# Field-Resolved Single-Cycle Deep-UV Pulses via Attosecond Solitons

**Amelie Marie Heinzerling**

SIGILL. UNIVERSITAT. LUDOVIC. MAXIM.

München 2024

# Field-Resolved Single-Cycle Deep-UV Pulses via Attosecond Solitons

**Amelie Marie Heinzerling**

Dissertation
an der Fakultät für Physik
der Ludwig–Maximilians–Universität
München

vorgelegt von
Amelie Marie Heinzerling, geb. Schulte
aus Leuven, Belgien

München, den 13.06.2024

Erstgutachter: Prof. Dr. Ferenc Krausz
Zweitgutachter: Prof. Dr. Peter Hommelhoff
Tag der mündlichen Prüfung: 01.08.2024

# Contents

# Zusammenfassung

Ultrakurze ultraviolette (UV) Laserpulse sind ein essentielles Werkzeug zur Untersuchung ultraschneller Elektronendynamiken in Festkörpern mit breiter Bandlücke [1,2], beispielsweise für optoelektronische Geräte, sowie in Molekülen [3,4]. Kürzlich hat das Konzept der Selbstkompression von Laserpulsen und der Erzeugung von tiefer UV-Strahlung (DUV) durch Emission von resonanten dispersiven Wellen (RDW) in Hohlkernfasern (HCF) großes Interesse geweckt, dieses als Quelle für ultrakurze, modulierbare DUV Pulse zu nutzen [5,6]. Um die durch diese Pulse induzierten ultraschnellen Licht-Materie-Wechselwirkungen vollständig zu verstehen, ist es wichtig, zeitaufgelöste Experimente mit vollständiger Feldauflösung durchzuführen. Attosekunden-Streaking und photoleitende Abtastung messen das elektrische Feld eines Laserpulses, einschließlich seiner Phaseneigenschaften [7–10]. Allerdings wurde das elektrische Feld eines ultrakurzen Pulses im DUV Wellenlängenbereich noch nie gemessen. Die vollständigen Informationen über das gesamte elektrische Feld eines solchen Pulses ermöglichen Untersuchungen der Phasen-Abhängigkeit, Attosekunden-Polarisations-Spektroskopie und elektronischen, molekularen Fingerabdrücken.

Im Rahmen dieser Doktorarbeit wurde die lineare photoleitende Abtastung (LPS) geprüft und mit Attosekunden-Streaking verglichen, jedoch erreichte der Aufbau für die Messung von UV-Strahlung seine Auflösungsgrenze. Daher wurde stattdessen die nichtlineare photoleitende Abtastung (NPS) weiter untersucht. Vor dieser Arbeit wurden Ergebnisse mit festen sowie gasförmigen Proben im Bereich zwischen 275 nm und 5300 nm veröffentlicht [10, 11]. In dieser Dissertation wurde nun die spektrale Bandbreite dieser NPS Messtechnik auf den kompletten DUV-Bereich erweitert, wobei Pulse mit Wellenlängen von bis zu 150 nm ($\sim$2 PHz / $\sim$8 eV) im vakuum-UV-Bereich gemessen wurden.

Für diese Messungen wurde ein geeigneter Aufbau zur DUV-Erzeugung entwickelt. Die neuesten Fortschritte im Themengebiet der Soliton-Dynamiken wurden angewandt und weiterentwickelt, um die Soliton-Selbstkompression sowie die DUV-RDW-Emission in einer kompakten HCF mit der vorhandenen Laserquelle zu induzieren. Zum ersten Mal wurde das elektrische Feld (inkl. der Phaseneigenschaften) eines selbstkomprimierten Solitons mit RDW im NIR-DUV-Bereich zeitaufgelöst abgetastet. Durch die Optimierung der Dispersion und der Phase konnte das Soliton inklusive der RDW zu einem Sub-Zyklus-Lichttransienten synthetisiert werden, welcher eine $E^2(t)$-Pulslänge von unvergleichbaren 323 as erreicht.

Außerdem wurde in dieser Doktorarbeit die RDW von den längeren Wellenlängen isoliert, was nahezu unabhängige Studien des Einzelzyklus-DUV-Pulses mit einer Intensitäts-Einhüllenden von 1.2 fs ermöglicht. Darüber hinaus wurde die Entstehung und das Verhaltens der Soliton-Dynamiken entlang der Faser und in Abhängigkeit vom Eingangsdruck untersucht, insbesondere durch Vergleiche mit Simulationen. Der Nachweis der Anwendbarkeit dieser intensiven Attosekundenpulse erfolgte durch nichtlineare Ionisationsmessungen. Zusammenfassend lässt sich sagen, dass der komplette Aufbau eine Schlüsseltechnologie zur Untersuchung von Licht-Materie-Wechselwirkungen auf der natürlichen Zeitskala des Elektrons in einem bisher unzugänglichen Spektralbereich (4 eV - 8 eV) darstellt.

# Abstract

Ultrashort ultraviolet (UV) laser pulses are an important tool for studying electron dynamics in wide-bandgap solids [1, 2], e.g. for optoelectronic devices, as well as in molecules [3, 4]. Recently, the concept of pulse self-compression and deep-ultraviolet (DUV) generation via resonant dispersive wave (RDW) emission in hollow-core fibers has attracted great interest to be used as a source of ultrashort and tunable deep-ultraviolet pulses [5, 6]. To fully understand the ultrafast light-matter interactions induced by these pulses, it is crucial to perform time-dependent experiments with full electric field resolution. Attosecond streaking and (non-) linear photoconductive sampling measure the electric field of a (typically infrared) laser pulse, including its carrier-envelope offset phase (CEP) [7–10]. However, the electric field of an ultrashort deep-ultraviolet pulse has never been measured, until now. Having the full-field information of such a pulse enables studies of the dependence on CEP, attosecond polarization spectroscopy as well as electronic fingerprinting of molecules.

In the framework of this PhD, linear photoconductive sampling (LPS) has been studied and benchmarked with attosecond streaking, but to measure ultraviolet radiation it was found to be limited in resolution. Therefore, nonlinear photoconductive sampling (NPS) has been further investigated. Before this work, results with solid or gas samples have been published between 275 nm and 5300 nm [10, 11]. Here, the spectral bandwidth of this metrology technique has been extended across the DUV region, measuring down to the vacuum-UV region around 150 nm ($\sim$2 PHz / $\sim$8 eV).

Therefore, a suitable DUV generation setup has been developed. The recent advancements in soliton dynamics have been applied and further developed in order to induce soliton self-compression and DUV RDW emission in a compact HCF with the existing laser source. For the first time, the electric field of a self-compressed soliton with a RDW in the NIR-DUV region has been sampled in a time-resolved manner, even delivering the field's phase information. By optimizing the dispersion and the CEP, the soliton and the RDW could be synthesized to a sub-cycle light transient reaching a full width at half maximum (FWHM) $E^2(t)$ pulse length as short as 323 as.

Moreover, in this PhD work, the RDW has been isolated from the longer wavelengths, enabling nearly independent studies of the single-cycle DUV pulse, with a FWHM intensity envelope around 1.2 fs. In addition, the evolution of soliton dynamics along the fiber and their pressure dependence has been investigated, particularly via comparisons with simulations. The applicability of these intense, attosecond pulses have been proven via nonlinear injection measurements. The complete setup provides a key technology apparatus for the investigation of light-matter interactions on the electron's natural timescale in a previously inaccessible spectral range, between 4 eV and 8 eV.

# List of Abbreviations

| | |
|---|---|
| Al | aluminum |
| Ar | argon |
| AOM | acousto-optic modulator |
| AOPDF | acousto-optic programmable dispersive filter |
| ATI | above-threshold ionization |
| BBO | beta-barium borate, $\beta$-$BaB_2O_4$ |
| BPF | bandpass filter |
| CCD | charge-coupled device |
| CEP | carrier-envelope-offset phase |
| CPA | chirped pulse amplification |
| CM | chirped mirror |
| CW | continuous wave |
| DFG | difference-frequency generation |
| DUV | deep-ultraviolet |
| FFT | fast Fourier transform |
| FROG | frequency-resolved optical gating |
| FS | fused silica |
| FWHM | full width at half maximum |
| GDD | group-delay dispersion |
| GVD | group-velocity dispersion |
| HCF | hollow-core fiber |
| He | helium |
| HH | high harmonic |
| HHG | high harmonic generation |
| IR | infrared |
| LPS | linear photoconductive sampling |
| $MgF_2$ | magnesium-fluoride |
| MIR | mid-infrared |

| | |
|---|---|
| MPI | multi-photon ionization |
| NLSE | nonlinear Schrödinger equation |
| NIR | near-infrared |
| NPS | nonlinear photoconductive sampling |
| PPLN | periodically polled lithium niobate |
| RDW | resonant dispersive wave |
| SFA | strong-field approximation |
| SFG | sum-frequency generation |
| SHG | second-harmonic generation |
| Si | silicon |
| $SiO_2$ | silicon dioxide |
| SPM | self-phase modulation |
| STD | standard deviation |
| TBP | time-bandwidth product |
| TDSE | time-dependent Schrödinger equation |
| THG | third harmonic generation |
| TIA | transimpedance amplifier |
| Ti:Sa | titanium doped sapphire, $Ti^{3+}:Al_2O_3$ |
| TOF | time-of-flight |
| UV | ultraviolet |
| VIS | visible |
| VUV | vacuum-ultraviolet |
| XUV | extreme ultraviolet |
| ZDW | zero-dispersion wavelength |

## Unit Prefixes

| | |
|---|---|
| P = peta | $10^{15}$ |
| T = tera | $10^{12}$ |
| G = giga | $10^{9}$ |
| M = mega | $10^{6}$ |
| k = kilo | $10^{3}$ |
| | $10^{0}$ |
| m = milli | $10^{-3}$ |
| $\mu$ = micro | $10^{-6}$ |
| n = nano | $10^{-9}$ |
| p = pico | $10^{-12}$ |
| f = femto | $10^{-15}$ |
| a = atto | $10^{-18}$ |

# List of Figures

# Chapter 1

# Introduction

The attosecond timescale is incredibly short, covering only a billionth of a billionth of a second, such that it is impossible for electronic devices to resolve signals this fast. Hence, the realm of attosecond physics might seem highly specialized and impractical, seemingly relevant only to a select group of researchers. However, its impact extends far beyond physics, as attoseconds are the natural timescale of electrons, the fundamental components of all matter. In attosecond physics, researchers seek for optical solutions, using the finely-controlled properties of light to resolve these ultrafast dynamics.

High harmonic generation (HHG), a technique to generate ultrashort light pulses with high photon energies, was experimentally developed and theoretically predicted to be in the attosecond timescale in the end of the 20th century [12–15]. In 2001, a train of attosecond pulses from HHG was measured experimentally in a time-resolved manner for the first time [16]. Shortly after, the first successful operation of a measurement setup was announced, functioning like an ultrafast camera [17–20] and capturing snapshots of isolated attosecond pulses [8,21]. These milestones paved the way for the examination of electron dynamics through light-matter interactions in various fields, from fundamental physics, to chemistry, engineering and medicine.

In the last two decades, ultrashort high harmonic pulses and the measurement techniques have become indispensable tools for probing electron dynamics not only within atoms [22,23] and solids [24–29], but also within complex molecular structures [30, 31], unlocking new frontiers in science and technology. With these attosecond pulses and the ability to detect them, analyzing the information they carry about interactions with a medium gave rise to new research fields such as attochemistry [32–34] and lightwave electronics [35–37].

Laboratories equipped with the required infrastructure, known as attosecond beamlines, typically generate high harmonic pulses in the extreme ultraviolet (XUV) spectral region. These wavelengths are even shorter than ultraviolet (UV) light emitted by the sun (UV-A, -B, & -C) and are undetectable by the human eye, appearing invisible to us. As much as the XUV region is required to investigate highly energetic dynamics, e.g. of core electrons [23, 38], it cannot be used for studies of dynamics appearing at smaller energies, e.g. of valence electrons making transitions to bound states. As a consequence, the generation of light transients at longer wavelengths was developed. With different techniques, such as field synthesis, ultrashort pulses in the visible (VIS) and near-infrared (NIR) range could be created [39–41]. Optimally, the complete spectral region should be available in order to study all kinds of ultrafast dynamics. However, efficiently generating pulses within the range between visible and XUV radiation (the UV) on the attosecond timescale remained a challenge for a long time.

Moreover, not only the generation of ultrashort UV pulses is challenging, also extending the bandwidth of the measurement techniques, so-called attosecond metrology, has been difficult. Nevertheless, vigorous efforts have been made to further develop attosecond metrology, capturing the complete information of ultrafast laser pulses and evolving into a new direction over time. In recent years, the electric field of light has been measured via photo-induced currents, providing detailed insights into light-matter interactions [2]. This current sampling technique, referred to as photoconductive sampling, uses ultrashort laser fields to induce charges extremely rapidly, effectively acting as an attosecond gate. On the basis of the Auston switch [42], and further advancements in order to operate with different mechanisms [9, 43–45] as well as in various materials, such as solids [10, 44, 46], nanostructures [47–49] and gases [11, 50], this method enables sampling of fields with petahertz (PHz) bandwidth. However, along with the traditional 'streak camera', only laser fields in the visible / near-UV up to the IR could be resolved. The shortest measurements of the field's oscillations and phase cover wavelengths down to 275 nm [10] (~1.1 PHz) performed via nonlinear photoconductive sampling in a solid. To the best of our knowledge, field sampling of deep-ultraviolet (DUV) or vacuum-ultraviolet (VUV) radiation (see spectral overview in appendix A.1), popularly known as UV-C radiation, has never been reported.

The goal of this work is to extend the spectral regime of ultrashort field sampling and generate few- to single-cycle pulses in the deep-ultraviolet regime while extending current metrology techniques to cover not only the near-UV to NIR regime, but also the deep-UV, down to the vacuum-UV. The energy range between ~ 4 and 8 eV has so far remained inaccessible for field-resolved experiments. The first challenge is to generate ultraviolet radiation and delivering it as ultrashort pulses. The compression of ultraviolet pulses is complicated as this radiation is absorbed in most materials such that the current dispersive mirror technology cannot counteract any pulse lengthening in this spectral regime. Therefore, a generation technique is needed that directly provides compressed pulses. The second challenge is pushing the bandwidth of attosecond metrology, as DUV pulses have never been measured in a field-resolved manner. On these short timescales, the oscillatory behaviour becomes extremely relevant. The details of the electric field, i.e. the carrier wave and its phase carry the information about light-matter interactions and moreover, can be tuned to optimize their influence. So far, only the complex envelope of the fields could be accessed in the DUV [51–53], as well as in the XUV (e.g. through reconstruction via attosecond streaking [7, 21]). The field sampling techniques were not investigated in this regime yet and remained an open question, until it was studied in this work.

To approach the first challenge, novel research is reviewed. Recently, the generation of ultrashort pulses has been pushed to deliver durations as short as 1.9 fs at around 260 nm and with hundreds of nJ energy generated via frequency upconversion (harmonics) [51, 52]. However, this technique suffers from poor tunability and limited spectral properties. Fortunately, recent advances in nonlinear fiber optics offer a unique way of realizing sources generating ultrashort UV pulses with unprecedented peak and average power [5, 6, 54]. The exceptional dynamics of optical solitons, optical fields which maintain their shape upon propagation, have been found to be generable in simple gas-filled hollow-core fibers (HCFs) [55]. Controlled dynamics allow for self-compression of such solitons, leading to ultrashort pulses and emission of so-called resonant dispersive waves in compact fiber systems [55, 56]. As specific dispersion requirements need to be fulfilled that do not naturally occur in HCFs, this regime was only exploited in the last decade, allowing the generation of intense, tunable ultraviolet pulses, with few-femtosecond durations [53, 57].

The major findings of this work are the measurements of electric fields containing deep-ultraviolet (DUV) radiation and attosecond pulses, which are shorter than any previously reported in this spectral region. The results were made possible by extending the photoconductive sampling technique across the DUV to the VUV, tackling the second challenge. In order to generate these exceptional pulses, the recent advances in soliton dynamics were adapted and applied to an existing few-femtosecond VIS-NIR laser system. The developed setup enabled producing attosecond solitons and DUV resonant dispersive waves (RDWs) with extraordinarily short pulse durations. The route towards these results and the related findings are presented in this thesis as follows.

Chapter 2 provides the theoretical framework for understanding the utilized physical phenomena and corresponding experimental results. First, ultrashort laser pulses are introduced, and the importance of their phase is explained. The behaviour during propagation and interaction with matter is fundamental for this work and is thus presented in detail. The linear and nonlinear regimes are explained separately, resulting in different optical effects. Next, the combination of both is discussed, as certain configurations can lead to completely new phenomena: optical solitons and RDWs. Finally, the basics of strong-field phenomena are explained, covering the most common generation technique of attosecond pulses, the high harmonic generation.

In Chapter 3, the experimental setup and methods used are presented. A detailed description of the laser source is followed by the presentation of the relevant metrology techniques. The principle of attosecond streaking, the 'ultrafast camera', is explained, as well as the experimental setup (beamline AS2) used to perform streaking measurements. Subsequently, the concepts of photoconductive sampling and the distinction between linear (LPS) and nonlinear photoconductive sampling (NPS) are presented. For LPS, the same existing attosecond beamline AS2 is used to perform experiments, while a suitable NPS setup did not exist yet.

The following chapters cover the experimental results. Chapter 4 discusses the comparison of LPS with attosecond streaking, measured simultaneously for the first time ever. The measurement of the delay-dependent signal at different photon energies via attosecond streaking sheds light on the occurrence of the LPS signal. The temporal distribution of the different frequencies in the XUV pulse is visible in the streaking spectrogram, allowing to match the LPS trace with certain energies. Further, the spectral bandwidth of the measured field was extended via self-phase modulation (SPM) in a HCF in order to push LPS towards ultraviolet wavelengths. However, the LPS setup was found to be limited in bandwidth.

Chapter 5 lays the foundation for the generation and characterization of ultrashort ultraviolet pulses. As the previous techniques are not applicable to resolve DUV radiation, an NPS setup is developed to achieve this goal. The extended spectrum is further optimized and measured in a field-resolved manner, proving the NPS detection capability of UV radiation with a gas sample. Since the pulse length was measured to be greater than 7 fs, and pulse compression could not be developed for the DUV region, generation via SPM is not expedient. Instead, the advances in soliton dynamics provide a promising route. The experimental requirements and the corresponding development of a setup are presented. The detection of DUV radiation is performed with a spectrometer, raising hope for short pulse durations.

Chapter 6 combines the generation of DUV radiation via RDW emission with the advanced NPS setup, pushing the bandwidth of this field sampling technique further into the DUV. The detection of wavelengths as short as 150 nm (8 eV) via field sampling is presented, setting a new record. With pulse durations in this regime of only 1.2 fs, they are the shortest ever reported in the UV range. Moreover, not only is the RDW measured, but also the self-compressed soliton in the VIS-NIR. By tuning the phase of the input pulse, sub-cycle attosecond light transients with unrivaled durations of $\sim$320 as can be generated. The results are compared with simulations of soliton dynamics, explaining the generation mechanism. Finally, the attosecond pulses are used as a gate to measure VIS-NIR pulses, demonstrating the applicability to trigger ultrafast nonlinear processes in a previously inaccessible spectral range.

Chapter 7 provides a summary and evaluation of the presented results. The motivation and challenges are reviewed, followed by a discussion of the new findings and possible further advancements of the setup. Subsequently, in Chapter 8, conclusions are drawn on the impact of this PhD work through its possible applications. An outlook is given, providing a wide range of new research opportunities enabled by the results presented in this dissertation.

# Chapter 2

# Theoretical Background

This chapter provides the theoretical foundations to understand the physical principles covered in this PhD work, which is based on light-matter-interaction on the attosecond and femtosecond timescale. Generally, ultrashort laser pulses are fundamental to attosecond physics. Characterized by their electric field, these pulses interact with a medium to drive various optical processes. Depending on the laser intensity, different phenomena can be initiated and influenced, including nonlinear optical effects. Additionally, strong-field dynamics, such as multi-photon and tunnel ionization, play a crucial role in attosecond physics, as high laser intensities enable electron emission and manipulation on their natural timescale, the attosecond timescale.

First, in section 2.1 an overview about ultrashort laser pulses is given, including the mathematical description of their generation and propagation. Secondly, the description of nonlinear optical phenomena and light-matter interaction is presented in section 2.2. This topic includes the interactions of the laser fields with gas in a hollow-core fiber and the basics of soliton and resonant dispersive wave emission. Thirdly, different strong-field phenomena are covered in section 2.3, including the generation of attosecond pulses via high harmonic generation (HHG).

## 2.1 Ultrashort Pulses

Ultrashort laser pulses are electromagnetic wave packets that can be fully described by the Maxwell's equations [58]:

$$\begin{aligned}\nabla \cdot \vec{D} &= \rho \\ \nabla \cdot \vec{B} &= 0 \\ \nabla \times \vec{E} &= -\frac{\partial \vec{B}}{\partial t} \\ \nabla \times \vec{H} &= \frac{\partial \vec{D}}{\partial t} + \vec{J}\end{aligned} \tag{2.1}$$

where $\vec{D}$ is the electric displacement field, $\rho$ is the electric charge density, $\vec{B}$ is the magnetic field, $\vec{H}$ is the magnetic field strength and $\vec{J}$ is the current density. Assuming non-magnetic materials, these variables are correlated via the following relationships:

$$\vec{D} = \epsilon_0 \vec{E} + \vec{P}, \qquad \vec{B} = \mu_0 \vec{H}. \tag{2.2}$$

where $\epsilon_0$ is the permittivity and $\mu_0$ the permeability of free space, related via the speed of light $c$ as $\epsilon_0 \mu_0 = 1/c^2$.

In this thesis, the laser pulses are described exclusively by their electric field. The magnetic field description is equivalent and can be derived from Faraday's law (Maxwell's Eq. 2.1 no. 3), if needed. In addition, we assume that the electric field has no spatial or polarization dependence for now, such that it can be completely described in time as $\vec{E}(x, y, z, t) = E(t)$, which is equivalent to a complete description in the frequency domain, as explained in the following [59].

To convert the temporal description of the electric field to the frequency domain a complex Fourier transformation has to be conducted as follows:

$$\tilde{E}(\omega) = \mathcal{F}(E(t)) = \int_{-\infty}^{+\infty} E(t) e^{-i\omega t} dt, \tag{2.3}$$

Note that a measured electric field only contains the real part $E(t)$. When performing a complex Fourier transformation, we derive the corresponding complex spectrum $\tilde{E}(\omega)$, emphasized with a tilde, containing the frequencies $\omega$. Performing the inverse Fourier transform not for the whole frequency set, but only the positive frequencies (from zero to infinity), results in the physical solution of the complex electric field:

$$\tilde{E}^{+}(t) = \frac{1}{2\pi} \int_{0}^{+\infty} \tilde{E}(\omega) e^{i\omega t} d\omega = \frac{1}{2\pi} \int_{-\infty}^{+\infty} \tilde{E}^{+}(\omega) e^{i\omega t} d\omega. \tag{2.4}$$

This complex electric field $\tilde{E}^{+}(t)$, containing only positive frequencies, is known as analytic signal and can be rewritten into the product of two terms: an amplitude term and a phase term:

$$\tilde{E}^{+}(t) = A(t)e^{i(\phi(t)+\omega_0 t)}, \tag{2.5}$$

where $A(t)$ is the pulse envelope, while $e^{i\omega t+i\phi}$ describes the carrier wave. $\omega_0$ is the carrier frequency of the laser, determining the field oscillations. The phase $\phi$ can be Taylor expanded into a time-independent term $\varphi_0$, a linearly time-dependent term $\varphi^{(1)}(t)$ and higher-order terms:

$$\begin{aligned}\phi(t) &= \sum_{n=0}^{\infty} \frac{\phi^{(n)}(t-t_0)^n}{n!}. \\ &= \varphi_0 + \varphi^{(1)}(t-t_0) + \frac{1}{2}\varphi^{(2)}(t-t_0)^2 + .., \\ &= \varphi(t_0) + \left.\frac{d\varphi}{dt}\right|_{t_0}(t-t_0) + \frac{1}{2}\left.\frac{d^2\varphi}{dt^2}\right|_{t_0}(t-t_0)^2 + ..\end{aligned} \tag{2.6}$$

The first term $\varphi_0$ describes the phase between the carrier wave and the peak of the envelope and is thus called carrier-envelope offset phase (CEP). Hence, varying the CEP only changes the distribution of the carrier in the envelope, but has no influence on the envelope itself. For longer pulses the CEP can often be neglected and a slowly varying envelope approximation (SVEA) can be applied. Since the term 'ultrashort pulses' can cover attoseconds to picoseconds, which is a very broad range, it has to be noted that within this range there is a point where the CEP cannot be neglected anymore. With pulses that have three-cycles or less, SVEA is not valid. For few-femtosecond and attosecond pulses in the UV-NIR region, the CEP has a tremendous influence. An example for the importance is shown in Fig. 2.1. In a) a few-cycle pulse is presented with a pulse duration of 3 fs. Two different CEPs, 0 and $\pi/2$, are shown in blue and green dash-dotted, respectively. In addition, in b), a 30 fs long pulse is presented for both phases, depicting that the CEP becomes less important for pulses with more optical cycles.

Here (in Fig. 2.1), a typical Gaussian pulse envelope $A(t)$ is used, described by [60]:

$$A(t) = E_0 \cdot \exp\left(-2\ln 2\frac{t^2}{\tau_{fwhm}^2}\right), \tag{2.7}$$

where $E_0$ is the amplitude and $\tau_{fwhm}$ describes the pulse duration as the full-width at half maximum (FWHM) of the intensity $I \propto |E(t)|^2$. Moreover, the pulses are shown in the optimal case with the minimal possible pulse duration, i.e. without any phase terms that would lead to pulse lengthening.

However, in reality the time-dependent phase is not zero and leads to longer pulse durations. The linear phase $\varphi^{(1)}(t-t_0)$ combined with the carrier frequency

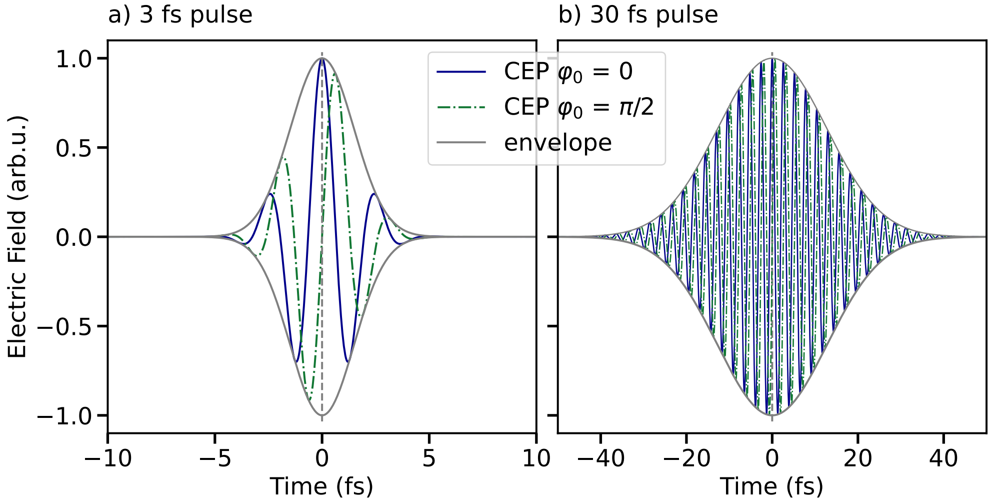

Figure 2.1: CEP influence on electric fields with durations of 3 fs (a) vs. 30 fs (b). The pulse with CEP $= 0$ is shown in blue, while the pulse with a shifted carrier by $\pi/2$ is shown in green dash-dotted.

leads to a time-dependent carrier frequency: the instantaneous frequency:

$$\omega_{inst} = \omega_0 + \varphi^{(1)}(t) = \omega_0 + \frac{d\varphi(t)}{dt}. \tag{2.8}$$

For ultrashort pulses, the frequency bandwidth of an electric field is wide and the instantaneous frequency describes which frequencies occur at a certain time. The second order temporal phase $\frac{d2\varphi}{dt^2}$ describes the chirp of the pulse, meaning that the instantaneous frequency is increasing or decreasing over time. Therefore, it is often described in the frequency domain as higher orders of the spectral phase, which can be defined, similar to the temporal phase, as a Taylor expansion around the carrier frequency $\omega_0$ as:

$$\begin{aligned}\Phi(\omega) &= \sum_{n=0}^{\infty} \frac{\Phi^{(n)}(\omega-\omega_0)^n}{n!}. \\ &= \Phi(\omega_0) + \left.\frac{d\Phi}{d\omega}\right|_{\omega_0}(\omega-\omega_0) + \frac{1}{2}\left.\frac{d^2\Phi}{d\omega^2}\right|_{\omega_0}(\omega-\omega_0)^2 + ..\end{aligned} \tag{2.9}$$

The zeroth order term corresponds again to the CEP, while the first order term is called group delay, describing a temporal shift of the pulse envelope. The second order term refers to the group delay dispersion (GDD). Generally, when a pulse propagates through a dispersive medium (such as glass or air) it acquires a frequency-dependent spectral phase due to the frequency-dependent refractive index of the medium $n(\omega)$. This can also include higher order terms, introducing nonlinear chirp.

The complex spectrum containing positive frequencies can be described using the spectral phase $\Phi$ and the spectral intensity $S(\omega)$:

$$\tilde{E}^{+}(\omega) = \sqrt{S(\omega)}e^{i\Phi(\omega)}. \tag{2.10}$$

In reality, spectrometers often acquire the intensity vs. wavelength $S(\lambda)$. Frequency and wavelength are related via $\omega = 2\pi c/\lambda$ and to transform from one to the other, we have to consider energy conversation as:

$$\int_{-\infty}^{+\infty} S_{\lambda}(\lambda) d\lambda = \int_{-\infty}^{+\infty} S_{\omega}(\omega) d\omega. \tag{2.11}$$

Therefore, to transform a frequency-dependent spectrum to be wavelength-dependent for comparison with a spectrum measured with a typical spectrometer, the spectrum has to be corrected by a factor $\propto \lambda^{-2}$ as:

$$S_{\lambda}(\lambda) = S_{\omega}(\omega)\frac{d\omega}{d\lambda} = S_{\omega}(2\pi c/\lambda)\frac{2\pi c}{\lambda^2}. \tag{2.12}$$

The spectral phase is easily transformed from frequency to wavelength via $\Phi_{\lambda}(\lambda) = \Phi_{\omega}(2\pi c/\lambda)$ [61].

The shortest possible pulse duration can only occur if all frequency components are in phase, meaning that the phase derivatives are zero. Consequently, in attosecond experiments, managing the dispersion in order to minimize the pulse duration is one of the main tasks. The phase accumulation in air due to its dispersion is one of the major reasons why experiments with few-femtosecond or attosecond pulses are performed in vacuum. Another major reason is the high absorption of low wavelengths in atoms, and smaller aspects such as air circulations and corresponding fluctuations and dust.

Moreover, resulting from the Fourier transformation, the pulse duration is inversely related with the spectral bandwidth. Hence, the wider the range of frequencies a laser field contains, the shorter it can be in time. The required spectral bandwidth $\Delta\omega$ to reach a certain pulse length $\tau_{fwhm}$ can be calculated via the time-bandwidth product (TBP)

$$\tau_{fwhm} \cdot \Delta\omega \geq 2\pi \cdot a, \tag{2.13}$$

reaching equality for the minimal pulse duration, the theoretical case of a flat spectral phase. Depending on the pulse shape, the quantity $a$ has to be chosen accordingly. For a Gaussian pulse the TBP is defined with $a = 0.441$ [59].

## 2.2 Nonlinear Optics

Nonlinear optical phenomena of laser pulses in a medium without free charges ($\rho = 0$) and without free currents ($\vec{J} = 0$) are described by the nonlinear wave equation, derived from Maxwell's equations (Eq. 2.1) using Cartesian coordinates to [59]:

$$\left(\nabla^2 - \frac{1}{c^2}\frac{\partial^2}{\partial t^2}\right)\vec{E}(x,y,z,t) = \frac{1}{\epsilon_0 c^2}\frac{\partial^2}{\partial t^2}\vec{P}(x,y,z,t), \tag{2.14}$$

with $\nabla^2 = \frac{\partial^2}{\partial x^2} + \frac{\partial^2}{\partial y^2} + \frac{\partial^2}{\partial z^2}$. The polarisation $\vec{P}$ describes the response of the medium due to the interaction with the laser field. It can be expressed as a power series of the electric field strength $E(t)$ assuming an instantaneous response [62]:

$$\begin{aligned} \vec{P} &= \underbrace{\epsilon_0\chi^{(1)}\vec{E}(t)}_{\vec{P}_L} + \underbrace{\epsilon_0\chi^{(2)}\vec{E}^2(t) + \epsilon_0\chi^{(3)}\vec{E}^3(t) + \dots + \epsilon_0\chi^{(n)}\vec{E}^n(t) + \dots}_{\vec{P}_{NL},}, \end{aligned} \tag{2.15}$$

enabling the differentiation into a linear polarisation $\vec{P}_L$ and nonlinear polarisation $\vec{P}_{NL}$, depending on the electric field strength. The parameter $\chi^{(1)}$ is known as the linear optical susceptibility, while the higher orders, $\chi^{(n)}$ with $n > 1$ describe the nth-order nonlinear optical susceptibility as a nth-rank tensor. Separating the polarisation into $\vec{P}_L = \epsilon_0\chi^{(1)}\vec{E}$ and $\vec{P}_{NL}$ and applying the relation $n_0^2(\omega) = 1+\chi^{(1)}(\omega)$ assuming an isotropic medium with a frequency-dependent refractive index $n(\omega)$, leads to the following form of the wave equation:

$$\nabla^2\vec{E} - \frac{n(\omega)^2}{c^2}\frac{\partial^2\vec{E}}{\partial t^2} = \frac{1}{\epsilon_0 c^2}\frac{\partial^2\vec{P}_{NL}}{\partial t^2}. \tag{2.16}$$

This representation highlights that the nonlinear response of the medium, the time-varying nonlinear polarization, drives the electric field. Hence, the right-hand side of the equation acts as a source term, accelerating the charges in the medium. Assuming a linearly polarized field propagating along the $z$-direction in a medium with a frequency-dependent refractive index $n(\omega)$, the wave equation can be Fourier transformed to:

$$\left(\frac{\partial^2}{\partial z^2} + \underbrace{\frac{n^2(\omega)}{c^2}\omega^2}_{k^2}\right)\tilde{E}(z,\omega) = -\frac{\omega^2}{\epsilon_0 c^2}\tilde{P}_{NL}(z,\omega). \tag{2.17}$$

The labelled prefactor is known as the frequency-dependent wave vector $k(\omega)$.

In the linear case, i.e. without a nonlinear source term ($P_{NL} = 0$), a plane wave has the following solution for the wave equation in the time domain (Eq. 2.16):

$$E(z,t) = E_0(z,t)e^{i(\omega_0 t - k_0 z)}, \tag{2.18}$$

for a laser field with central frequency $\omega_0$ and corresponding wave vector $k_0 = \omega_0 n(\omega_0)/c$. This field can evolve during propagation through a material, effected by the induced polarization $\vec{P}_L$. The relevant effects are described in the following section 2.2.1. Afterwards, in 2.2.2, the 3rd-order nonlinear polarization $\vec{P}_{NL}$ is discussed. The importance of the balance of these two effects is covered in 2.2.3. Even orders and higher odd orders are not discussed, as they are not relevant for this work.

### 2.2.1 Linear Polarization

Keeping the assumption that the nonlinear polarization is negligible, we can study the influence of the linear polarization on the pulse. The spectral phase can change with frequency in different ways (Eq. 2.9). When a laser pulse propagates through a dispersive medium with refractive index $n_0(\omega) = n(\omega)$ of length $L$, it accumulates the spectral phase:

$$\Phi(\omega, L) = k(\omega)L = \frac{\omega}{c} n(\omega)L. \tag{2.19}$$

Frequency-related phase effects are often described through the change of the wave vector via the beta coefficients:

$$\beta_j = \left. \frac{d^j k(\omega)}{d\omega^j} \right|_{\omega_0}, \tag{2.20}$$

which corresponds to the phase for each order (Eq. 2.9) per unit length. The second order derivative of the phase is the group delay dispersion (GDD), and the GDD per unit length is called group velocity dispersion (GVD or $\beta_2$). The group velocity $v_g$, described via $1/v_g = dk/d\omega = \beta_1$, represents the velocity of the pulse envelope. When the group velocity is dispersed, it changes with frequency as:

$$\beta_2 = \left. \frac{d^2 k(\omega)}{d\omega^2} \right|_{\omega_0} = \left. \frac{d}{d\omega} \frac{1}{v_g} \right|_{\omega_0}. \tag{2.21}$$

When a pulse shows a linear change of the instantaneous frequency over time, we refer to a linearly chirped pulse. A pulse can become chirped by propagation through a material with $\beta \neq 0$, meaning the frequencies propagate with different group velocities, and hence, leading to a stretched pulse. A pulse whose frequencies increase with time is called positively chirped. This case corresponds to positive values for $\beta_2$, meaning that a pulse experiences so-called normal dispersion in the material during propagation, leading to a positive chirp. In contrast, a decrease of frequencies over time is referred to a negatively chirped pulse, which can be acquired by propagation through a material with anomalous dispersion, as $\beta_2 < 0$. For a broad spectrum, it can happen that one part experiences normal dispersion, while another part experiences anomalous dispersion. The value at which $\beta_2$ changes its sign, i.e. exactly at $\beta_2 = 0$, is called zero-dispersion wavelength (ZDW).

### 2.2.2 3rd-order Nonlinear Polarization

Nonlinear polarisation terms cannot be neglected when using high laser intensities. Depending on the field strength, different orders of the polarisation in Eq. 2.15 become relevant. Moreover, in order to give a description of the encountered nonlinear effects, we have to distinguish between different media and their properties, in particular their inversion symmetry. Second-order effects such as second harmonic generation (SHG) and sum- and difference-frequency generation (SFG and DFG, respectively) can only occur in a medium without inversion symmetry, i.e. non-centrosymmetric crystals, exhibiting $\chi^{(2)}$.

In general, all even orders of the nonlinear susceptibility, and thus all even order terms of the nonlinear polarization, are zero for materials with inversion symmetry. As gases do possess inversion symmetry, the strongest and first nonlinear effect in gases is contributed by the third order $P^{(3)}$. Since the gas medium is exclusively used in this PhD work, the most important related effects are covered below.

As the even order nonlinear susceptibility vanishes in gases, the third order $\chi^{(3)}E^3$ shows the highest contribution to the nonlinear polarization. Therefore, we neglect higher orders in the following and consider the third order as the exclusive contribution to the nonlinear polarization as:

$$P_{NL}(t) = \epsilon_0 \chi^{(3)} E^3(t). \tag{2.22}$$

Assuming an electric field described by $E = E_0(t) \cdot (e^{i\omega t} + e^{-i\omega t})$ and an instantaneous response, the nonlinear polarization becomes:

$$P_{NL} = \epsilon_0 \chi^{(3)} \left( \frac{1}{8} E^3 e^{i3\omega t} + \frac{3}{8} |E|^2 E e^{i\omega t} \right) + c.c., \tag{2.23}$$

including two major terms that describe two different effects. The oscillation at $3\omega$ in the first term occurs due to third harmonic generation. For efficient frequency conversion, phase matching (momentum conversation) is required. The second term oscillates at the fundamental frequency and is proportional to the pulse intensity $I(t) = \frac{1}{2}\epsilon_0 n c |E(t)|^2$, causing the so-called Kerr effect, which is described as an intensity-dependent refractive index:

$$n = n_0 + n_2 I, \tag{2.24}$$

introducing the nonlinear refractive index $n_2 = 3\chi^{(3)}/2n_0^2\epsilon_0 c$. Assuming an intense plane wave $E(z,t)$ travelling through a medium with Kerr refractive index (2.24), the wave vector in Eq. 2.18 has to be altered to $k = \omega(n_0 + n_2 I)/c = k_0 + k_{NL}$. Hence, due to $k_{NL} \propto n_2$, the pulse does not only accumulate the phase $\Phi = k_0 L$ during propagation, but also experiences a nonlinear phase shift as:

$$\Phi_{NL}(t) = -\frac{\omega}{c} n_2 I(t) L = -\frac{2\pi}{\lambda} n_2 I(t), \tag{2.25}$$

leading to a change in instantaneous frequency (chirp) to:

$$\Delta\omega_{inst} = \frac{d}{dt}\Phi_{NL}(t) = -\frac{\omega}{c}n_2\frac{dI(t)}{dt}L. \tag{2.26}$$

As a consequence, the frequencies in the leading part of an initially unchirped Gaussian pulse, having increasing intensity ($dI/dt > 0$), are shifting to smaller values (red-shift), while the the trailing edge is blue-shifted due to the decreasing intensity $dI/dt < 0$ (assuming $n_2 > 0$). Hence, the pulse becomes positively chirped. If the shift $\Delta\omega_{inst}$ exceeds the bandwidth of the pulse, new frequency components are generated and thus, spectral broadening takes place. This effect is called self-phase modulation (SPM).

Moreover, the nonlinear refractive index $n_2$ influences the group velocity $v_g$. When the group-velocity becomes intensity-dependent, the pulse shape can be altered. In that case, the peak of the envelope becomes slower compared to the edges, which is referred to as self-steepening. As the propagation distance increases, the steepening of the trailing edge intensifies. If it reaches the point of becoming vertical, the pulse breaks up, a phenomenon known as optical shock.

### 2.2.3 Optical Solitons

The nonlinear Schrödinger equation (NLSE) can be written as follows [63]:

$$i\frac{dE}{dz} = \frac{\beta_2}{2}\frac{d^2E}{dt^2} - \gamma|E|^2E \tag{2.27}$$

to describe the propagation of an optical pulse $E(z,t)$ with slowly varying envelope (negligible $d^2E/dz^2$) through a dispersive, nonlinear optical medium with nonlinear coefficient $\gamma = 2n_0\epsilon_0 n_2\omega_0$. The first term on the right-hand side describes the change of the pulse through the influence of the group velocity **dispersion** $\beta_2$, while the second term resembles the self-phase modulation (due to **nonlinearity**). We have seen in the two previous sections that both effects can lead to a stretch of the pulse due to chirp. One solution to this NLSE is the case in which dispersion and nonlinearity are balanced, resulting in an invariant pulse shape during propagation. As explained in section 2.2.2, SPM leads to positive chirp. In order to compensate for this effect, the dispersion has to be anomalous, introducing negative chirp. When SPM and GVD are acting together and totally balance each other, while other effects are negligible, a so-called fundamental optical soliton occurs (Fig. 2.2).

A common platform to study soliton effects are hollow-core fibers (HCFs) filled with noble gases. They transmit a broad spectral range, which is crucial for ultrashort pulses, and the gases show high ionization energies, enabling higher pulse energies. Moreover, this setup can be tuned in fiber length, core diameter, gas

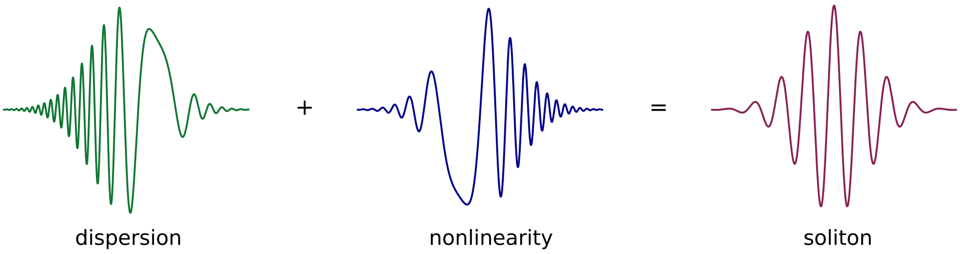

Figure 2.2: When dispersion and nonlinearity are balanced, a fundamental optical soliton can occur.

type and gas pressure, allowing the tuning of GVD and SPM to achieve the desired configuration. The GVD of HCFs is described by [5]:

$$\beta_2 \approx \frac{\lambda^3}{4\pi c^2}\left(\rho\frac{\partial^2\chi_e}{\partial\lambda^2} - \frac{u_{nm}^2}{2\pi^2 a^2}\right). \tag{2.28}$$

Here, $\rho$ represents the gas density relative to standard conditions, $\chi_e$ denotes the susceptibility of the filling gas species under those standard conditions, $u_{nm}$ describes the mode as the mth zero of the Bessel function $J_{n-1}$ and $a$ is the hollow core radius. The first term on the right-hand side of the equation arises from the material dispersion of the filling gas, while the second component accounts for the anomalous dispersion induced by confinement within the waveguide core. A notable characteristic of gas-filled hollow fibers is their inherent ability to modify the dispersion profile simply by adjusting the pressure and composition of the filling gas.

To define the conditions for soliton dynamics, it is useful to define the dispersion length in optical fibers as a distance, over which dispersive effects become important as [63]:

$$L_D = \frac{\tau_0^2}{|\beta_2|}, \tag{2.29}$$

depending on the pulse length $\tau_0$ and the GVD $\beta_2$ (described by Eq. 2.28). Similarly we can define the nonlinear length, the distance over which nonlinear effects (SPM) become important:

$$L_{NL} = \frac{1}{\gamma P_0}, \tag{2.30}$$

with the nonlinear coefficient $\gamma$ as defined above, determined by $n_2$ of the gas in the fiber, and the laser peak power $P_0$. Depending on the two effects, and their relative importance, we can differentiate four categories. Therefore, we define the soliton order $N$ as:

$$N = \sqrt{\frac{L_D}{L_{NL}}} = \sqrt{\frac{\tau_0^2\gamma P_0}{|\beta_2|}}. \tag{2.31}$$

In the first category, the fiber is so short that neither of the effects play a significant role ($L \ll L_{NL}$, $L \ll L_D$) and the definition of the soliton order is pointless. The other three cases are:

- $L \ll L_{NL}$, $L \sim L_D$, $N \gg 1$: dispersion (GVD) dominates,
- $L \sim L_{NL}$, $L \ll L_D$, $N \ll 1$: nonlinearity (SPM) dominates,
- $L \sim L_{NL}$, $L \sim L_D$, $N \sim 1$: SPM and GVD play an equally important role.

Since GVD and SPM were discussed before, here in this section, the fourth category where SPM and GVD are comparable is discussed. As mentioned above, when GVD and SPM perfectly balance each other, hence $N = 1$, a fundamental soliton exists. However, when the effects are comparable, but $N \neq 1$, higher-order solitons occur. They can change their temporal and spectral shape, but they return to their initial shape periodically every oscillation.

When the value of N surpasses 1.5, an optical pulse evolves into a second- or higher-order soliton. In either case, SPM dominates initially. Thus, when propagating through the fiber, the spectrum is extended and the pulse gets positively chirped. The increased bandwidth enhances the impact of anomalous dispersion, compensating the chirp again. This interplay results in a slight compression of the pulse and higher peak power. Theoretically, when the optimal configuration with maximum bandwidth and temporal compression is reached, the cycle continues until the initial settings are present again.

However, in reality, higher-order solitons can encounter perturbations induced by third- or higher-order dispersion (e.g. $\beta_3$). Then, such solitons undergo a so-called fission process, leading to further spectral broadening, and subsequent pulse compression, eventually resulting in a breakup of the higher-order solitons into multiple fundamental solitons of varying width. Due to perturbations and self-steepening, this iterative process of spectral broadening and pulse compression has the potential for significant self-compression, potentially reducing the pulse duration to less than one optical cycle at the pump wavelength, alongside extensive spectral broadening [55]. We refer to these pulses as self-compressed solitons.

The soliton fission length $L_{fiss}$ is defined as the length scale where soliton self-compression occurs as [5]:

$$L_{fiss} = \frac{L_D}{N} = \sqrt{L_D L_{NL}} \propto \frac{\tau a^2}{\lambda^3 \sqrt{I_0}}, \tag{2.32}$$

depending on the ratio of the wavelength cubed vs. the fiber core diameter $a$ squared, since $L_{NL}$ is proportional to $a^2/I_0$ in a single fiber mode. Tuning the fiber length to slightly larger $L > L_{fiss}$, results in the shortest pulse duration, highest peak power, and maximal spectral broadening.

In addition to the perturbation via higher-order dispersion, fibers have losses that are not negligible in reality. To account for them, the term $-\frac{i\alpha}{2}E$ can be added on the right hand side of the NLSE [63]. We can define the length after which the power is reduced by 1/e as

$$L_{loss} = \frac{4\pi^2 a^3}{3u_{nm}^2 \lambda^2} \propto \frac{a^3}{\lambda^2}, \tag{2.33}$$

depending on the wavelength, HCF core radius $a$ and mode of the beam, described by $u_{nm}$, the mth zero of the Bessel function $J_{n-1}$. To observe soliton dynamics, $L_{fiss}$ should be smaller than $L_{loss}$.

Moreover, this perturbation through the third- or higher-order dispersion, can lead to resonant dispersive wave (RDW) emission. This phenomenon describes radiation emitted by the perturbed soliton, meaning that it transfers energy to higher frequencies which propagate with the same phase velocity. For an efficient ('resonant') energy transfer, the phase of the soliton experiencing anomalous dispersion has to be matched with the phase of the RDW, propagating linearly in the normal dispersion regime. The phase matching condition can be written as [64]:

$$\beta_L(\omega) \overset{!}{=} \beta_s(\omega) \qquad \text{with:} \tag{2.34}$$

$$\begin{aligned} \beta_L(\omega) &= \beta_0 + \beta_1(\omega-\omega_0) + \frac{1}{2}\beta_2(\omega-\omega_0)^2 + \frac{1}{6}\beta_3(\omega-\omega_0)^2 + .. \\ \beta_s(\omega) &= \beta_0 + \beta_1(\omega-\omega_0) + \frac{\gamma P_0}{2} \end{aligned} \tag{2.35}$$

In reality, especially the linear phase of the RDW has to be matched with the nonlinear phase of the propagating soliton. When changing the gas pressure, mostly the third order dispersion $\beta_3$ experienced by the RDW is tuned, leading to an increase of $\beta_L$. When adjusting the power, it mostly contributes to a change in the nonlinear propagation constant $\gamma$ of the soliton. As a consequence, these two parameters, gas pressure and power, can be used to experimentally tune the RDW wavelength, such that phase matching is accomplished. The value of the zero-dispersion wavelength is a good indicator if and at which wavelength the RDW emission can occur.

In hollow-core fibers, due to their relatively uniform and smooth dispersion characteristics and broad spectral guidance, resonant dispersive wave emission can be finely adjusted across the vacuum-ultraviolet, deep-ultraviolet, and visible spectral regions by employing near-infrared pumping. However, achieving efficient energy transfer to the resonant dispersive wave requires spectral overlap between the propagating pulse and the phase-matched point [55]. For frequency shifts towards the deep and vacuum ultraviolet, a considerably broader spectrum with the necessary shorter wavelengths is required. As a result, resonant dispersive wave emission in hollow-core fibers usually arises at the point where high-order soliton compression reaches its maximum, aligning with the peak of spectral broadening. Due to self-steepening, the trailing edge of the pulse becomes increasingly steep and the spectrum becomes asymmetric. Since the generation of higher frequencies due to SPM depend on the gradient of the trailing edge, these frequencies undergo greater broadening. This effect enhances the likelihood of spectral overlap at the phase-matched point.

During generation, RDW is observed in the pulse as an oscillatory structure near the trailing edge. Since the RDW experiences normal dispersion, on the contrary to the soliton, it disperses gradually with propagation. As a consequence, the fiber length is typically chosen not much longer than the generation point, to maintain the short pulse duration of the RDW. Moreover, the employment of pressure gradients in the fiber is crucial for delivering ultrashort ultraviolet pulses to vacuum, given the high dispersion characteristics of potential window materials. A decreasing pressure gradient ensures that few-femtosecond ultraviolet pulses reach the end of the fiber and the evacuated experimental setup nearly at their transform-limited duration [65]. The theoretical framework presented in this section is the foundation for the results in chapter 5 and 6.

## 2.3 Strong-Field Phenomena

When the laser field is so intense such that it reaches a certain field strength which is comparable to the electric field of an atom ($E_{at} = 5.14 \cdot 10^{11}\,\mathrm{V/m}$ [66]), the response of the medium cannot be described by the power series of the polarization anymore [62], as in Eq. 2.15. This critical field strength corresponds to intensities around $4 \cdot 10^{16}\,\mathrm{W/cm^2}$. Ultrashort, focused laser pulses can reach this value, opening the door for experiments to study various strong-field phenomena. However, in this work, lower field strengths are used, typically in the range of $10^{14}\mathrm{W/cm^2}$. In the following, the focus lies on strong-field ionization, as it is fundamental for the generation of attosecond pulses. This section serves as the foundation for Chapter 4.

### 2.3.1 Multi-Photon and Tunneling Ionization

In the weak-field regime, the photon energy needs to be larger than the ionization potential $I_p$ of an atom in order to ionize. On the contrary, having an intense laser field with intensities above $10^{12}\,\mathrm{W/cm^2}$, different ionization processes can take place. When the field amplitude is high enough, but still smaller than the atomic field strength, photoionization can occur due to the absorption of multiple photons with photon energies smaller than the ionization potential. Depending on the photon energy, $n$ number of photons are required to overcome the ionization potential

($n \cdot E = n \cdot \hbar\omega \geq I_p$) and allow for multi-photon ionization (MPI). If the field becomes even stronger, comparable to the atomic field as mentioned above, tunneling ionization can take place. In this scenario, the Coulomb potential of the atom is modulated by the lasers electric field and the electron is not strictly bound anymore. It can be released by tunneling through this weakened barrier, described by quantum mechanics. To differentiate between these two regimes, the Keldysh parameter $\gamma_{_K}$, defined as:

$$\gamma_{_K} = \sqrt{\frac{I_p}{2U_p}}, \tag{2.36}$$

is used for classification [67]. It describes the ionization potential relative to the ponderomotive energy $U_p$, given by $U_p = \frac{e^2 E_L^2}{4 m_e \omega_L^2}$, which describes the cycle-averaged kinetic energy of a free electron with charge $e$ and mass $m_e$ in a laser field with peak amplitude $E_L$ and frequency $\omega_L$. It is often used in the form:

$$U_p[\mathrm{eV}] = 9.22\,\mathrm{eV} \cdot I\left[10^{14}\,\frac{\mathrm{W}}{\mathrm{cm}^2}\right] \cdot \lambda[\mu\mathrm{m}]^2. \tag{2.37}$$

When $\gamma_{_K} > 1$, the dominating process to release an electron is MPI. On the contrary, for $\gamma_{_K} \ll 1$, the ponderomotive energy is larger than the binding energy due to the extremely strong laser field, and tunneling ionization dominates. The two phenomena are visualised in Fig. 2.3.

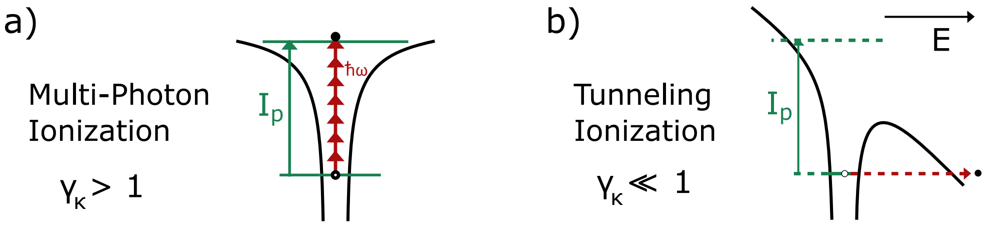

Figure 2.3: a) Multi-photon ionization: When the laser with photon energy $E = \hbar\omega$ is very intense, the absorption of multiple photons can occur and ionize the medium, generating free electrons. b) Tunneling Ionization: The electric field $E$ of the laser modulates the Coulomb potential and the electron can be released via tunneling.

The ionization rate $\Gamma$ for multi-photon ionization is proportional to $I^n$ [68], the laser intensity to the power of number of photons. To describe the ionization rate for tunneling ionization due to strong fields, the ADK-theory by Ammosov, Delone and Krainov can be used, stating $\Gamma \propto \exp(-2\sqrt{(2I_p)^3}/3E(t))$ [69].

Next to these two major cases, we can define other effects: On the one hand, a regime beyond the tunneling ionization exists, at even higher field strengths. In that case, the potential barrier is completely suppressed, below the binding energy. This regime is not relevant for this thesis. On the other hand, in the regime below MPI, linear ionization by single photon absorption can take place.

In the middle regime, between MPI and tunnel ionization, when $\gamma_K$ is around 1, the atom can absorb more photons than needed for MPI, meaning that an already ionized atom can absorb photons. This phenomenon is called above threshold ionization (ATI) and leads to the release of electrons containing the photons excess energy plus the energy from the additionally absorbed photons.

### 2.3.2 High Harmonic Generation

High harmonic generation (HHG) describes the process where a strong laser field is influencing a material in such a way that it emits photons with energies of $n$ times the fundamental photon energy, referred to as harmonics. High harmonics can be generated in solids, liquids, plasmas and gases, but the focus in this work lies on the latter. In that case, HHG can be described by the three-step model, also known as simpleman's model: a semi-classical, single-atom description. Here, we assume a linearly polarized laser field that initiates this process. As the name says, the generation can be divided into three steps:

1. **Tunneling Ionization**: the laser pulse is focussed into gas (typically noble gas) and distorts the Coulomb potential. Then, an electron, described quantum mechanically as electronic wavepaket, can tunnel through the potential barrier with highest probability at the peak of the oscillating laser field. Directly after release (or birth), the electron has zero velocity.

2. **Acceleration**: the electron is accelerated away from its parent ion by the laser field for roughly a quarter field period. The motion can be described classically via $\vec{a} = -e\vec{E}(\vec{r}, t)/m$, assuming the Coulomb potential can be neglected therefore after birth (strong-field approximation: SFA). Since the field changes direction over time, the electron is influenced accordingly and can return to its parent ion, while being further accelerated. It accumulates kinetic energy $W_{kin}$ corresponding to the acceleration duration.

3. **Recollision**: When the electron returned to its parent ion, recombination can take place, leading to emission of a photon with an energy of $\hbar\omega = I_p + W_{kin}$, which is typically extreme ultraviolet (XUV).

The three steps are visualized in Fig. 2.4.

Corkum [70] found the maximum kinetic energy the electron can reach to be

$$E_{cutoff} = \hbar\omega_{max} = I_p + 3.17\, U_p, \tag{2.38}$$

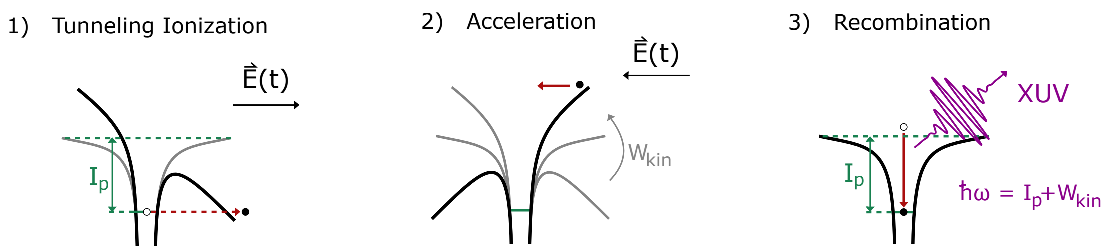

Figure 2.4: The 3-step model is used to describe high harmonic generation in the single atom response and consists of first, tunneling ionization due to an intense laser field, second, acceleration of the electron and third, recombination with its parent ion and photoemission of an XUV photon.

with the ponderomotive energy $U_p$ depending on the lasers intensity and wavelength as stated in Eq. 2.37. As HHG requires tunnel ionization, the ionization potential $I_p$ of the gas has to be chosen much smaller than $U_p$ to fulfill $\gamma_K \ll 1$.

The third step, recollision, cannot only feature the recombination of the electron with its parent ion, inducing the emission of an XUV photon, but also other processes, such as electron-rescattering, non-sequential double ionization, or incoherent recombination and Bremsstrahlung. Moreover, when an electron is emitted significantly before the laser field peak, this so-called direct electron just escapes, without further interaction with the parent ion. Thus, timing is crucial for HHG, which is based on the first mentioned recombination and photoemission process. Therefore, the related details are explained below.

The three-step model describes the process for a single atom. However, in the macroscopic picture, the generation takes place in gas, consisting of many atoms, as shown in Fig. 2.5 a). Hence, many photons are emitted around similar timescales at similar places. In order to achieve the emission of coherent radiation as high harmonics, the phases of all the emitted XUV fields have to be matched. The phase mismatch depends on the difference of the wave vectors of the driving field and the HHG radiation and has to be cancelled out. The phase difference depends on the fraction of ionized gas atoms and can thus be tuned by the geometry, gas pressure, density, type, and laser intensity [71], e.g. by moving the gas out of the laser focus.

As emission can take place around every laser peak, it happens every half cycle of the field $T/2 = \omega$. When laser field is long, emission takes place again and again, leading to a pulse train (see Fig. 2.5 c)). The radiation is interfering, leading to only odd order harmonics with frequency $2\omega = T$. This effect results in the typical HHG spectrum, as shown in Fig. 2.5 b). It exhibits a plateau-behaviour until the cutoff energy $E_{cutoff}$ (Eq. 2.38).

The electron trajectories (Step 2) depend on the time of birth relative to the electric field, as shown in Fig. 2.5 d) and e). When the electron is emitted slightly after the peak of the laser field it can recombine with maximum kinetic energy $3.17\,U_p$, also called cutoff energy, as shown as blue trace in Fig. 2.5 d). When an electron is emitted slightly before, earliest exactly at the laser peak, it propagates on a longer pathway and recombines later, with less kinetic energy. This case is referred to as long trajectory. When it is emitted even earlier, it cannot recombine (direct electron). On the other hand, when the electron is emitted later, following a short trajectory, it returns earlier and also with less kinetic energy. Depending on the moment of ionization, the electrons recombine roughly 3/4 cycles later, around the zero-crossing of the field.

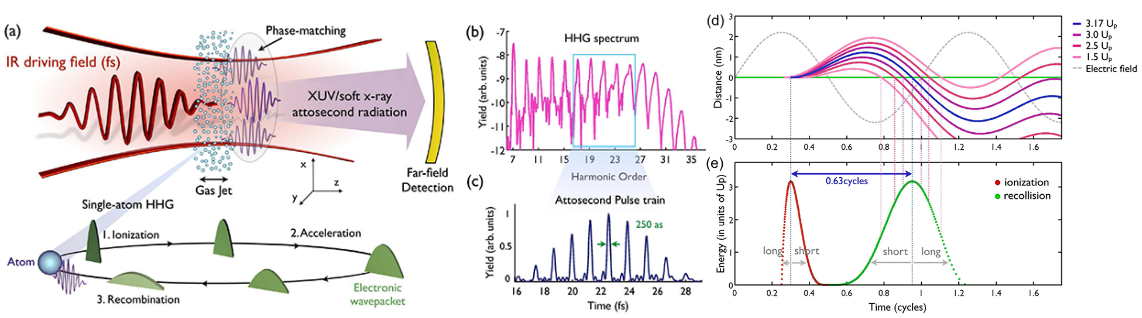

Figure 2.5: a) High harmonic generation in the macroscopic and microscopic picture. The macroscopic case shows the IR driving field focused into a gas jet, leading to the emission of XUV photons. This can be explained microscopically (single-atom) with the 3-step-model. The emitted XUV radiation interferes which leads to odd high-order harmonics, as visible in the spectrum shown in (b). Photon emission takes place every half-cycle, resulting in an attosecond pulse train (c). Depending on the emission times of the electrons, they can follow different trajectories (d). The optimal trajectory leads to the maximum kinetic energy of the electron of $3.17\,U_p$. Electrons on short trajectories return later to the parent ion, while electrons following longer trajectories return earlier (e), but both cases enable lower kinetic energies. When electrons are emitted before or after the shown trajectories, they cannot recombine with their parent ion. Reprinted from [72].

The shorter the driving pulse is, the fewer the number of photoemission events, and the shorter the HHG pulse train can be. For instance, a few-cycle IR driving field as shown in Fig. 2.6 only leads to four photoemission events.

Since the energy of the emitted photons depends on $U_p$, and thus the laser field, it depends on the amplitude of the laser oscillations. Hence, the half-cycle with the largest amplitude leads to emission of the most energetic photon (as shown via the color-coding of the XUV radiation in the figure above), meaning that only a single attosecond pulse exists within the pulse train which contains this cutoff frequency. This fact is used to isolate an attosecond pulse by spectral filtering the cutoff energy. It refers to the filtering of the emission due to the strongest half-cycle and is therefore called amplitude gating.

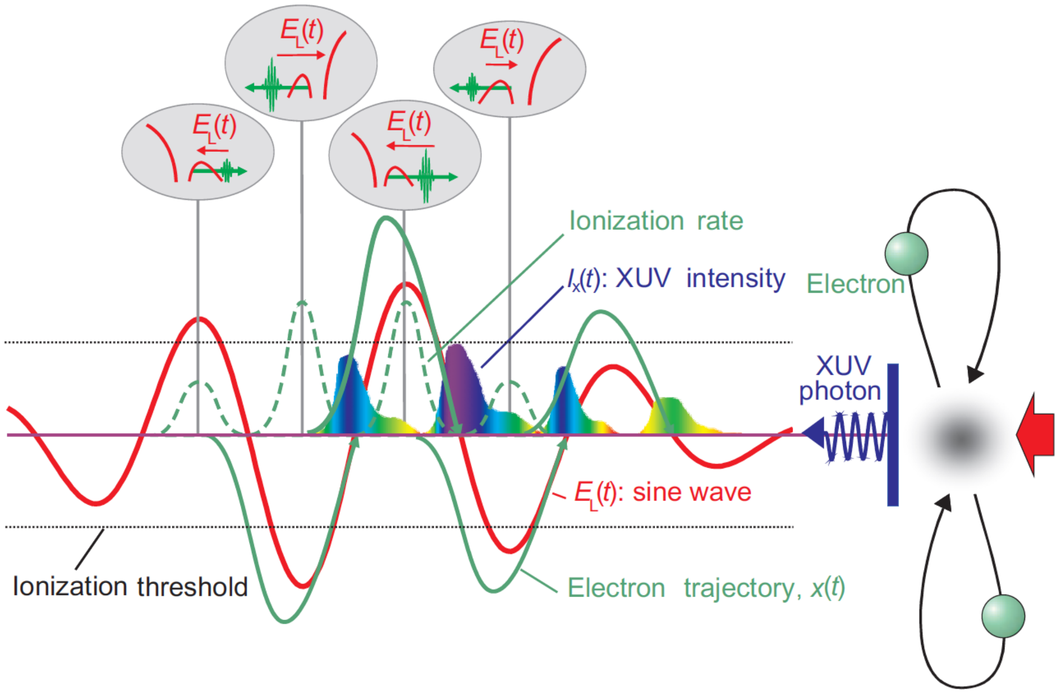

Figure 2.6: High Harmonic generation during the time of an 5-fs NIR laser pulse. The electric field $E_L(t)$ is a sine wave, shown in red. When the amplitude of a sub-cycle is large enough, above the ionization threshold, electrons can tunnel out of the gas atoms, get accelerated and recombine with their parent ions around three quarters later. The ionization rate is visualized in green dotted lines, as well as the corresponding optimal free electron trajectory in green solid lines. The emitted XUV photons contain several frequencies, as shown in different colors at different times, depending on the amplitude of the accelerating half-cycle and the electron trajectory. Only the strongest half-cycle can generate the cutoff-frequency (purple here). Reprinted from [7].

# Chapter 3

# Experimental System and Methods

This chapter presents the experimental foundations for the conducted measurements in this PhD work. As explained in the previous chapter, having the full electric field information of an ultrashort laser pulse can provide information about its generation and interaction with a medium. The here utilized laser pulses are on the ultrashort timescale of a few femtoseconds ($1\,\mathrm{fs} = 10^{-15}\,\mathrm{s}$) or hundreds of attoseconds ($1\,\mathrm{as} = 10^{-18}\,\mathrm{s}$), which corresponds to a frequency of hundreds of THz or even 1 PHz ($= 10^{15}\,\mathrm{Hz}$). In order to resolve such ultrafast processes, an even shorter event is needed. Since conventional electronics are performing with a speed in the GHz range ($10^{9}\,\mathrm{Hz}$), faster measurement techniques are needed. Here, we use the ultrashort laser pulses themselves to measure other ultrashort laser pulses.

The used experimental laser setup, located in the Laboratory for Attosecond Physics in the Max-Planck-Institute of Quantum Optics in Garching, is presented in detail in Section 3.1. With this laser system various field-resolved metrology experiments were performed and compared in this thesis, all delivering the electric field of a laser pulse including its phase information, but in different circumstances. In attosecond streaking, described in Section 3.2.1, attosecond XUV pulses are acting as a gate to scan along the electric field of the fundamental visible to near-infrared (VIS-NIR) femtosecond pulses in a pump-probe scheme. This metrology technique, often referred to as the attosecond streak camera became the foundation for field-resolved measurements of ultrafast electron dynamics in atoms, solids and molecules all over the world [4, 22, 25, 28, 30].

Another metrology technique called photoconductive sampling, also uses a pump-probe configuration, but is based on measuring the current of the gated photoelectrons. It is presented in Section 3.2.2 and can be used for different wavelengths and intensities. Generally, it has to be differentiated in linear and nonlinear photoconductive sampling (LPS and NPS, respectively), depending on the gate pulse and sample. Both methods are presented below in detail. The linear configuration (LPS) uses a similar environment as attosecond streaking, while XUV radiation is not needed in the nonlinear configuration, enabling smaller and more flexible setups.

These first two techniques, LPS and streaking, are experimentally compared in Chapter 4, measuring VIS-NIR laser fields, but showing that different XUV energies are favoured. The third technique, NPS, can cover different photon energies and is therefore used and advanced in Chapter 6, pushing the bandwidth limit to fully cover the DUV - NIR.

## 3.1 Phase-Stable Laser Source

All experiments have been performed using the femtopower laser system FP3, which is based on a titanium-sapphire chirped pulse amplification system from *Femtolasers*, now *Spectra-Physics*. The setup is shown in Fig. 3.1, and will be explained along the laser beam path, from the bottom right to the upper left.

The first element is the titanium-sapphire oscillator which is pumped by a *Verdi* V6, a continuous-wave (CW), frequency-doubled Nd:YVO$_4$ laser from *Coherent* emitting at 532 nm. The V6-output is modulated by an acusto-optic modulator (AOM). The oscillator is passively mode-locked and delivers a pulse train centred around 780 nm. The pulses have energies of 2.4 nJ, durations of $\sim$ 8 fs, and a repetition rate of 78 MHz. The laser beam exits the cavity at the outcoupling (OC) mirror and enters the monolithic carrier-envelope-offset phase (CEP) stabilisation unit [74], which consists of a f-0f interferometer. This so-called fast loop uses periodically-poled lithium-niobate (PPLN) in which self-phase modulation (SPM) and difference frequency generation (DFG) occur at the same time. In the region of spectral overlap the broadened fundamental (f) and the DFG signal (0f) interfere with each other and produce a beat signal, which is detected by a fast photodiode. This signal is coupled to the AOM, where the amplitude of the pumplaser is modulated such that the CEP is stabilized. After the PPLN, the majority of the beam is sent via a beamsplitter to the chirped pulse amplification (CPA) unit [75].

In this scheme, the pulses get stretched first, then amplified and afterwards compressed again. Here, the stretcher consists of a 13.5 cm long SF57 glass and glass wedges. It lengthens the pulses to $\sim$ 1 ps. They propagate then through the multi-pass Ti:Sa amplifier, being pumped by a DM30, which is a frequency-doubled Nd:YLF laser at 527 nm from *Photonics Industries*. After the first four passes the beam is sent through a Pockels Cell (PC) which acts as a pulse picker and reduces the repetition rate to 4 kHz. Subsequently, a Dazzler, which is an Acousto-Optic Programmable Dispersive Filter (AOPDF) from *Fastlite*, corrects for higher-order dispersion effects. The pulses get amplified more by passing the Ti:Sa crystal another five times, delivering pulses with energies of 1 mJ and a reduced spectrum (due to

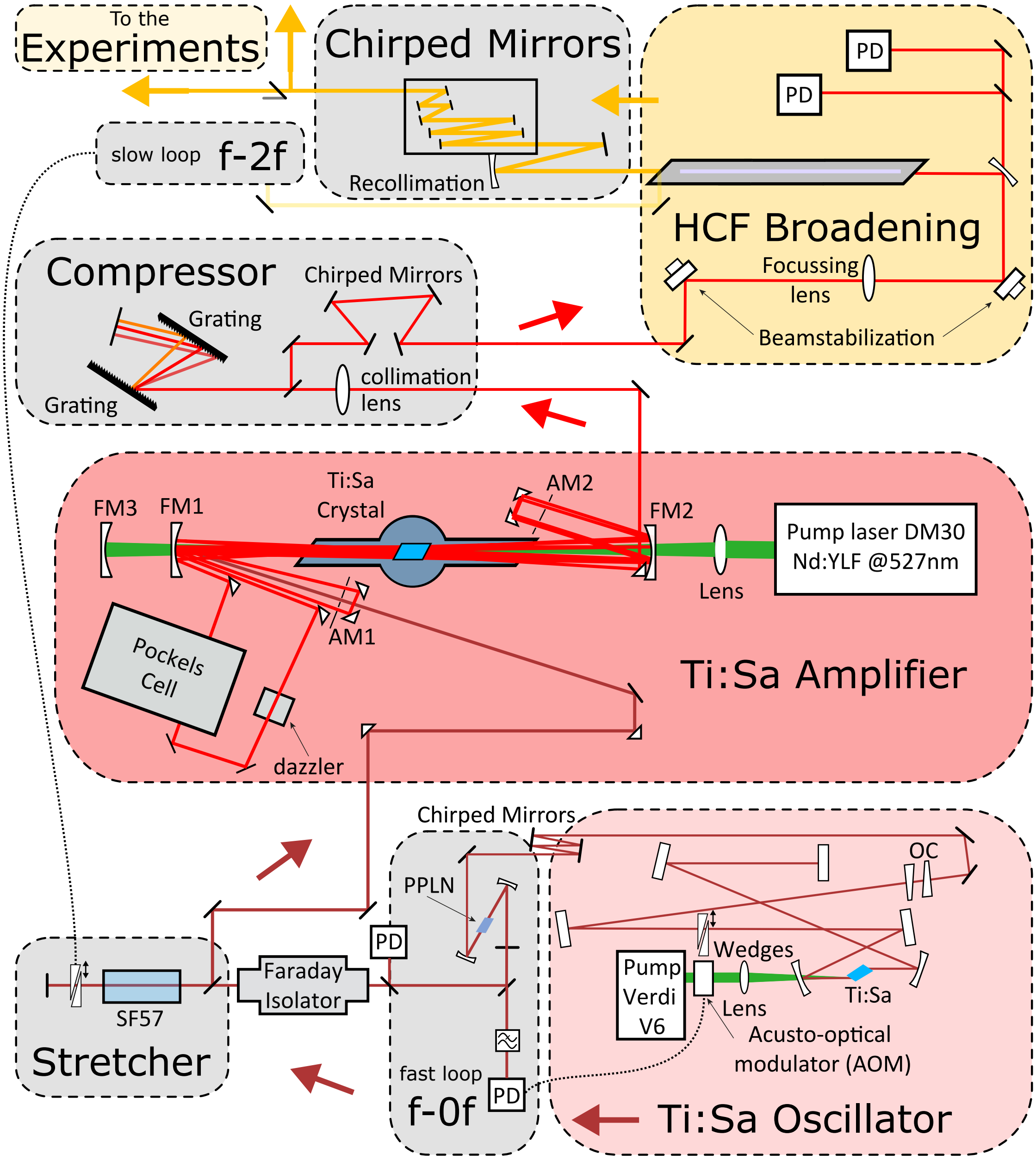

Figure 3.1: Setup of the FP3 laser system consisting of a Ti:Sa oscillator, a chirped pulse amplifier (stretcher, Ti:Sa amplifier and compressor), a spectral broadening stage in a gas-filled hollow-core fiber and subsequent pulse compression, leading to $< 4$ fs pulses centred at 780 nm and with a repetition rate of 4 kHz. The pulses are CE phase-stabilized via two interferometric loops. The scheme is adapted from [73]

gain-narrowing) spanning from ∼ 750 nm to 830 nm. These pulses get temporally compressed by two transmission gratings and chirped mirrors to ∼ 20 fs, being close to the Fourier limit.

Thus, in order to get even shorter pulses, the spectral bandwidth needs to be extended. In this setup, new frequencies are generated due to SPM in a 1.5 m long gas-filled hollow-core fiber (HCF). The beam is focussed and actively, spatially stabilized to constantly hit the entrance of the HCF core centred. The HCF is mounted in a gas tube which is filled with 1.6 bar neon and sealed with two thin windows. As a result of this broadening stage, the extended spectrum reaches from 350 nm to 1100 nm. The pulses get compressed by passing through four pairs of chirped mirrors (CMs), leading to pulses shorter than 4 fs. Due to the limited bandwidth of the CMs, the spectrum reaches then from ∼ 400 nm to 1050 nm. A small fraction of the beam is reflected from the exit window and used for the slow loop. In a typical f-2f interferometer the second harmonic (2f) is generated in a BBO crystal and interferes with its fundamental (f). This signal is coupled to the wedges in the stretcher unit, which enables the compensation of slow CEP drifts and fine-tune to a desired CEP.

These braodband, phase-stable and ultrashort pulses are sent either to the attosecond beamline for XUV generation and streaking or to the DUV-RDW setup with photoconductive sampling. Both are explained in more detail in the following. Due to its sensitivity the system required constant maintenance, which was a big part of this work.

## 3.2 Field-Resolved Metrology Techniques

In order to study ultrashort field-dependent light-matter interactions, it is crucial to be able to directly measure the electric field oscillations of light. In the following, the field sampling techniques used in the framework of this thesis are explained. First, attosecond streaking is presented in Section 3.2.1. Secondly, both types of photoconductive sampling (linear and nonlinear) are explained in Section 3.2.2. Generally, to measure an ultrashort pulse with a good time resolution, an event that is even shorter is needed. Therefore, in the following, either an even shorter laser pulse is directly used as a scanning gate, or a nonlinear interaction leading to a shorter gate due to its nonlinearity. Then, with a time delay scan, the full electric field can be recorded.

### 3.2.1 Attosecond Streaking

#### Concept

Attosecond streaking is a special pump-probe scheme that uses isolated attosecond XUV pulses to measure a femtosecond VIS-NIR probe field, hereafter referred to as NIR pulse for simplicity. The significantly shorter XUV pulse can be scanned along the NIR probe pulse by small changes of the time delay $\tau$. The principle is often called 'streaking camera' and visualized in Fig. 3.2 a) with the XUV pulse in purple and the NIR pulse in red.

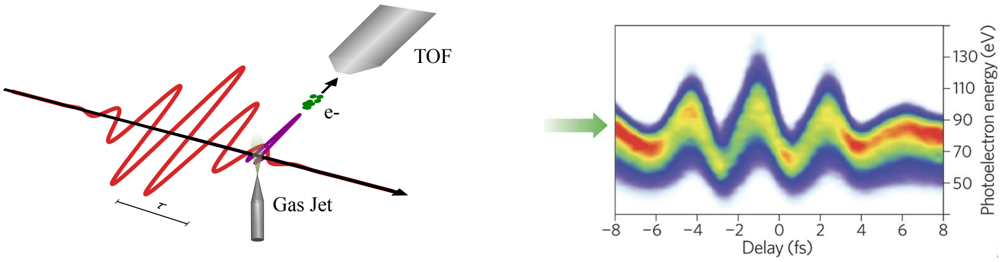

(a) Attosecond streaking camera scheme (b) Typical streaking spectrogram [76]

Figure 3.2: Scheme for an attosecond streaking camera (a) and the resulting spectrogram (b). An attosecond XUV pulse ionizes gas, leading to free electrons in a vacuum chamber. The time-of-flight (TOF) spectrometer detects the time from emission of the electrons until arrival at the spectrometer, such that the electron velocity and thus the kinetic energy can be determined. Depending on the time delay $\tau$ between pump and probe pulse, the electron momentum is modulated. By scanning the time delay along the whole probe pulse, the time-dependent electron kinetic energy and thus vector potential of the probe pulse is mapped and visualized in a typical spectrogram, taken from [76]).

Experimentally, the two beams are focused collinearly onto a gas jet, typically containing noble gas. The attosecond XUV pulses cause quasi-instantaneous ionization of the gas atoms via linear photo ionization due to the high photon energies. The free electrons emitted at the time of ionization $t_0$ then have a kinetic energy $E_0$ that corresponds to the XUV photon energy minus the ionization potential $I_p$ of the gas:

$$E_{0,kin} = E_{XUVphoton} - I_p = \frac{p_0^2}{2m} \tag{3.1}$$

Thus, after emission, the electrons with mass $m$ propagate through vacuum with a certain momentum $p_0$ depending on the XUV photon energy and choice of gas (different $I_p$). The electron momentum is further affected by the electric field $E(t)$ of the probe pulse, resulting in a certain gain or loss of the electron momentum, and thus an acceleration or deceleration of the electron. Generally, the electric field of a laser pulse can be defined via its vector potential $A(t)$ as $E(t) = -\frac{\partial A(t)}{\partial t}$. Hence, the additional momentum given by the probe can be written proportional to the probe vector potential as follows:

$$p_{probe} = \int F\,dt = -\int eE\,dt = -eA(t). \tag{3.2}$$

At the time of electron emission $t_0$, the probe vector potential can be assumed to be quasi-stationary $A(t_0)$ due to the ultrashort, quasi-instantaneous ionization through the pump. As a consequence, the final momentum of the electrons $p_{final}$ emitted at $t_0$ is given as the initial momentum $p_0$ plus the probe momentum at $t_0$:

$$p_{final} = p_0 + p_{probe,0} = p_0 - \int_{t_0} eE\,dt = p_0 - eA(t_0) \tag{3.3}$$

Measurements of the electron velocity $v$ with a time of flight (TOF) spectrometer at a certain distance $l$ to the interaction area gives access to the kinetic energy of the electrons

$$E_{kin} = \frac{1}{2}mv^2 = \frac{1}{2}m\left(\frac{l}{(t-t_0)}\right)^2, \tag{3.4}$$

where $t$ is the time of arrival at the spectrometer detector and $t_0$ is the time of ionization. By scanning the time delay, the electron kinetic energy at each ionization instance is measured, and stitching them together leads to the complete spectrogram as shown in Fig. 3.2 b). With $E_{final} = \frac{p_{final}^2}{2m}$ the momentum and hence via Eq. 3.3, the vector potential $A(t)$ of the probe, or so-called streaking pulse, can be determined. Taking the time derivative of the probe leads to direct access of the electric field $E(t)$. For this technique, it is crucial that the probe field does not change over time, meaning that the CEP needs to be stabilized and drifts should be minimized.

For optimal resolution, the gate pulse should be as close as possible to a delta function. Hence, isolated, unchirped attosecond pulses should be used. Typically, attosecond gate pulses are generated via high harmonic generation (HHG, see Chapter 2.3.2) and their fundamental pulse is used as the probe or so-called 'streaking' pulse. Having both beams from the same source directly provides optimal time synchronisation. However, as explained with the illustration in Fig. 2.6, depending on the length of the fundamental pulse, the process typically results in emission of an attosecond pulse train, with attosecond pulses initiated by each half-cycle of the fundamental that exceeds the ionizing threshold. In order to receive an isolated attosecond pulse, this pulse train has to be filtered before the streaking setup, as explained in section 2.3.2.

From the streaking spectrogram, which shows the electron momentum or kinetic energy vs. time delay, also the temporal structure of the attosecond XUV pulse can be retrieved by studying the shape of the electron momentum distribution depending on the time-delay. Methods like the ptychographic reconstruction algorithms [77] or frequency-resolved optical gating for the complete reconstruction of attosecond bursts (FROG-CRAB) [78, 79] are commonly used for the extraction of pulse information from the streaking spectrogram.

### Experimental Setup

As mentioned above, the required attosecond gate pulses are typically generated via high harmonic generation (see Chapter 2.3.2) and their fundamental pulse is used as the streaking pulse. After HHG, the two beams are propagating together. In order to introduce a time delay between them, they are split into two arms. The pulses pass through approximately the same path length, while one of the beam paths comprises a delay stage to perform the delay scan as explained above. Typically, the XUV arm is spectrally filtered by either transmission through a metallic filter and / or reflection from a multilayer mirror with specific spectral reflectivity. After recombination, the beams are collinearly focused into the gas jet for attosecond streaking.

In this work, the existing attosecond beamline *AS 2*, shown in Fig. 3.3, was used to perform attosecond streaking. The corresponding results are presented in Chapter 4. The beamline *AS 2* starts at the end of the FP3 setup (see Fig. 3.1) and guides the beam through three vacuum chambers. The first chamber is the HHG chamber on the left. There, the beam is focused into a ceramics gas target with a opening diameter of 300 µm. In the presented experiments, the target is filled with 25 mbar of argon. The generated high harmonics (HHs) propagate together with the fundamental, NIR beam into the second chamber, the so-called delay chamber in which the beams are separated and recombined again with a chosen, adjustable time delay.

Since the XUV beam is less divergent than the NIR beam, the beams can be spatially separated with a perforated mirror. Here, the XUV radiation passes through the hole in the center of the mirror that has a 1.5 mm diameter. As a consequence, the reflected beam has a doughnut shape and only consists of the more divergent NIR radiation. This beam runs through a delay stage, and passes an intermediate focus, while the HHs can be sent to diagnostics such as an XUV CCD camera. With the CCD camera, either the beam profile of the XUV can be studied or the spectrum, when passing a grating beforehand. Despite the option to send the beam to the camera for diagnostic purposes, it usually passes a metallic filter for cutting the spectrum and hence the pulse length (as explained in Section 2.3.2 and in the conceptual explanation of streaking above), and the corner mirror, which is an

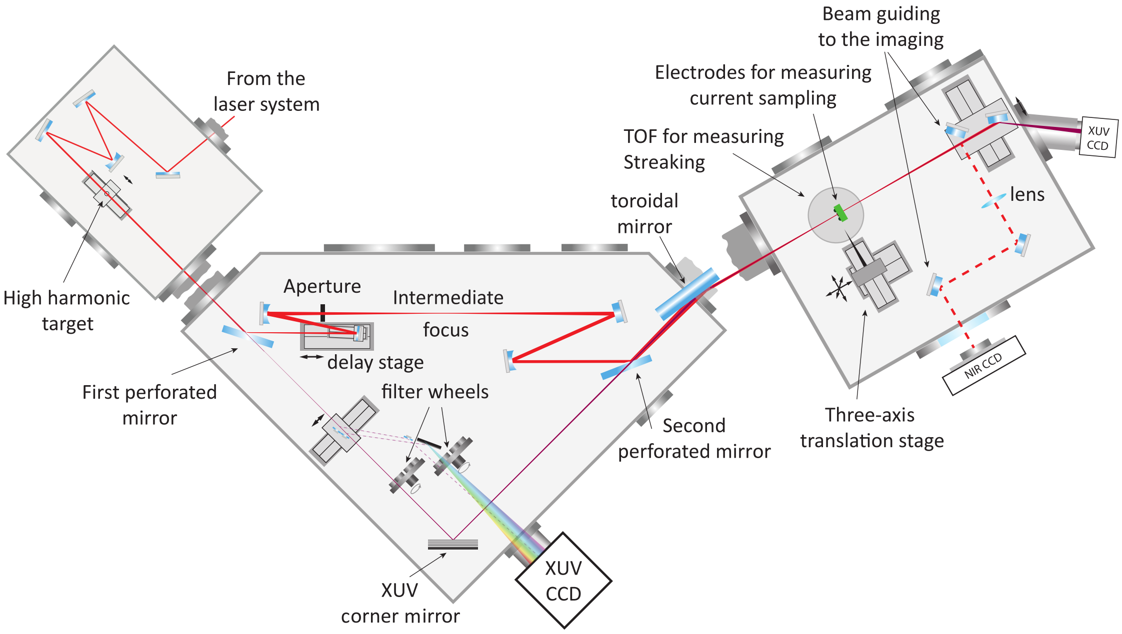

Figure 3.3: AS2 beamline with three chambers. In the first chamber (going from left to right) HHG takes place in a gas jet. In the second (triangular) chamber the high harmonics (HHs) get separated from the fundamental beam and recombined with perforated mirrors. The time delay between the two pulses can be adjusted with a delay stage in the IR arm. The XUV beam passes appropiate filters and can be sent to diagnostic tools such as the CCD camera for signal optimization. At the end of this chamber, the combined beam is focused into a gas jet in the third chamber, the experimental chamber. A TOF spectrometer is attached in order to measure the vector potential of the NIR pulse. Electrodes can be used for linear photoconductive sampling. The remaining beam can be sent to further diagnostics. Adapted from [10].

unprotected gold mirror in the presented experiments.

At the end of the chamber, the beams are recombined using another perforated mirror and focused with a toroidal mirror into a gas jet in the third chamber, the experimental chamber. For the streaking and field sampling experiments, the gas nozzle is filled with neon. Along the polarization axis of the streaking pulse, a TOF spectrometer is mounted next to the gas nozzle and laser focus. In this work in chapter 4.1, attosecond streaking is simulatenously performed with linear photoconductive sampling (LPS). The latter is explained in the following. For LPS, an electrode is placed on translational stages (x,y, and z) on the opposite site of the focus than the TOF spectrometer. The gas nozzle, which is mounted on the same stage is adjusted to the laser focus precisely every measurement run. More diagnostics are connected to this chamber, accessible by a movable mirror. The XUV beam can be studied with another CCD camera, while the NIR beam can be sent outside to a camera and or a spectrometer. These diagnostics are used to optimize the spatial and temporal overlap of the two pulses.

### 3.2.2 Photoconductive Sampling

Photoconductive sampling is an alternative method to measure the electric field of light, based on optical switching of electronic currents. First known as the *Auston switch*, this switching concept was used in 1975 to measure picosecond THz transients [42]. In 2013, optical-field-induced currents have been measured in dielectrics even with sub-femtosecond control [44]. This findings opened the door for direct sampling of electric transients with larger bandwidths. In 2020, researchers measured waveforms of electric fields from the UV to MIR range and benchmarked photoconductive sampling with attosecond streaking [10]. The interferometric photoconductive sampling setup can be built much more compact than the beamline needed for attosecond streaking. Moreover, the optically-induced current measurements have been conducted in various materials, e.g. in dielectrics [44, 80], in nanoantennas [47], as well as in gases [11, 81]. The experiments in solids are usually performed close to the damage threshold for the highest possible signal. The gas medium has the advantage that it cannot be damaged and the current signal can be optimized by variation of laser intensity and gas pressure.

The working principle of photoconductive sampling is as follows: an injection pulse excites a medium for a very short duration and hence, changes the charge distribution forming a temporal gate. In solid samples charges are excited from the valence into the conduction band and in gases atoms are ionized, corresponding to a charge redistribution from bound to free electrons. A second pulse drives these newly generated free electrons, leading to an externally measurable photocurrent. This pulse is called drive pulse in the following. The medium is surrounded with electrodes that measure this drift current $I_{drift}(\tau)$. The understanding of how the microscopic electron dynamics lead to a macroscopic current signal has been under discussion. Generally, a measurable current can occur due to charge carriers that directly hit the electrodes or due to the formation of a macroscopic dipole between the electrodes. Certain models described the emergence of the current due to dipole contributions [11] and others due to direct photocurrent [44]. Only recently, a unified model based on the Ramo-Shockley theorem has been published. It provides a more complete description, also including the influence of effects like electron-neutral scattering and mean-field charge interactions [81].

The external measured drift current $I_{drift}(\tau)$ represents the vector potential of the drive pulse $A_{drive}(t)$, given by

$$I_{drift}(\tau) = \frac{e^2 N_{at}}{m_e} \int_{-\infty}^{+\infty} A_{drive}(t) G_{gate}(t-\tau)\, dt \tag{3.5}$$

where $e > 0$ is the elementary charge, $m_e$ is the electron mass, $N_{at}$ is the concentration of atoms and $\tau$ is the time delay between the two pulses. The gating function $G(t-\tau)$ describes the excitation dynamics of the medium which are proportional to the ionization rate due to the injection pulse. In order to have a meaningful measurement of the drive field, the gating function has to be significantly shorter than the driving field, at least shorter than a half cycle. Then, the current $I(\tau)$ at each time delay $\tau$ represents the vector potential of this drive pulse $A_{drive}(\tau)$ with $\frac{d}{d\tau} I(\tau) = -A'_{drive}(\tau) = E_{drive}(\tau)$. In the frequency domain, the current can be simplified to

$$I_{drift}(\omega) = \frac{e^2 N_{at}}{m_e} A_{drive}(\omega) G_{gate}(\omega) \tag{3.6}$$

where $G(\omega)$ is the spectral response function [82] (see appendix for details A.2).

Depending on the injection mechanism, we distinguish between linear photoconductive sampling (LPS) and nonlinear photoconductive sampling (NPS). If the photon energy is large enough to overcome the bandgap or ionization energy, single photon absorption is sufficient and the medium is linearly excited or ionized. This is depicted in Fig. 3.4 a) in a gas medium, as experimentally used in this work. If the photon energy is smaller, the gas can be ionized via multi-photon absorption (see Fig. 3.4 b)). This nonlinear process requires high injection intensities. To ensure that the actions of the two pulses are separable and the influence on the other is negligible, they have to be cross-polarized in NPS. Then, the driving pulse is polarized parallel to the electrodes such that a dipole is generated along that axis. The injection pulse is polarized perpendicular to the electrodes and will thus not influence the measured photocurrent. Moreover, the driving pulse should not inject any charges itself, which is realized by low drive intensities. This also holds for LPS, where the ionization energy is too large for a weak drive beam with smaller photon energies to generate free electrons.

a) Linear Photoconductive Sampling

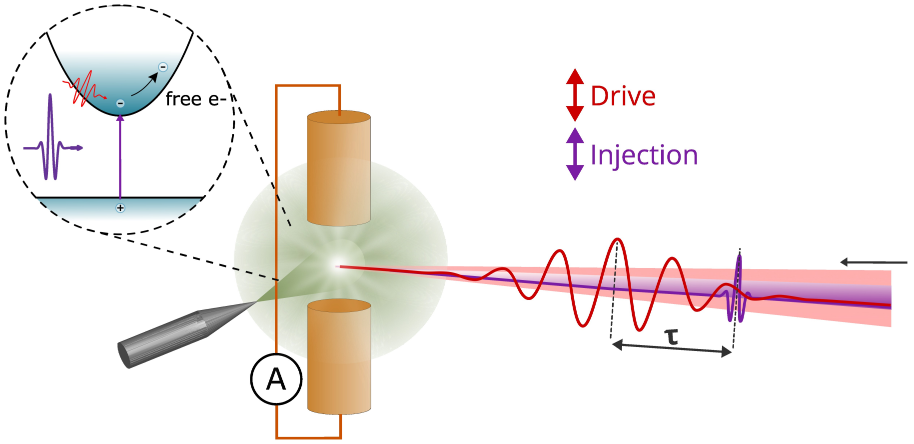

b) Nonlinear Photoconductive Sampling

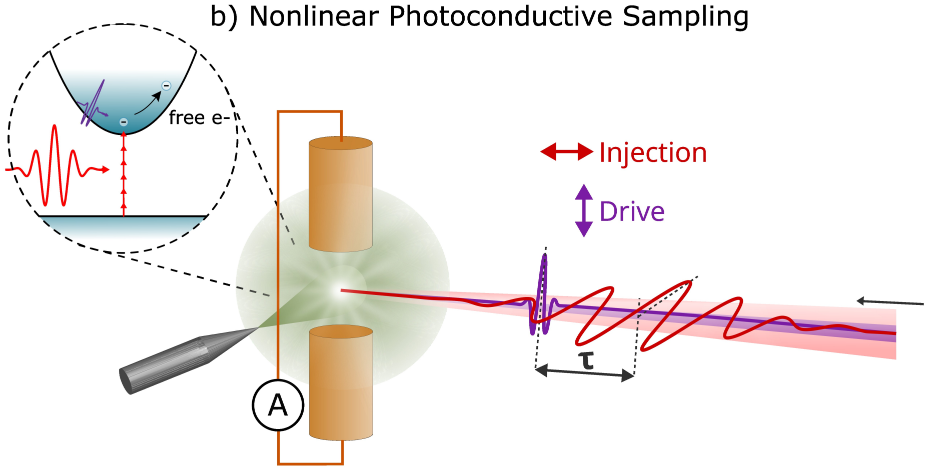

Figure 3.4: Linear (a) vs. nonlinear (b) photoconductive sampling (LPS vs. NPS) in a gas medium. In (a) the gas atoms are ionized with a single-photon absorption of a high energy ((X)UV) injection pulse with energies larger than the ionization potential of the gas, freeing the bound electrons. The drive pulse (NIR) drives the generated charges towards the electrodes. In (b) the medium gets ionized via multi-photon absorption of the NIR injection. The charges can be driven by the same pulse or even shorter pulses with shorter wavelengths (UV), as long as the gating function is sufficiently short. Adapted from [83].

The gating function strongly depends on the type of injection. In the linear case, it is approximately proportional to the injection pulse intensity: $G_{LPS} \propto I_{inj}$, and thus also the pulse length of the injection pulse. A typical ionization rate in the case of a 3 fs NIR pulse is shown on the left side of Fig. 3.5 in red. Generally, an injection in the form of a delta function would be optimal, leading to a single step ionization. In order to optimize the LPS ionization rate, shorter pulses with shorter wavelengths (as shown in magenta) can be used as injection pulses, such as the XUV pulses from HHG.

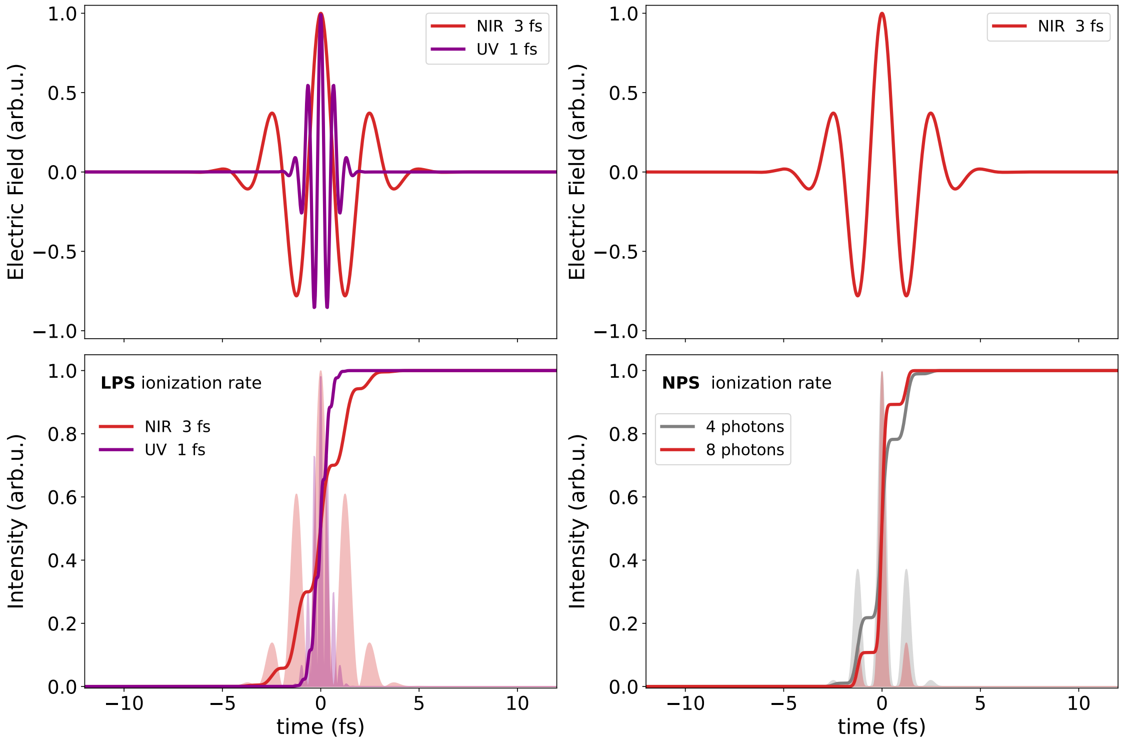

Figure 3.5: The influence of different types of injections and different parameters on the ionization rate and hence, the gating function. On the left side, the case of linear injection (LPS) is shown, while on the right side nonlinear injection (NPS) is covered. In the upper plots the electric field for these calculations are shown. In LPS the gating function depends on the pulse intensity (filled area behind). In contrast, the NPS gating function depends on the number of photon involved in the nonlinear absorption. The more photons involved the steeper the rate. Thus, with the correct settings, an NIR pulse can be used as injection in NPS to measure itself, while LPS need much shorter injection pulses to resolve NIR fields.

In the nonlinear case, the part of the gating function influenced by the ionization rate depends on the rate of energy deposition and thus, on the degree of multi-photon absorption $G_{NPS} \propto E_{inj}^{2n}$ [10], where $n$ is the number of absorbed photons. On the right side of Fig. 3.5 the influence of the number of photons involved on the ionization rate is visualized. The more photons are absorbed, e.g. in a larger bandgap material and with very high intensities, the steeper the ionization rate. It is clearly visible that in NPS the main peak of the electric field has the largest influence. In contrast, in LPS the weaker oscillations on the sides are much more pronounced, which leads to a longer temporal gate and thus, less temporal resolution. Because of that, to resolve NIR fields, a shorter injection pulse is needed for these LPS measurements. On the other hand, for NPS high photon energies are not necessarily needed for the injection. The settings can be chosen such that the temporal gate here can be much shorter than the pulse length, since only the high intensities at the main peak of the electric field can lead to high-order multi-photon absorption.

Furthermore, the CEP has a big influence on the temporal gate. As explained in chapter 2 one can have different electric fields with the same envelope, e.g. a sine vs. a cosine, but differing by the CEP. A cosine waveform with one maximum peak in the center can lead to a cleaner injection than a sine waveform which has two equally strong field maxima. This enables measurements of the beam itself, or measurements of driving pulses that are shorter than the injection pulses. As a consequence, also shorter wavelengths such as the ones in the UV regime can be resolved if the gating function is short enough, following the Nyquist-Shannon theorem [84]. The most simple NPS setup, where the beam measures itself, is shown in Fig. 3.6.

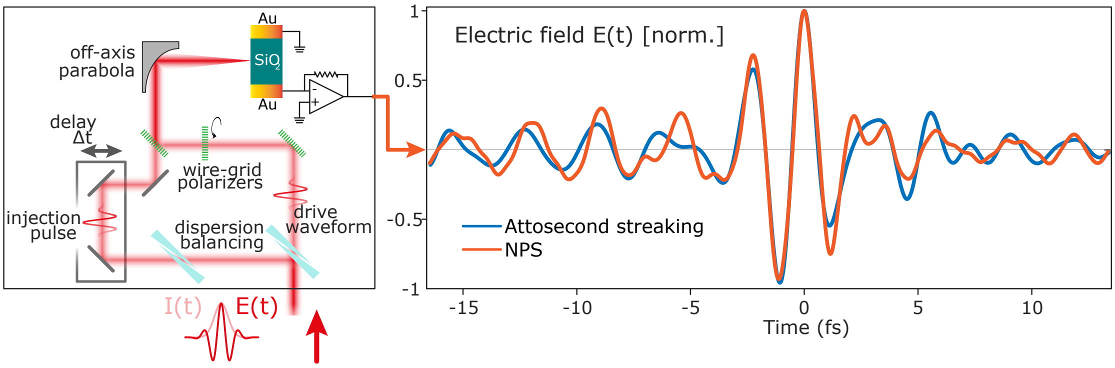

Figure 3.6: Typical NPS setup and the acquired electric field of the drive field, compared to the field measured via attosecond streaking. The setup visualizes that the beam is separated into a strong injection pulse and a weak drive pulse, each independently tunable in CEP with wedges. One of the beams is rotated in polarization such that they are cross-polarized. After recombination the beam is focused into the NPS sample, which is fused silica ($SiO_2$) in this case, surrounded by two electrodes. The measured current is amplified with trans-impedance amplifiers and the signal is acquired with a lock-in detector. Adapted from [10].

In comparison to the attosecond beamline AS2 shown in Fig. 3.3 used for streaking and LPS, this interferometric NPS setup is much more compact, and it can deliver the same driving field information as from streaking, as shown by Sederberg et al [10], in the right panel of Fig. 3.6. Since no XUV radiation is needed for NPS, the interferometric setup can even be placed in air, which simplifies the building and measurement efforts. Here, the beam is separated into a strong and a weak arm by using the reflection from a wedge which is used for dispersion balancing. The stronger injection beam passes a delay stage, while the other beam is rotated in polarization with two wire grid polarizers, which leads to intensity loss and hence, a weak beam. The beams are then recombined with another wire-grid polarizer and focused with an off-axis parabola into the NPS sample, which is surrounded by two electrodes. They are mounted such that they match the polarization of the weak drive field.

Via trans-impedance amplifiers (TIA) and a lock-in detector the signal is acquired. In order to use lock-in detection the laser pulse needs to be modulated at a reference frequency $f_{ref}$ [85]. In this work, we use $f_{ref} = \frac{f_{rep}}{2} = 2\,\text{kHz}$. The measured signal is then subtracted by the reference at every second pulse. If the two consecutive pulses would be identical, the signal would be erased. Hence, every second pulse has to be changed, e.g. via a chopper that blocks these reference pulses. In that case, the signal is cleaned by the background noise. In order to measure an increased signal, we choose flipping of the CEP after every pulse, because in that case, the modulation results in a doubled signal.

In principle a similar interferometric setup as shown for NPS in Fig. 3.6 can be used for LPS, but it needs to be adapted such that the injection beam has higher photon energies. This can be reached e.g. via frequency upconversion such as harmonic generation or broadening in a fiber.

The goal of this work is pushing the limits of field sampling into measurements of ultrashort deep-ultraviolet (DUV) pulses. Theoretical calculations claim that LPS can measure frequencies up to 1 PHz [9], while it has been experimentally shown that the detection of frequencies above 0.7 PHz is challenging [86]. In chapter 4 measurements with LPS confirm that PHz frequencies cannot be resolved in a typical manner, due to the injection pulse length in this work. Moreover, LPS is compared to attosecond streaking in real-time, to improve the understanding of the different underlying electron dynamics.

In the subsequent chapters the focus is on measuring ultrashort PHz fields with NPS, following the goal of this thesis. NPS has been shown to work down to 275 nm at a single intensity, but as well as the other methods, it has never been used to directly measure the electric field of a DUV pulse $> 1.1\,\text{PHz}$. The development and concept of the generation of strong and ultrashort DUV pulses is covered in chapter 5. Subsequently, direct measurements of these PHz fields with NPS are presented in chapter 6, pushing the bandwidth limits of this technique and enabling a key technology apparatus for the investigation of light-matter interactions on the timescale of electric field oscillations.

# Chapter 4

# Benchmarking LPS vs. Attosecond Streaking

Time-resolved measurements on the attosecond timescale allow studies of electron dynamics on their natural timescale. Understanding and manipulating electron behaviour is essential in fundamental physics research, but also relevant for various fields of applications. Comprehension of the attosecond metrology principles facilitates the implementation of applications, from chemistry [4, 30–33], biology and medicine [87–92] to semiconductor technologies [25, 93, 94] and quantum physics research [95–99]. In order to make this research apparatus available for more applications, a compact, flexible and straightforward measurement technique is needed.

Up to now, attosecond streaking is the power-house for field-resolved metrology on the attosecond timescale. As presented in the previous chapter (3.2.1), it requires large beamlines with complex vacuum setups, expensive optics, and devices for the experimental realization. As a consequence, new methods and upgrades in attosecond metrology are discussed widely in the recent years, such as photoconductive sampling. In order to upgrade attosecond metrology and push the utilization of more flexible metrology setups in the future, linear photoconductive sampling (LPS) is studied in more detail in this chapter.

LPS is based on current sampling and delivers similar results to attosecond streaking, but with better signal-to-noise ratio, faster alignment and acquisition times, and no need of a time-of-flight spectrometer. The method, which is explained in section 3.2.2, has been used for field sampling instead of attosecond streaking in various works [9, 100, 101]. However, when using high harmonics as linear injection pulse, the influence of each harmonic and their temporal distribution was not discovered until now. In the first section of this chapter, measurements of streaking and LPS have been performed simultaneously for the first time, enabling the direct comparison and conclusions about the influence of the broadband harmonic spectrum and hence, the differently modulated photo-electron source.

Developing a versatile metrology technique, requires the ability to measure different electric fields, e.g. with different wavelengths or intensities. In the published works, VIS-NIR fields have been measured, and theoretically, frequencies up to 1 PHz should be resolvable, but have not been confirmed experimentally up to this point. In the second section of this chapter, the spectral limitations for lower wavelengths are studied, pointing out that UV radiation cannot be resolved with this setup. The below presented measurements have been performed at the attosecond beamline AS2 (3.1).

## 4.1 Linear Photoconductive Sampling vs. Attosecond Streaking

In order to push attosecond metrology to be more flexible as attosecond streaking, linear photoconductive sampling is the smallest possible adjustment. It uses the same pump-probe-scheme and experimental beamline, but a different detection scheme. Instead of measuring the electron velocity with a time-of-flight spectrometer, a current is detected with electrodes, simplifying the data acquisition. It has been shown that LPS is capable of measuring the same electric fields in the NIR region as attosecond streaking does [9, 73, 86].

In these previous comparisons, using subsequent measurements, both techniques have been optimized for the highest signal, showing that LPS requires different settings than attosecond streaking. The latter requires isolated attosecond pulses, typically received via amplitude gating of high harmonics, confining only the highest XUV energies via spectral filtering (see section 2.3.2 for details). On the contrary, a higher current signal could be acquired with LPS by not using any spectral filter. The source of the signal was assumed to be the lower order harmonics and thus the lower XUV energies. However, this has not been proven experimentally and remained an unproven statement. The two techniques were never performed simultaneously for direct comparison to the best of our knowledge.

To understand the technique better and advance the technology, the source of the signal has to be determined. In this work, for the first time, LPS and streaking measurements have been performed simultaneously. Using trade-off parameters, both measurement types are not optimized for their strongest signal, respectively, but it enables receiving real-time information about the differences of the techniques. For better understanding of the measured broadband streaking spectrogram, simulations have been performed as well. The results show the influence of the phase properties of the high harmonics on the streaking measurement, enabling to draw conclusions on the predominant XUV energies partaking in the LPS signal generation.

### 4.1.1 Experimental Results

The experimental setup has been used as presented in chapter 3.1. The measurements have been performed in neon, with a gas pressure that is high enough to have a reasonable LPS signal and low enough to still have sufficiently good vacuum for the TOF spectrometer and MCP. No filter has been applied and the XUV corner mirror was coated with gold for sufficient LPS signal. Commonly, photoconductive sampling is performed with two electrodes around the interaction area which measure the current with opposite signs. Therefore, the difference signal yields doubled amplitude. Here, one of the electrodes is aligned with the TOF spectrometer but much closer to the focus, meaning that it would block the electrons to reach the TOF during the measurement. Hence, in these simultaneous measurements presented below, only one LPS electrode could be used. When the XUV beam ionizes the gas, the electrons are detected by a TOF as shown in Fig. 3.2 along one side of the polarization axis (above the gas jet) and an LPS current is measured with a single electrode on the other side (below the gas jet).

The above mentioned experimental adaptions led to broad streaking spectrograms, resulting in the following results, shown in Fig. 4.1.

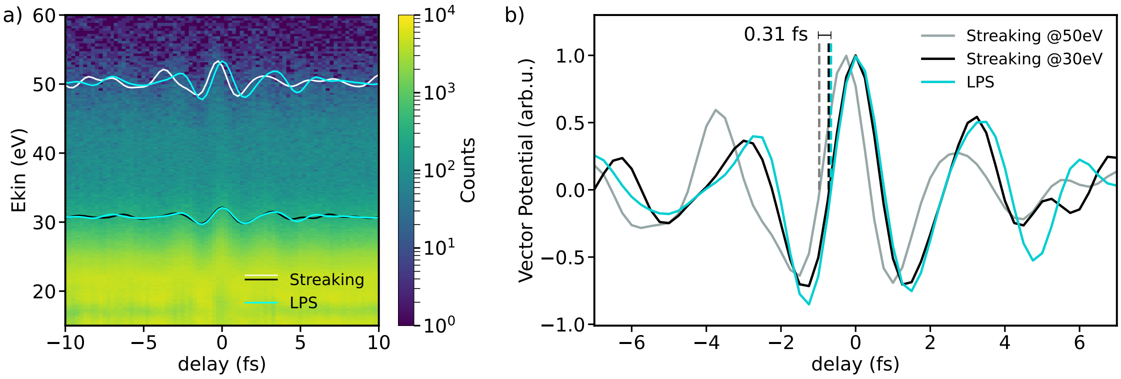

Figure 4.1: In a) a streaking spectrogram with a cutoff trace around 50 eV (white) is shown together with the simulatenously measured LPS signal (cyan). The same LPS trace is plotted with smaller amplitude at lower kinetic energies together with an 'intermediate cutoff' streaking trace around 30 eV (black). The streaking trace at lower energies matches the LPS trace much better than the cutoff one. In b) the three curves are shown in greater detail. A time delay between cutoff and LPS trace of 0.31 fs is derived.

A measured streaking spectrogram with electron counts at many different kinetic energies is shown in a). The cutoff trace around 50 eV is overlaid in white. Moreover, the simultaneously measured LPS trace is laid on top in cyan. It can be clearly seen that a time delay between these two traces exist. On the other hand, when the streaking trace is extracted at lower kinetic energies (black), around 30 eV, the time delay between the pulse maxima is strongly reduced. Also regarding the carrier wave, the streaking trace matches the LPS traces much better at these lower electron energies, highlighted in the right panel (Fig. 4.1 b). The cutoff trace extracted around 50 eV is shifted by approx. 310 as compared to the LPS trace, while the trace around 30 eV is only shifted by ~50 as. In this measurement, step sizes of 250 as have been used.

In addition to the delay, other differences occur in the waveforms. The LPS and 30 eV streaking waveforms overlap quite well in the region of ± 4 fs, but start to differ afterwards. The 50 eV waveform, besides the time delay, already deviates around ± 2.5 fs. A possible reason is the difference in the measured counts at the two kinetic energies (30 and 50 eV), which is approximately two orders of magnitude. The small amount of signal at the cutoff at 50 eV is close to zero and is less reliable due to a small signal to noise ratio. Additionally, the higher harmonics might have slight different temporal distributions, as they are close to the cutoff.

As explained in section 3.2.1, the measured electron momentum is directly coupled to the laser vector potential. Taking the time derivative of this vector potential, results in the electric field. The squared of the field oscillations $(\Re(\tilde{E}(t))^2 = \mathrm{E}^2(\mathrm{t})$ and the intensity envelope $(\mathrm{I}(\mathrm{t}) = |\tilde{E}(t)|^2)$ are shown in Fig. 4.2 for all three traces mentioned above.

The three different traces all yield different values of the full-width at half maximum (FWHM) pulse length. It has to be noted that the signal in photoconductive sampling does not correspond to the vector potential directly, but to the convolution of a gating function with the vector potential (as explained in section 3.2.2). Here, the LPS field is still convolved with the gating function. Since the focus on this section was to observe the differences of the measurement techniques, which seems to be conclusive by looking at the time delay shift, and not the extraction of exact field parameters, the gating function is neglected. However, correcting for the response function typically leads to a shorter FWHM pulse length.

Furthermore, LPS and streaking do measure the same field simultaneously in time, but the traces differ due to the different electron energies. On the one hand, the two streaking traces are extracted at certain kinetic energies, resembling certain high harmonics. On the other hand, the LPS measurement is integrated over all electron energies seen by the electrodes. Hence, the electron energies are not filtered for LPS in contrast to the streaking traces, and moreover, the response is weighted by an unknown function describing the probability of a given photoelectron to reach the electrodes.

As the electrons with lower kinetic energies hold the main amount, and hence give the highest fraction to the LPS pulse integrated over all energies, the measured

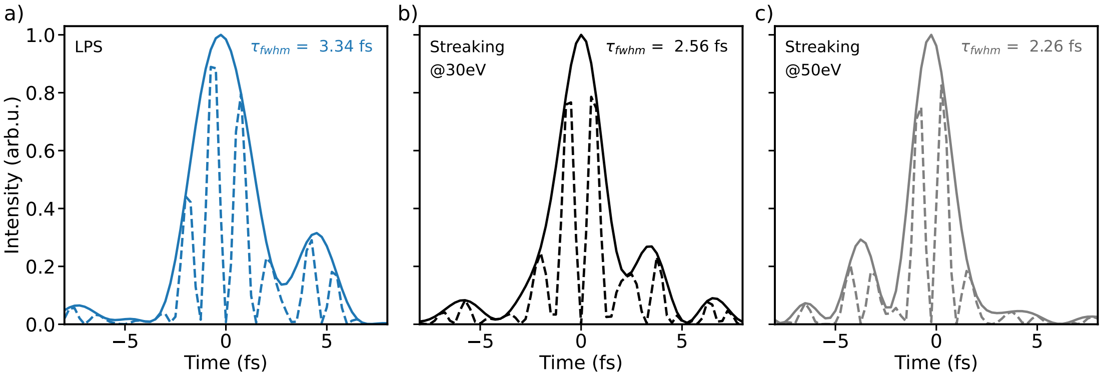

Figure 4.2: The squared signal of the electric field oscillations together with the envelope for three different cases: a) the LPS measurement, b) the extracted streaking trace at 30 eV and c) the extracted streaking trace at the cutoff (around 50 eV. All three traces are measured simultaneously and thus, resemble the same driving field. However, differences occur because the measured LPS traces are integrated over all electron energies which the electrode can detect. Moreover, the two different streaking traces are measured at nearly two orders of magnitude apart regarding their measured counts (see Fig. 4.1), leading to different reliability.

LPS pulse length matches best with the attosecond streaking one extracted at lower kinetic energies (30 eV). Retrieving the electric field from the cutoff trace around 50 eV gives even shorter pulse lengths. Here, the traces are normalized, but as mentioned above and shown in Fig. 4.1, the two streaking traces have different signal strengths, leading to a larger error for the 50 eV trace compared to the 30 eV trace. Moreover, the temporal distribution of the high harmonics becomes apparent in the streaking spectrogram. These differences are reflected also in the electric fields, and are responsible for different FWHM values within streaking.

The curves shown above have been smoothened by temporal and spectral filtering (following 8). To be precise, a super-Gaussian bandpass filter (BPF) has been applied in the frequency domain. The chosen spectral range is visualized together with the Fourier-transformed (FT) streaking and LPS traces in Fig. 4.3 a. The laser spectrum has been measured with a spectrometer (*Ocean Insight*, Maya 2000), which is shown on the right (Fig. 4.3 b) in the wavelength range. The filter has been chosen such that only the existing laser wavelengths between 400 and 1050 nm are present in the FT spectra. Thus, only the frequencies between 0.25 PHz and 0.75 PHz remained. In the raw spectra (Fig. 4.3 a) several artefacts at higher frequencies, especially $> 1$ PHz, can be seen. This high frequency noise is removed by the spectral filtering, leading to smoother curves in the time domain.

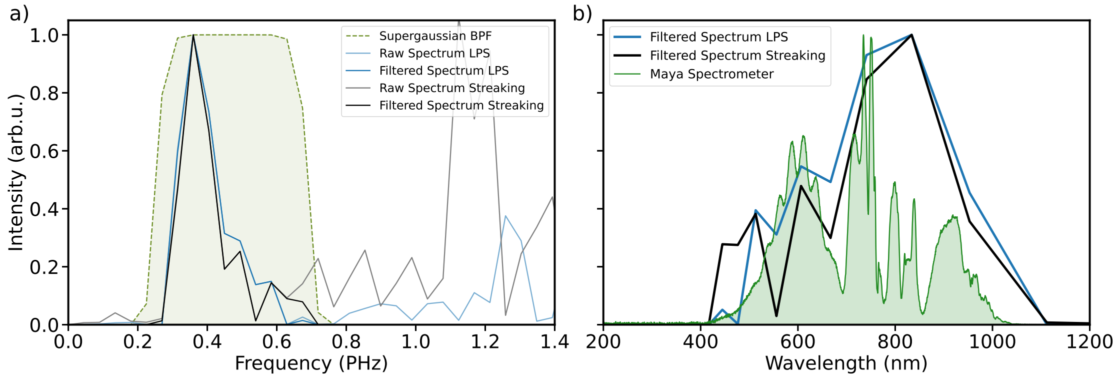

Figure 4.3: Spectral Filtering of the streaking and LPS traces in frequency (a) and wavelength (b) representation. A super-Gaussian bandpass filter (BPF) is applied to transmit only the frequencies actually occuring in the laser radiation. An Ocean Insight 'Maya' spectrometer has been used to determine the correct spectrum and the filter is chosen accordingly. The high frequency artefacts which are visible in the raw spectra (a) are removed.

### 4.1.2 Simulations of HHG and Streaking

In order to understand the origin of the time delay between the high and low kinetic energy traces simulations have been performed. First, the high harmonic generation is simulated by using the open-source framework *HHGmax* [102] and additional custom code by Maximilian Högner. The code simulates the propagation of the fundamental laser pulse through the HHG target (with cylindrically symmetrical geometry and paraxial approximation). Here, the measured electric field with LPS is given as an input pulse. HHGmax computes the single-atom dipole response and the radiation of the dipole is propagated till the end of the target. Second, the macroscopic response is determined by the calculation of the dipole responses on a spatial grid. Third, the XUV field (the high harmonics) is propagated and the far-field is determined in the frequency space. This result, acquired from the HHGmax simulations, is further used to calculate the XUV field in time. Afterwards, the streaking process is simulated via Volkov-integration [103], leading to the following spectrogram. It visualises the kinetic energy of the freed electron after XUV-photoemission for the given time delays. It is shown in Fig. 4.4 (b), together with the experimental result (a) presented above for comparison. The whole simulated streaking trace is shifted in time by about 600 as, such that the maximum of the vector potential is defined as time zero for better visibility.

As highlighted in the experimental results, there is a shift in time visible within the streaking spectrogram. The two streaking traces extracted at 30 eV and the

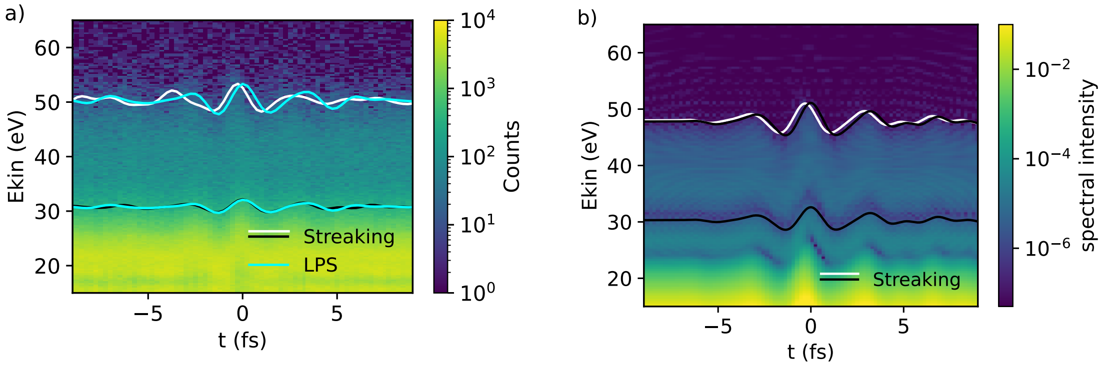

Figure 4.4: Streaking spectrogram experimentally measured (a) and simulated (b) with slightly shifted traces at the cutoff energy compared to lower kinetic energies. In both plots, the shift in delay between the 30 eV and cutoff trace is 310 as.

cutoff (around 50 eV) have a time delay shift of 310 as. The same shift can be determined from the curves in the simulated spectrogram. The black line from the 30 eV trace in Fig. 4.4 (b) is overlaid at the cutoff with the white curve fitted to the cutoff trace. Thus, the shift in time delay is evident not only in the experimental results, but also in the simulated results. The other differences between experimental and simulated spectrogram such as the strength of the spectral intensity or the shift of the cutoff can be explained with the choice of the given experimental parameters. The laser intensity, focal size and pulse properties can differ in reality to the theoretically used values, since they were not measured on a day-to-day basis. However, the actual field parameters, including the phase, are most important for this comparison and used as an input for the simulation.

Here, the phase of the XUV pulse is identified as the prime reason for the time delay shifts. As known, a linear spectral phase corresponds to a shift in time, but the pulse is still unchirped. A second order, nonlinear, spectral phase leads to a chirped pulse, such that the different frequencies occur at different times. To check the phase of the XUV pulse, the results of the HHGmax simulations are visualized. The simulations return the XUV field and the phase in the frequency domain, which is shown in Fig. 4.5 b). The corresponding field intensity is visualised in Fig. 4.5 a).

Fitting the spectral phase visualizes the quadratic slope, proving that the XUV pulse, leading to the spectrogram presented above, is chirped. This chirp can be assigned to the typical attochirp, which occurs due to the process of the high harmonic generation. Since the harmonics are not being emitted simultaneously because of the different electron trajectories (compare section 2.3.2), GDD arises [104].

To further prove that the time shift of the different kinetic energies and thus different high harmonic (HH) frequencies originate from the chirp of the HHs, the

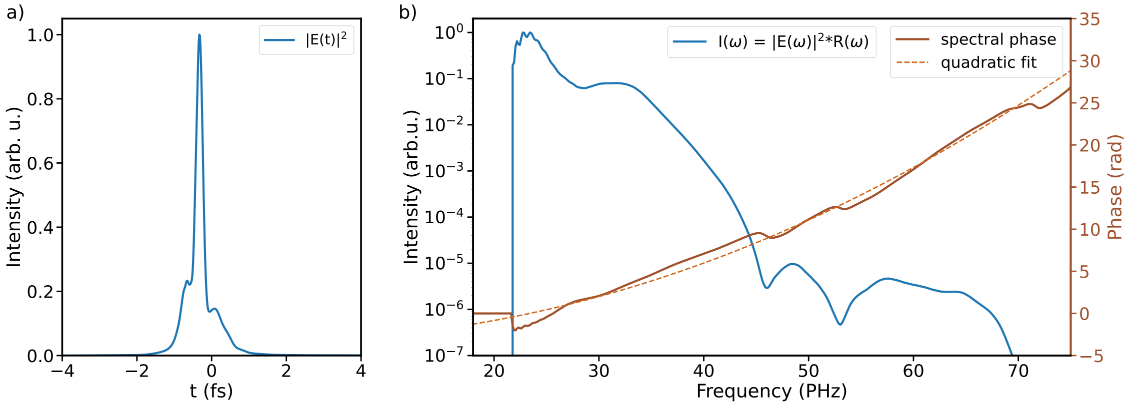

Figure 4.5: Simulated XUV pulse and spectrum with its spectral phase, which has a parabolic behaviour. The spectrum is corrected by an interpolated reflectivity curve of the used gold corner mirror $R(\omega)$ [105].

phase of the simulated XUV field is modified. Using a constant phase, but otherwise the same field as extracted from the HHGmax simulations, the spectrogram is perfectly aligned in time. The comparison is shown in Fig. 4.6.

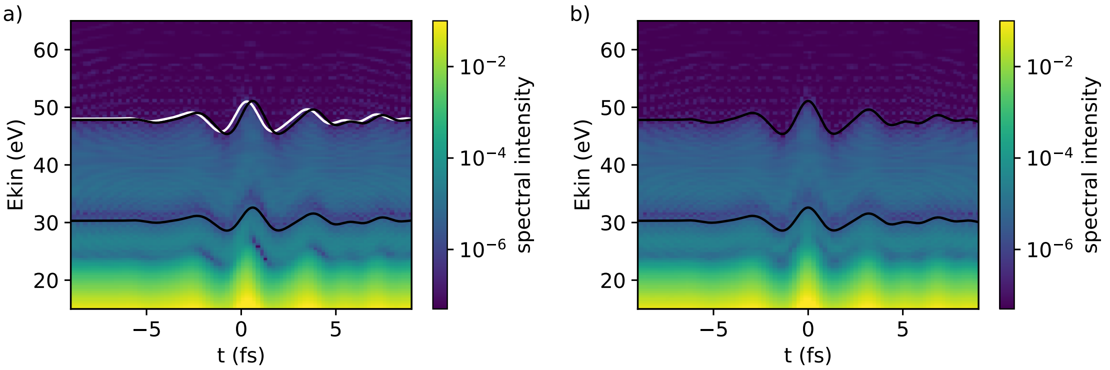

Figure 4.6: The streaking spectrograms calculated with the simulated XUV pulses in comparison: original phase with higher orders (a) vs. linear phase behaviour (b). Using the spectral phase of the derived HHs, leading to shifts in time, versus a modulated, constant phase that does not show any chirp and thus, leads to perfectly aligned traces in time.

In (a), the original phase leads to the determined time delay shifts. First, the shift of the complete streaking trace in time due to a linear spectral phase (which was corrected in Fig. 4.4 for better visualisation as mentioned above). Second, the time delay shift between the different kinetic energies, compared between two traces, due to a nonlinear spectral phase. In contrast to that, in the case of a linear phase in (b), the same trace fits the spectrogram at lower and higher (cutoff) electron energies.

Summarizing, in this chapter it was shown that the simultaneous measurements of LPS and attosecond streaking prove the common assumption that LPS follows the rather lower-energetic XUV photons. This examination was accomplished by comparison of the LPS traces with the streaking traces extracted at different kinetic energies. It was shown via validation with simulations that the different HH frequencies are shifted in time due to a chirped XUV pulse (attochirp). Since the LPS and attosecond streaking measurements were performed simultaneously, real-time comparison shows that the LPS trace has the same time delay shift as the lower electron kinetic energy traces in the streaking spectrogram.

## 4.2 Limits of LPS

As mentioned in the section above, researchers found low LPS signal when introducing metallic filters as common in attosecond streaking. In this PhD work described in section 4.1 it has been experimentally proven that the lower kinetic energies are mostly contributing to the LPS signal. Hence, if they are filtered, the signal is low. Since a spectral filter in attosecond streaking is not just used to cut the spectrum, but also manipulate the temporal behaviour, its absence has a downside. Not utilizing a filter means using the full attosecond pulse train as an injection pulse instead of an isolated attosecond pulse. However, with sufficiently short NIR pulses, the XUV pulse train still leads to sufficient resolution to measure NIR fields with LPS, but reaches its limits for measuring lower wavelengths, which is covered in greater detail in this section.

To study the spectral limits of LPS, the spectrum has been extended via self-phase modulation (SPM) in a gas-filled hollow-core fiber. For this purpose, the setup in the delay chamber of the AS2 beamline (compare 3.2.1) has been modified. The adapted area is indicated with a blue plane in Fig. 4.7 a). The fiber is mounted on an x-, y-, z-stage in the intermediate focus in the delay chamber. To match the focusing parameters, the focusing optics have been exchanged. Moreover, an UV spectrometer to study the broadened spectrum can be reached with a movable mirror.

The introduced fiber has a length of 5.5 cm, a core diameter of 100 $\mu$m and is filled with argon. The gas pressure can be varied up to approximately 1 bar. The fiber setup is designed such that the beam can enter the gas-filled fiber without passing any material. Two tiny holes were drilled into the cladding of the fiber until the core is reached [106]. The fiber is held by an airtight construction which lets gas enter through the holes and exits only through the core endings. These

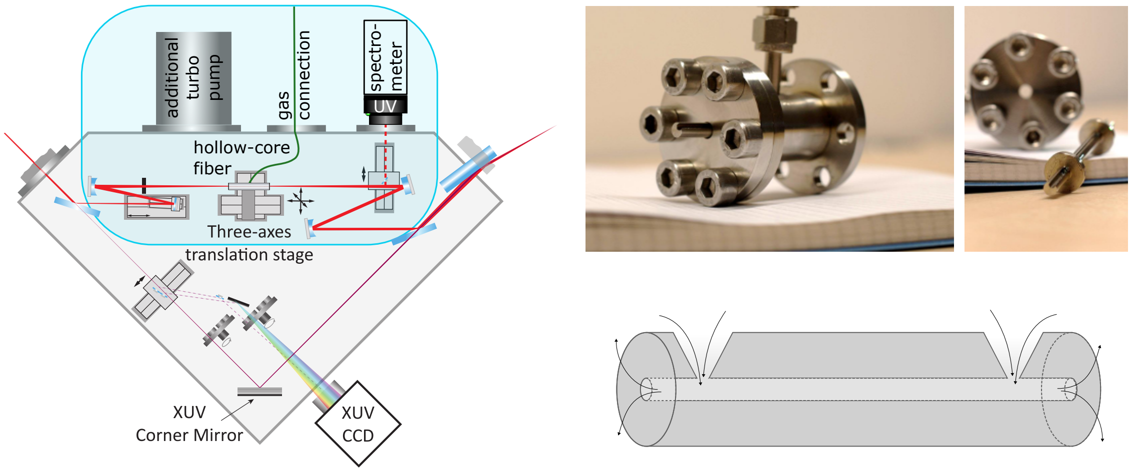

(a) Modifications of the AS2 delay chamber

(b) Inserted hollow core fiber with holes

Figure 4.7: The modified delay chamber of the AS2 beamline (a). The blue area indicates which optics have been changed and which elements have been added. The added hollow-core fiber (b) is a standard glass capillary but with drilled holes to act as gas inlet. A suitable mount induces the gas into the core and is sealed apart from that.

fiber specifics are shown in Fig. 4.7 b). The method enables maintaining the short pulse length until the beam passes the gas. Since the two holes are located close to the two endings of the fiber, the gas pressure in the center can be assumed to be constant. As the gas exits through the core directly into the vacuum, an additional turbo pump is needed for compensation.

The spectrum directly after the added fiber in the delay chamber has been acquired with the VUV mini spectrometer (VS7550) from *Resonance LTD*. Without any inserted gas in the added fiber, it covers the typical range from 400 nm to 1050 nm that is delivered from the FP3 laser system. The ratio of the 600 nm peak to the NIR peak at 900 nm is altered compared to the FP3 output, probably due to slight spatial filtering at the fiber core entrance. When gas is inserted, self-phase modulation takes place and the spectrum is broadened down to ≈ 230 nm. Any changes in higher wavelengths cannot be detected due to the spectral limit of the spectrometer. The spectrum measured at 0 bar and 1 bar argon are presented in Fig. 4.8 in red and blue, respectively.

First, the pulses passing the fiber without any gas are measured with LPS, to recover the optimal measurement settings. The electric field is determined from the measured current (Eq. 3.5) via data processing (Eq. (A.2)). Since the gating function is not known, the here presented fields are still convolved with the gating

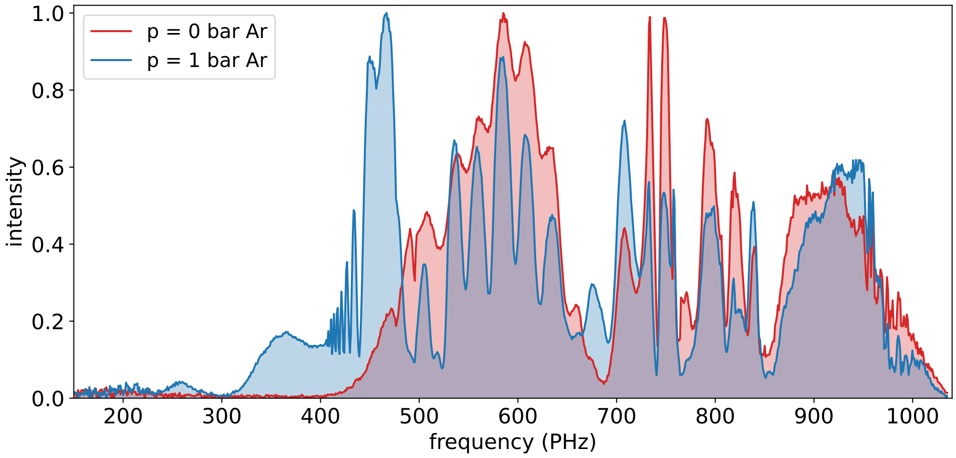

Figure 4.8: Spectra measured in the delay chamber with an UV spectrometer. The beam propagated through a fiber in the intermediate focus, being filled with 0 bar (vacuum) or 1 bar argon. When the fiber is filled with gas, SPM takes place and the spectrum is broadened towards the UV.

function. Temporal and spectral filtering has been performed to reduce the noise level. The spectral filter has been chosen to only transmit the present frequencies, measured with the VUV spectrometer. The measured and derived spectra are compared in Fig. 4.9 a), while the electric field and its intensity envelope, reaching a FWHM pulse duration of 4.12 fs, is shown in Fig. 4.9 b).

In comparison to the previous LPS measurement shown in Fig. 4.1 and 4.2, the measured FWHM of the LPS intensity envelope is now longer by ∼0.8 fs. Differences possibly occur due to the modifications, as presented in Fig. 4.7. Here, the beam passes through a fiber in the intermediate focus, which was not the case beforehand. The focusing optics were adapted to better fit the fiber core, nevertheless, slight spectral filtering occurs when coupling the beam into the fiber. Moreover, even when the fiber is not filled by any gas, the pulse experiences dispersion of the waveguide, according to Eq. 2.28. With a core diameter of 100 $\mu$m, the GVD of the HCF in vacuum for the central mode is approximately -0.4 fs$^2$/mm. For the 5.5 cm long fiber, the pulse experiences around -2.4 fs$^2$, which corresponds to roughly 70 $\mu$m of glass, meaning that a glass wedge would be needed to be shifted by about 1 mm. Hence, the measured FWHM is possibly longer in this configuration due to the spectral filtering and the dispersion of the waveguide.

Already in this measurement of the VIS-NIR pulse, the lower frequencies are not well resolved. The peak in the spectrum from 400 nm to 700 nm as measured by the spectrometer is not seen by the field sampling. It seems like LPS has no response

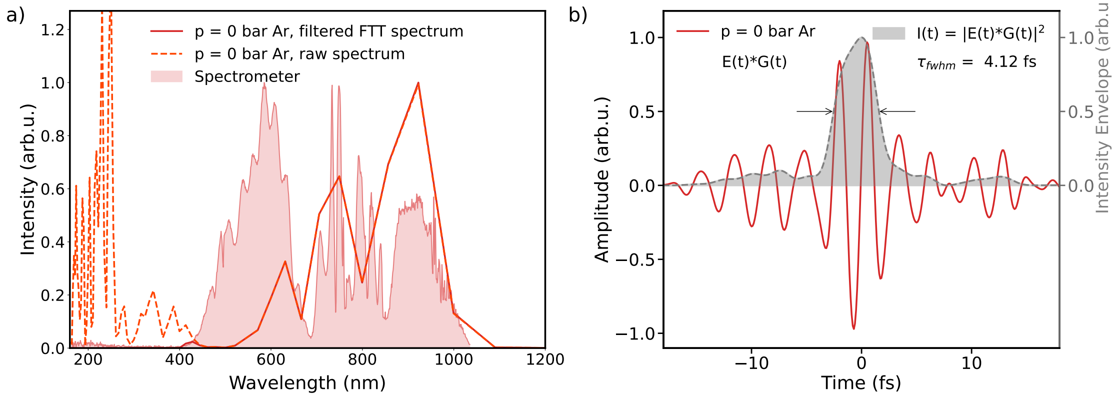

Figure 4.9: LPS measurement of the VIS-NIR pulse from the FP3 output, passing a hollow-core fiber in the intermediate focus, filled with 0 bar (vacuum). In the frequency domain the spectrum is filtered according to the measured spectrum with a spectrometer (a). The filtered corresponding electric field is shown in b), with a full-width half-maximum pulse duration of the intensity envelope of 4.12 fs.

around 500 nm. Next, LPS measurements are performed with gas in the fiber, such that SPM takes place and the spectrum broadens clearly down to 300 nm and with low signal even below down to 230 nm, as shown above. Due to the increased dispersion in the fiber through the inserted gas, the pulse is lengthened and delayed in time. As shown in Fig. 4.10 b), the delay is about 46 fs. This roughly suits the theoretical delay of a pulse travelling through 5.5 cm of 1 bar argon (51 fs) instead of vacuum.

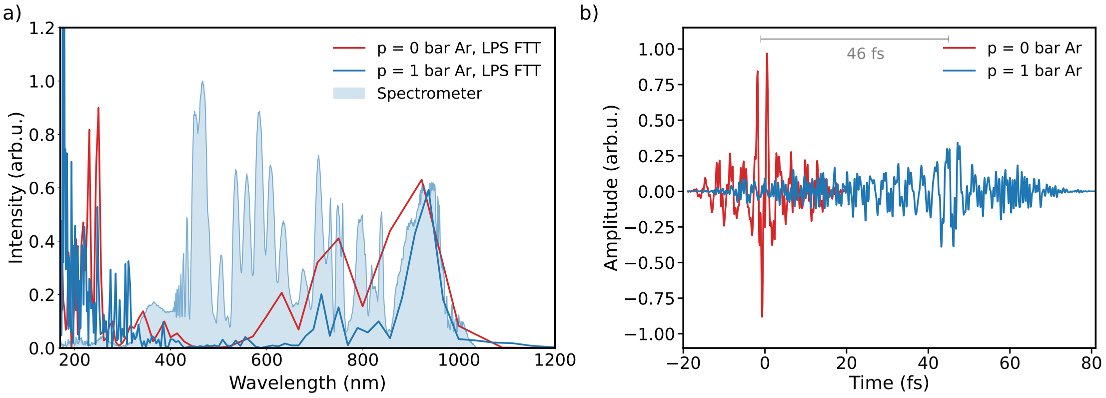

Figure 4.10: LPS of the broadened FP3 pulse, reaching from UV-NIR, as measured with the spectrometer (a). When the hollow-core fiber is filled with 1 bar Ar, the pulse gets delayed in time by about 46 fs and lengthened due to the dispersion of the gas (b). The broadened field signal is weaker compared to the vacuum case (0 bar Ar) and the UV radiation lies below the expected cutoff ($\sim$ 500 nm) and vanishes in the noise.

Since the high frequencies are not filtered here with an analytical spectral filter as for the measurement before, the data is much more noisy. However, again there is low or even zero LPS intensity below 650 nm (0.46 PHz), as visible in Fig. 4.10 a) in comparison with the spectrometer measurement. Again, it seems like a cutoff around 500 nm, which actually corresponds to the duration of the effective photo-electron emission of 1.67 fs with this HH radiation. Further, below 350 nm, the noise superimposes any potential signal. Due to the nature of the transformation from the frequency range to the wavelength range, including a division of $S(2\pi c/\lambda)$ by $\lambda^2$ as explained with Eq. 2.12, the noise increases drastically with shorter wavelengths.

To compare the spectral features without the large noise at low wavelengths due to the transformation, it is presented in the frequency domain below (Fig. 4.11). The spectral filters, i.e. super-Gaussian bandpass filters, have been chosen such that they only cut frequencies beyond the spectrum measured with the spectrometer. Hence, the filter for the broadened spectrum with 1 bar Ar in the fiber has a wider window. Even though the case without gas in the fiber should not have any frequencies above 0.75 PHz, a signal in the raw Fourier transformed data arises in that region. As they appear periodically it can be assumed to be harmonic artefacts. Removing them by spectral filtering leads to the clean electric field of the laser pulse. In the second case, Fig. 4.11 b), the signal is very low from 0.45 PHz onwards but gets steadily higher towards higher frequencies. As it does not match the spectrally measured signal, but does not have an harmonic artefact behaviour either, the reason for this noise is still unclear.

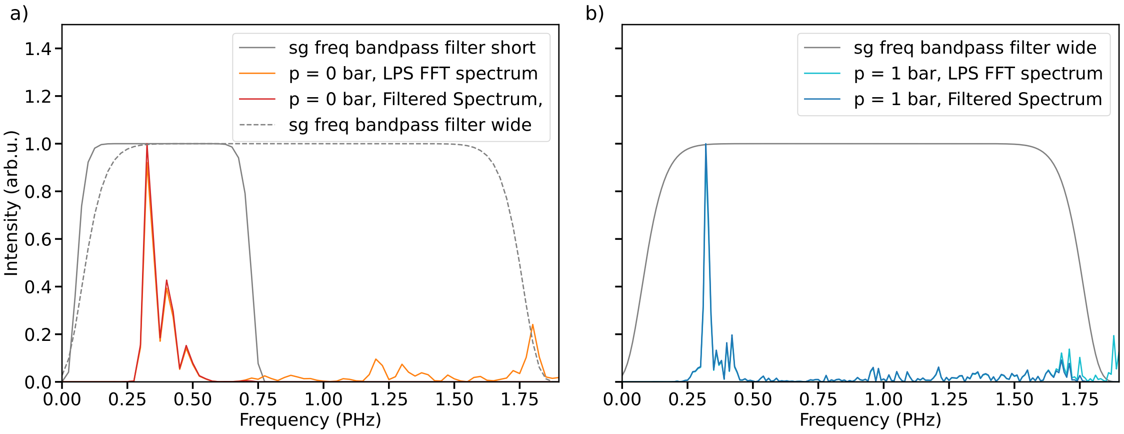

Figure 4.11: LPS Spectra in the frequency domain with spectral filters for both cases: 0 and 1 bar Ar in the fiber, shown in a) and b), respectively. The newly generated frequencies, and generally the lower frequencies between 0.45 PHz and 1 PHz, are not clearly recognizable in the NPS measurement.

Either way, the actual frequencies in place, between 0.45 PHz and 1 PHz are not detected as required, leading to the conclusion that the resolution of the attosecond pulse train is not sufficient to detect these frequencies. This result roughly matches the theoretical cutoff around 0.6 PHz. Moreover, the noise is too large at higher frequencies, meaning that more intense radiation would be needed to be detected, when using a suitable gating pulse.

To achieve the goal of this PhD work and perform field-resolved measurements of ultrashort ultraviolet radiation, an alternative approach was chosen subsequent to these measurements. More intense, ultrashort UV radiation was desired to start detecting and enabling optimizations of the system. Additionally, a metrology technique with better resolution for lower wavelengths was needed. These two challenges are covered in the next two chapters.

# Chapter 5

# Optimizing towards Single-Cycle Deep-UV Pulses

Detecting the electric field of ultrashort laser pulses has always been challenging, as electronic devices are not fast enough. As presented before, attosecond pulses generated via high harmonic generation have been detected traditionally with attosecond streaking. However, in the recent years attosecond metrology has evolved towards a new route, being more compact, flexible, faster and generally more accessible. Especially the current sampling techniques have attracted great interest. For linear photoconductive sampling (LPS), an ultrashort UV pulse is required in order to linearly ionize a medium and act as a gate for sampling another field [9]. As the generation of the typically used XUV pulses is complex and the low response above 1 PHz is limiting as presented in the previous chapter, LPS with high harmonics is not suitable to study DUV fields. In contrast, nonlinear photoconductive sampling (NPS) uses a nonlinear ionization process (strong-field photo-injection) to create an attosecond gate and was benchmarked with attosecond streaking [10]. For NPS, few-fs NIR pulses are sufficient, and the generation of XUV pulses is not needed. It has been validated to operate in the spectral region between 275 nm and 5000 nm, an incredibly broad bandwidth.

The goal of this work is to generate few-cycle pulses in the ultraviolet region, even across the deep-UV towards the vacuum-UV (VUV), and push the field metrology techniques in order to cover this spectral range. With DUV radiation various processes can be studied, as its photon energy matches e.g. the required energy to excite electrons into unoccupied molecular orbitals [3]. For time-resolved studies, ultrashort pulses in the few- or sub-fs range are required in order to resolve the dynamics of electrons on their natural timescale. As the previous field measurements with LPS could not detect the complete spectrum, an NPS setup was built and advanced within the scope of this work. When the electric field is measured in its entirety with all constituent frequencies, the actual electric field might be shorter in FWHM than the previous LPS results. The NPS setup developed for this task is presented in section 5.1. The generation of UV radiation by spectral broadening in a hollow-core fiber (HCF) via self-phase modulation (SPM) was performed as in section 4.2 and is embedded in this NPS setup. The settings were further optimized such that DUV radiation could be generated via SPM, which is presented in section 5.2, together with the field sampling measurements of this radiation carried out with the new NPS setup. It is shown that NPS can resolve the DUV radiation, but the pulse duration of the measured electric field is still too long for various applications.

In order to generate ultrashort UV pulses, the pulses generated via SPM would need to be compressed with broadband dispersive mirrors. As available coating materials reflect UV only in a very narrow wavelength range, pulse compression is challenging for the ultraviolet region. The requirements are not fulfilled by the current chirped mirror technology. Another option would be field synthesis, splitting up the radiation into different channels and compress each individually [39,41]. The recombined ultrashort waveform can then be tuned or synthesized by changing the time delay between the channels. However, to cover the whole spectral region from DUV-NIR, many channels would be needed, which then leads to lower stability. Instead, UV can be generated via different mechanisms, resulting intrinsically in shorter pulse durations. One possibility is the UV generation via frequency upconversion (i.e. third harmonic: THG), delivering sub-3 fs pulses [52]. In 2019, a new record was defined by the generation of DUV pulses between 210 nm and 340 nm, being as short as 1.9 fs [51]. Due to the phase-matching requirements, these low-order harmonics are limited in bandwidth, which leads to a limited minimal pulse duration (according to the time-bandwidth-product resulting from Fourier transformation (Eq. 2.13)). Moreover, THG suffers from poor tunability, is limited in compression for shorter wavelengths and requires constant flow and thus a large amount of noble gases, i.e. often the rare and expensive neon gas.

In contrast, a promising approach is the generation of self-compressed solitons and DUV resonant dispersive wave (RDW) emission. In the last decade, research in nonlinear fiber optics has opened up new frontiers in soliton dynamics, offering a robust and unique method for generating few-cycle UV pulses with exceptional peak and average power [5,54,55]. Emission of RDWs in gas-filled hollow-core fibers (HCFs) has facilitated the generation of pulses with comparable durations [53,57] and tunable wavelengths ranging from the visible to the vacuum UV. Additionally, these methods offer over ten times higher energies, even with compact HCF systems [56]. In the last section of this chapter, section 5.3, the requirements to generate RDW emission with the existing laser setup are presented. The desired settings are derived from simulations and an experimental setup was developed accordingly, which is presented as well.

## 5.1 Experimental Development of Broadband NPS Setup

In order to perform field sampling of ultraviolet radiation for the first time, a new experimental setup had to be developed. It was built inside a vacuum chamber, to maintain short pulse durations as the pulses would get dispersed in air. Moreover, the deeper the ultraviolet wavelengths, the more absorption in air occurs, reducing the field amplitude before it reaches the NPS sample. The used vacuum chamber contains a breadboard that is decoupled from the chamber walls, as necessary to decouple it from the flange-mounted, vibrating turbo pump which would disturb any field sampling measurement.

The laser pulses from the FP3 setup (see details in section 3.1) are guided with a periscope through a thin fused silica window into the vacuum chamber, which is evacuated by a turbo pump. In this work, an NPS setup according to the method presented in section 3.2.2, Fig. 3.6, was built and further developed, enabling field sampling measurements of radiation reaching from the NIR down to the VUV for the very first time. In this NPS technique, the high intensity of the injection pulse confines the multi-photon ionization to a duration of hundreds of attoseconds. The resulting temporal gate allows field sampling of the drive pulse with a comparable resolution. This self-built, bandwidth-extended NPS setup is presented in Fig. 5.1 .

The incoming VIS-NIR field (red) is split into two arms by a mirror that has a hole in its center, known as a perforated mirror. The part of the beam that has a larger diameter than the hole is reflected and has a doughnut shape from then on, while the central part passes through. The size of the hole is chosen accordingly to the beam diameter to split the arms for the desired powers. In each of the arms, glass ($SiO_2$) wedges are mounted for dispersion balancing and CEP optimization. In this setup, the reflected beam is the stronger one and will be used as injection pulse for NPS. It traverses a delay stage and is rotated in polarization by 90° by reflecting of a wire-grid polarizer and silicon (Si) wafer at Brewster's angle ($\sim 74$ degree).

The other beam that passed through the hole is focused into a gas-filled hollow-core fiber, as in chapter 4.2. It has a fiber length of 5.5 cm and core diameter of $100\,\mu$m. It is filled with tunable argon pressure, up to 1 bar. As the gas constantly exits the fiber and is directly sent into the vacuum, higher pressures are not realisable without harming the turbo pump. The spectral broadening in the fiber takes place according to the results presented in the previous chapter, where details on the fiber construction can be found (Fig. 4.7). Now, the electric field of this broadened pulse (purple) including its phase information will be measured via NPS. Hence, this broadened and weaker pulse acts as the drive pulse.

The fiber output is collimated and reflected with Al mirrors that have a thin protection coating of magnesium fluoride ($MgF_2$) to prevent oxidisation, because

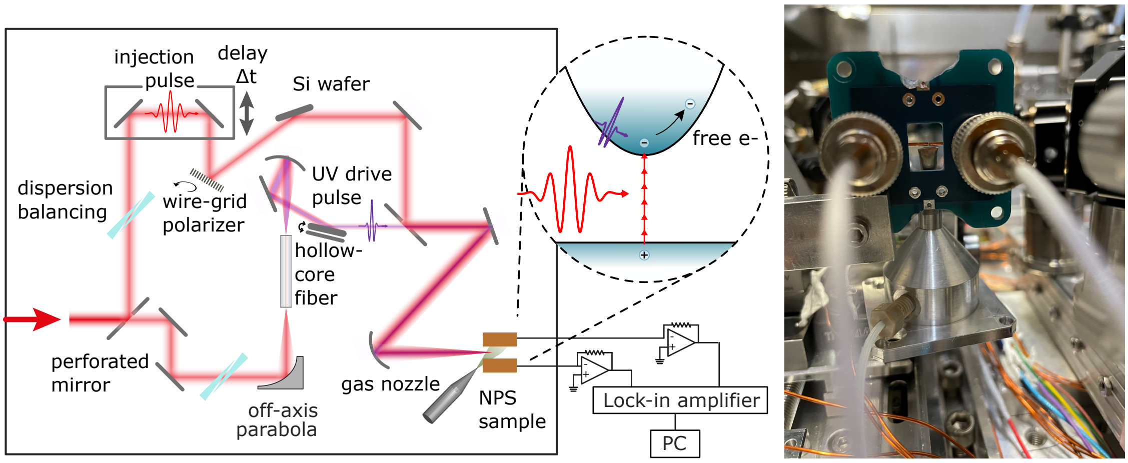

(a) schematic NPS setup (b) NPS sample

Figure 5.1: Self-built NPS setup: a) a perforated mirror separates the beam into two arms. The reflected beam acts as injection arm and is therefore orthogonally polarized to the drive beam after passing a wire-grid polarizer and Si wafer. The other beam is focused into a gas-filled hollow-core fiber that generates UV radiation. The UV can be filtered by reflection of a Si wafer under IR Brewster angle. The two beams are recombined with another perforated mirror and focused onto the NPS gas sample, shown in the picture besides (b). The signal is amplified and acquired via lock-in detection

aluminum has higher reflectivity of the UV wavelengths than aluminum oxide. After collimation, the beam is either fully reflected via these mirrors, or filtered by reflecting of a Si wafer under IR Brewster angle. The latter suppresses the IR radiation and enables a unique examination of the generated UV radiation. Afterwards, the orthogonally polarized injection and drive pulses are combined using another rectangular perforated mirror, and focused collinearly onto the NPS sample, which consists of two electrodes, and a gas nozzle as shown in Fig. 5.1 b). The focus of the injection beam (NIR) and of the drive beam (UV-NIR, referred to as UV) are shown in Fig. 5.2 a) and b), respectively. The injection focus is smaller than the drive in order to measure the homogeneous field in the center of the drive. Moreover, the injection does not show a clean Gaussian shape due to the previously mentioned doughnut-shape.

For a large bandwidth and flexible signal tunability, gas is used as medium. Two electrodes, which are simply two copper wires, are mounted around the gas nozzle. Since the UV driving pulses have p-polarization, the electrodes are aligned accordingly, left and right of the gas jet. This detection setup is pictured in Fig.

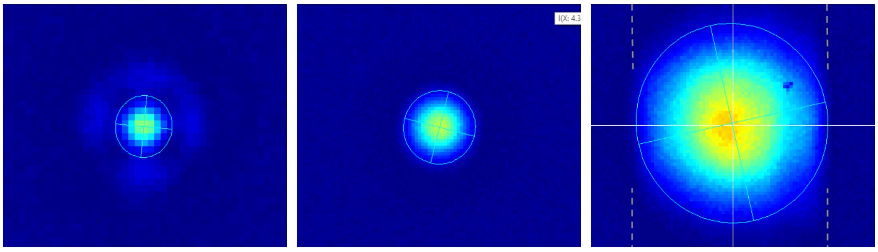

(a) IR focus: $\sim 50\mu$m ⌀ (b) UV focus: $\sim 120\mu$m ⌀ (c) Imaged UV focus with electrodes

Figure 5.2: Beam shape and diameter of the both arms in the NPS focus. a) The injection beam has a smaller focus than the drive beam (b), due to the larger beam diameter before the focusing mirror. The size difference enables an NPS measurement of the center of the drive pulse (b) which is more homogeneous than on the edges. c) The focus is imaged outside of the chamber, to align the beam between the NPS electrodes and perfectly overlapping with the other beam, while the chamber is under vacuum.

5.1 b). The electrodes measure the induced current as a function of time delay between the injection and drive pulses, as explained and visualized in Fig 3.4, section 3.2.2. Each of the electrodes is connected to a transimpedance amplifier (TIA, here FEMTO DLPCA-200) that amplifies the current between the electrode and the ground with a gain of $10^9$ V/A. Further, this voltage signal is detected via a lock-in amplifier (Zurich Instruments MFLI). As explained in section 3.2.2, in order to use lock-in detection the laser pulse needs to be modulated at a reference frequency [85]. Here, the CEP was flipped for every consecutive pulse between 0 and $\pi$, and the used reference frequency is 2 kHz.

For diagnostic purposes, three movable mirrors are placed in the chamber to pick up the beam at different positions. The first can sent the collimated fiber output out of the vacuum chamber through a $MgF_2$ window, onto a powermeter. This option is used to align the fiber around the beam on a proper mode and output power. Moreover, after the perforated mirror is a translation stage which enables capturing and redirecting the beam into the UV spectrometer (VS7550 VUV Mini Spectrometer from *Resonance Ltd*). In addition, after the NPS sample, the beam is re-focused outside to another spectrometer and camera to find and optimize the temporal and spatial overlap of the two arms. As an example, the focus of the drive arm is shown in Fig. 5.2 c), which is used to align the beam centered between the electrodes and with the other arm.

## 5.2 Limits of Ultrashort UV Pulse Generation via SPM

The fiber construction presented in Fig. 4.7 in the preceding chapter is used in this section. The gas enters into the fiber core through two small holes drilled into the cladding and leave via the core entrance and exit, directly into the vacuum. As a consequence, the pressure in the central part of the fiber is assumed to be constant and no windows are required to seal the fiber. As the gas is continuously exiting the fiber, the gas load in the vacuum chamber is increased. A maximum backing pressure of 1 bar can be used during operation of the turbo pump. With further optimization, this fiber setup could provide an extended spectrum covering the whole DUV region via SPM in a gas-filled hollow-core fiber (HCF), which is shown in Fig. 5.3 (purple), in comparison to the spectrum measured without gas in the HCF (red).

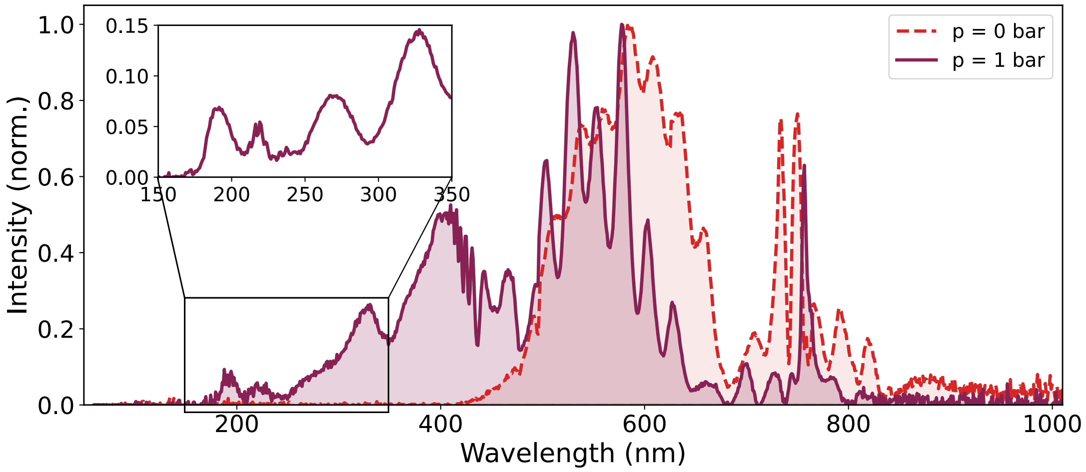

Figure 5.3: Spectral Broadening via SPM in a 5.5 cm long HCF. The fiber is either unfilled (0 bar, red dashed line), or filled with 1 bar Ar (purple solid line). The spectrum can be extended down to $\sim$ 170 nm, as highlighted in the inset. The spectra are recorded with the VUV mini spectrometer VS7550.

Initially the spectrum spans from approx. 400 nm to 1050 nm (see previous chapter), whereby the radiation above 820 nm can be barely detected by the used small slit size of the UV Spectrometer (VUV mini spectrometer (VS7550) from *Resonance LTD*). When entering 1 bar argon, the spectrum is expanded, reaching down to about 170 nm, as highlighted in the inset. Depending on the alignment of the fiber, and the input energy, the spectrum can be tuned. In the following, NPS measurements are performed with the NPS setup presented in the preceding section 5.1. The electric field is derived from the measured NPS signal as explained in the appendix A.2.

First, NPS measurements are performed and optimized for the drive pulse entering through the hollow-core fiber in vacuum, without any gas filling. The resulting electric field is presented in Fig. 5.4 a), together with its intensity envelope. The derived FWHM pulse duration of the envelope is 2.99 fs. The corresponding spectrum, determined via Fourier transformation, is shown in b) depending on wavelength. It is compared with the spectrum measured with the UV spectrometer as above (dashed), and an Ocean Optics Maya spectrometer (filled area). The Maya spectrometer is more suitable for this spectrum, as it well resolves higher wavelengths and therefore better matches the NPS spectrum.

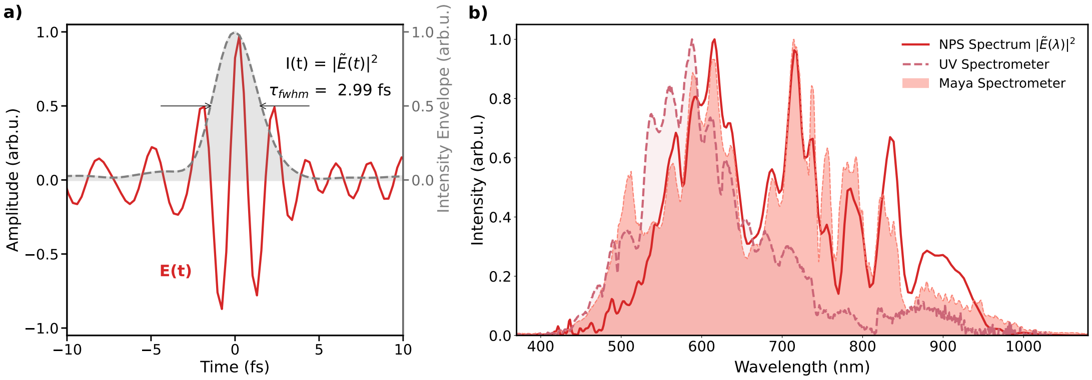

Figure 5.4: a) the electric field of the VIS-NIR drive pulse propagating through a hollow-core fiber in vacuum, without any gas filling. The intensity envelope measures a FWHM pulse duration of 2.99 fs. The corresponding spectrum (b) matches with the spectrum acquired with the Maya spectrometer. The UV spectrometer has low response in the higher wavelengths.

Next, 1 bar Ar was sent into the fiber. For better current signal, the spectrum was tuned for highest UV intensity, and not largest bandwidth, due to the expected low spectral response in the UV. As the pulse propagates through the gas, it experiences the dispersion and is delayed accordingly. Moreover, it is spectrally broadened due to SPM. The measured electric field is plotted in Fig. 5.5 a). The pulse is evidently dispersed and now has an envelope pulse duration of 7.39 fs FWHM. The higher frequencies are occuring clearly on the trailing edge, as typical for SPM (see chapter 2.2.2 for further details), introducing a positive chirp.

In Fig.5.5 b) the measured NPS spectrum is compared with the one acquired by the UV spectrometer. The spectrum is optimized for the peak at 300 nm, which is

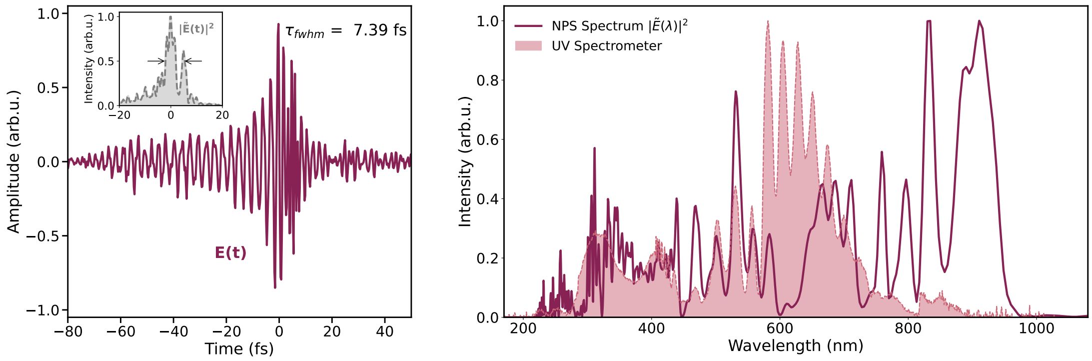

Figure 5.5: a) the electric field of the drive pulse after propagating through a gas-filled HCF. The interaction of the pulse with argon at 1 bar is clearly visible, resulting in a positively chirped pulse due to SPM. The corresponding spectrum is shown in b). The spectral broadening was tuned to have a higher intensity around 300 nm, as determinable from the spectrometer acquisition, as well as the Fourier transformed NPS field.

also resolved in the NPS spectrum. Generally, the spectra match well below 600 nm, but are completely divergent at higher wavelengths. These differences can occur due to several reasons. As the spectrometer is optimized to detect UV, the NIR detection capabilities above 800 nm are generally low. Moreover, differences might occur due to the spatial selection of the spectrometer with a 50 $\mu$m slit. If slight spatial chirp occurs or the beam contains higher-order modes, the different frequencies vary at different positions and focus differently, which again influences the NPS signal. In addition, a spectral dip occurs at 600 nm, which suggests an imperfect matching spectral response. It is calculated for the optimal injection CEP, but in reality the CEP might differ slightly.

Summarizing, in contrast to LPS, NPS can certainly detect the wavelengths down to 230 nm, as shown in Fig. 5.5. Depending on the injection pulse and experimental parameters, there are dips in the response, however, further tests and spectral tuning with this setup did not lead to shorter pulse lengths. Due to the SPM, the pulse is extensively dispersed and would need compression, which is not possible with the current chirped mirror technology. Also collaborations with optics design researchers could not provide suitable mirror coatings. Unfortunately, at this point, the UV radiation cannot be generated first and compressed later. Instead, a generation method is needed that directly generates an ultrashort pulse.

In the recent years, soliton self-compression and RDW emission attracted great interest. It was shown that DUV pulses can be emitted from self-compressed soliton in HCFs, with efficient energy conversion and high tunability. Moreover, the most important aspect, these pulses are intrinsically ultrashort while being generated. As no field sampling technique existed to measure the pulse duration of DUV pulses in a field-resolved manner, the goal of this work is to apply these attractive method of soliton dynamics to our laser system and measure the electric field with an extended NPS technology, for the first time. Therefore, the DUV generation via RDW emission is covered in the following section.

## 5.3 DUV Generation via RDW Emission in HCFs

Soliton self-compression and the resulting emission of a resonant dispersive wave (RDW) were extensively studied in the last decade also for hollow-core fiber (HCF) systems. Previously, the concept was occuring in fine-structured capillaries, such as photonic crystal fibers (PCFs), but were not observed in simple gas-filled hollow capillaries, as special requirements need to be fulfilled [55]. In order to generate a self-compressed soliton and RDW emission in HCFs, the dispersion needs to be negative, balancing the SPM. The physical concept is explained in detail in chapter 2.

In order to identify the feasibility with our system and goals, and implement the RDW generation in our laboratory, a collaboration with Francesco Tani has been started. He contributed to this project with his theoretical knowledge and numerical simulations (using the code [107]), determining the suitable parameters for our given laser setup and comparing the experimental results with theory. The calculations revealed that we can theoretically generate the shortest UV pulses ever reported using the spectrum from the FP3 laser system with about 3 fs pulses centered around 750 nm. Using our broadband spectrum as fiber input can lead to DUV resonant dispersive waves around 200 nm with pulse energies around 0.1 $\mu$J. In the previous experiments, a fiber with 100 $\mu$m core diameter was used. Due to the possibility of experimental confirmation, simulations have been performed to match this core diameter. In summary, the following parameters are needed:

- 100 $\mu$m core diameter
- 8 cm fiber length
- 10 bar helium
- 15 $\mu$J pulse energy, corresponding to 62 mW with our 4 kHz system

Using these parameters leads to the following simulated evolution of a self-compressed soliton and RDW (see Fig. 5.6). In the left panel, the temporal evolution of the electric field along the fiber length (from bottom to top) is shown. In the right panel, the evolution of the frequency distribution along the fiber length is plotted.

Already along the first centimeters, the spectrum is broadened via SPM. The zero dispersion wavelength (ZDW) is indicated as white dashed line and proceeds around 500 nm. It shifts due to the pressure gradient towards the end. As the negative dispersion acts on the major part of the spectrum, it can balance the SPM and leads to a self-compressed soliton. The reduced pulse duration is visible in the time representation on the left, showing a reduced width of the yellow central peak. In this configuration the phase-matching results in the energy transfer to a RDW around 200 nm, after propagation through approximately 8 cm. The longer it propagates, the more energy is transferred into the RDW, resulting in an intense DUV pulse at the fiber exit at 12 cm. If the fiber would be significantly longer, the RDW pulse would be stretched since it experiences positive dispersion over a longer distance. The choice of fiber length is a trade-off between RDW intensity and pulse length. The tilted stripes in the soliton indicate the CEP alternation of the field along the fiber, due to the dispersion, which is significantly different for the RDW, showing less tilt.

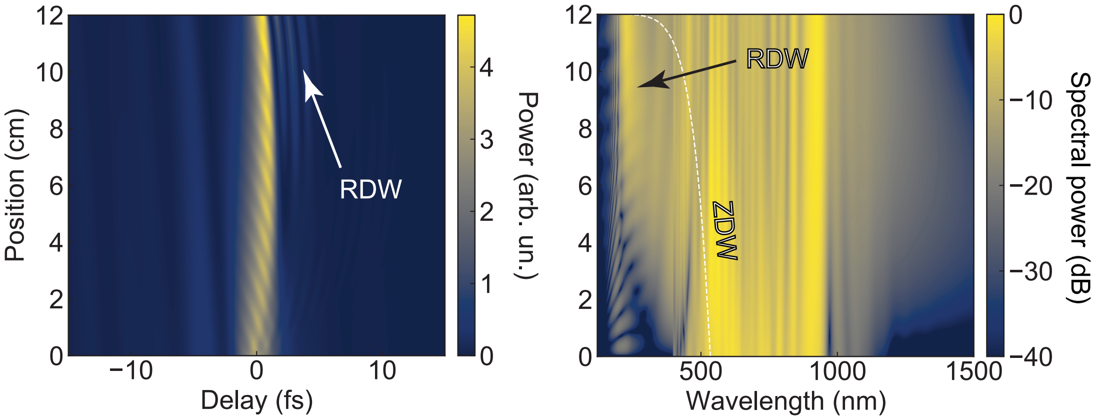

Figure 5.6: Simulations of the evolution of a self-compressed soliton and resonant dispersive wave in a hollow-core fiber with the above presented parameters. In a) the temporal dynamics along the 12 cm fiber highlights the compression of the pulse and RDW emission, while b) shows the evolution of the spectrum in the wavelength range.

In order to make these simulations reality in the experiment, a setup possessing the above mentioned requirements is needed. In the previous setup, the gas was continuously exiting directly via both fiber core endings into the vacuum chamber. Due to the short pulse durations and UV wavelengths, transmission through windows would significantly lengthen the ultrashort pulses. However, this previous configuration can only hold pressures up to 1 bar of gas. To generate RDW emission in the DUV region, 10 bar He are required, and hence, a new fiber configuration has to be developed.

According to the simulations, the required fiber has a length of 8-12 cm and a core diameter of 100 $\mu$m. It is filled with tunable pressure at the entrance and has a pressure gradient along the fiber to deliver the pulses directly into vacuum. As the input pulse does not contain UV, it is compressible with chirped mirrors. By overcompensating the dispersion beforehand, the propagation through an input window can be accounted for. Then, DUV light is generated in the fiber and at the exit, windows cannot be used in order to maintain the short pulse duration. As a result, a fiber construction was designed that seals the high gas pressure at the input and hold a pressure gradient through the fiber core. It was previously shown that a pressure gradient is not harmful for the RDW emission and can even be beneficial [65]. In our vacuum chamber, the exit has to be equipped with a differential pumping unit, evacuating the gas directly from the fiber exit such that the vacuum chamber can operate at least under low vacuum. The newly designed setup is presented in Fig. 5.7. The technical drawing, issued by the technician Tobias Kleinhenz, is shown in a cross-sectional view in a), while a picture of the developed mount is shown in b).

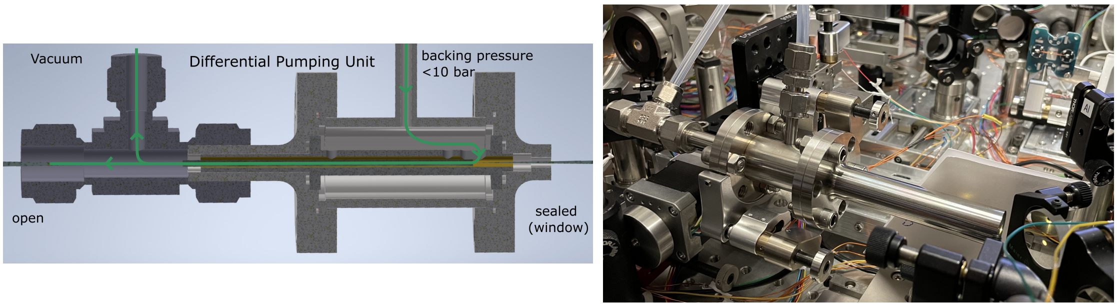

(a) Fiber Cross Section View

(b) Final Setup

Figure 5.7: Fiber Setup for RDW Generation: a) shows the technical drawing in a cross section view. The gas flow is visualized via green arrows. The gas entrance is sealed via the mount and a glass window, and can only pass through the core itself, where the gas is evacuated at the exit, resulting in a pressure gradient along the fiber. The beam and residual gas exits at the left into the vacuum chamber. In b) a picture of the final construction is shown. The entrance window is mounted sufficiently far away from the core entrance to avoid damage through the focused laser.

The fiber is glued into the fiber mount and the construction is sealed via o-rings and an entrance window. To avoid damage, the window is mounted sufficiently far away from the focus and to withstand the high pressure, the window is glued from the inside. In the cross section view (a) it is shown that the gas enters the core through the front entrance on the right and can only exit through the end, where it is directly exhausted from a vacuum pump (upwards). The beam and residual gas exits through a Swagelok T-piece at the left end. In the picture shown in (b), the construction is shown mounted inside the vacuum chamber. The gas is connected via Swagelok connections and gas tubes, as well as the vacuum pump at the exit. The fiber construction is held by a tiltable mirror mount, which is mounted on an x-, y-, z-translation stage. The beam is focused into the fiber with a parabolic mirror. As the fiber is now longer and different lengths had to be tested, the mount construction was built by the technical workshop in several lengths.

In order to fit the new parameters, the surrounding NPS setup was readjusted and optical elements were relocated due to the tight space. First soliton simulations were performed with a Gaussian input spectrum, leading to RDW emission after 8 cm. The first experiments were therefore performed with a fiber being 8 cm long. The settings were scanned and optimized, but no UV light was detected. Therefore, a 10 cm long fiber and subsequently a 12 cm long fiber was tested. With the 10 cm fiber, UV radiation occured, but was still quite weak. After 12 cm, DUV light was clearly detected with the UV spectrometer. More detailed simulations performed later with the measured input field also suggested a 12 cm long fiber (as in Fig. 5.6). Moreover, higher-order modes were not accounted for in the previous simulations which may occur experimentally. If the beam contains higher-order modes, longer propagation distances are needed, as the mode is naturally cleaned in the very beginning and soliton self-compression takes place later. The measured spectra show DUV peaks following RDW behaviour using the 12 cm fiber. According to the phase matching rules, the RDW shifts to higher wavelengths with higher pressures. This phenomenon was detected and is presented in Fig. 5.8 a). As the intensity was kept constant, the conversion efficiency decreases with lowering pressure.

The pressure at the fiber entrance was tuned from 6 up to 10 bar He. At 6 bar He, the RDW is located around 200 nm. At the maximum pressure allowed by the setup, 10 bar, the RDW peaks around 235 nm. The simulations of the pressure scan are presented in Fig. 5.8 b) for comparison. The pressure-dependent behaviour of the RDW in experiment and simulations agree well. Unfortunately, the DUV spectrometer could not detect the NIR radiation here. Typically, spectrometers that can measure the DUV cannot resolve IR radiation. In order to detect the whole spectrum, spectra from different spectrometer would need to be stitched together.

If the field sampling technique NPS covers the whole range, it could deliver the complete spectrum all in one. Moreover, simulations of RDW emission present the generation of ultrashort pulses. Hence, the agreement of the spectral behaviour in the DUV range indicates the generation of ultrashort pulses also experimentally. In order to measure the electric field, the NPS setup was adjusted around the new fiber construction. The results of conducted NPS measurements are presented in the following chapter.

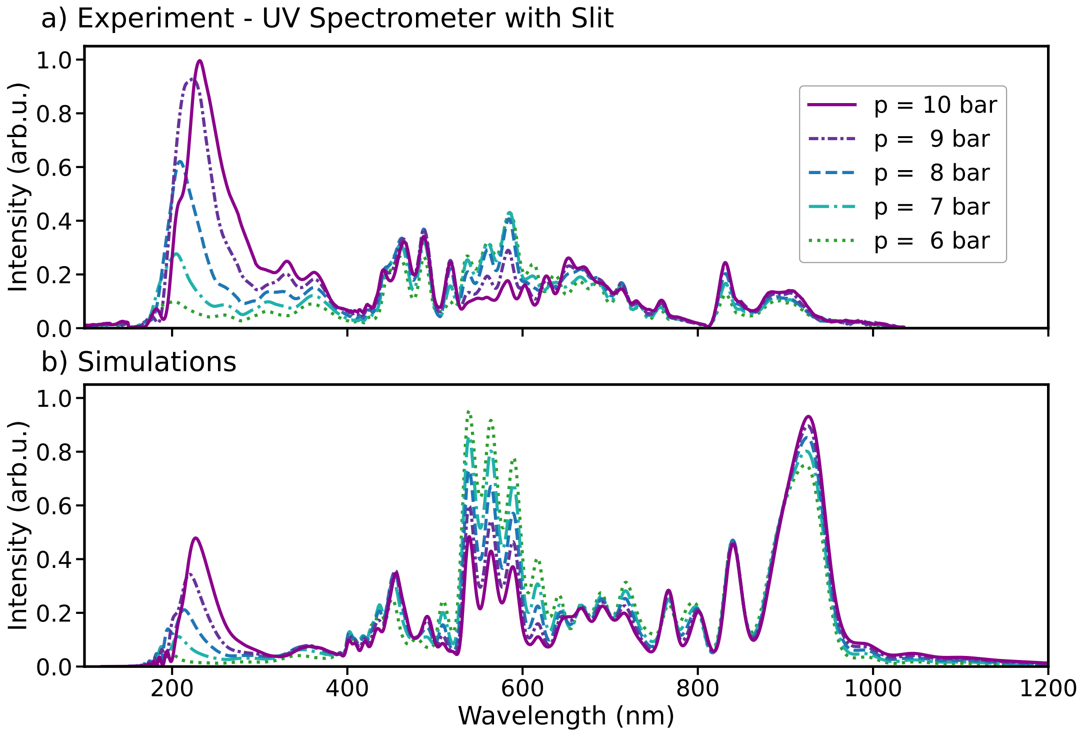

Figure 5.8: Experimentally measured spectra of the soliton and RDW radiation with the VS7550 UV spectrometer in a) and setup-specific simulations performed by Francesco Tani in b). Both panels show the RDW behaviour in the DUV for different HCF entrance pressures, reaching from 6 to 10 bar He. The spectrometer has low sensitivity above 750 nm.

# Chapter 6

# Field Sampling of Attosecond Solitons and Deep-UV Pulses

In this chapter, the previously presented generation of DUV radiation via soliton dynamics in HCFs is combined with the recent advancements in attosecond metrology. Self-compressed solitons and consequently emitted resonant dispersive waves (RDW) are measured in a field-resolved manner for the very first time. In order to do so, an experimental setup was developed and was presented in the previous section 5.3, where the successful generation of RDWs in the DUV is shown. Now, the full electric field information including the phase is obtained via nonlinear photoconductive sampling (NPS). Therefore, the developed fiber construction is inserted into the NPS setup presented in 5.1. In the NPS technique, electrons are rapidly released in argon via high-order multiphoton ionization by the few-cycle VIS-NIR pulse, the *injection* pulse. The orthogonally polarized *drive* field then accelerates the charges, producing an optically-driven current proportional to the drive pulse's vector potential.

The metrology technique NPS now captures the electric field of the generated RDW, demonstrating its capability to detect pulses at remarkably short wavelengths, and thus, extending the bandwidth of this technique further into the DUV, up to 8 eV ($\sim$ 150 nm), presented in section 6.1. When isolating the RDW, the DUV wavelengths could be finely resolved, exhibiting an envelope pulse duration of 1.2 fs, which is, to the best of our knowledge, the shortest pulse ever reported in the UV region. Moreover, sub-cycle DUV-NIR pulses, arising from the soliton dynamics in the HCF, are presented in section 6.2. By tuning the carrier-envelope offset phase (CEP) of the input pulses, the waveform can be optimized. For the first time ever, a sub-cycle light transient generated via soliton-self compression containing optical wavelengths were measured, being as short 323 as ($E^2$). Via comparisons with simulations and pressure scans the soliton behaviour is studied in section 6.3. Finally, as a proof of concept, the soliton pulses are used as NPS injection, acting as an attosecond gate to measure NIR pulses. With these measurements, presented in section 6.4, the applicability of these pulses to study extreme nonlinear optics is shown. Hence, light-matter interactions in the previously inaccessible spectral range between 4 eV and 8 eV can now be investigated on attosecond timescales. This chapter closely follows the author's publication [108].

For all sections, it has to be noted that the measured delay-dependent signal, the electric current $I_{drive}$, maps the vector potential of the drive pulse convolved with a gating function G(t). In the frequency domain, the data is corrected by the corresponding response function, numerically calculated by Manoram Agarwal. In addition, the data is processed with spectral and temporal filtering, as explained in the appendix 8. The electric field is derived from the vector potential via $E(\omega) = -\frac{\partial A(\omega)}{\partial t} = i\omega \cdot A(\omega)$.

## 6.1 Expanding NPS Bandwidth via DUV Dispersive Waves

In this section, NPS measurements of DUV radiation are performed. To generate a resonant dispersive wave in the DUV region, as in the previous chapter, the input of the fiber is filled with 10 bar of helium. With this setting, the soliton order N $\sim$ 1.9 is obtained and the RDW phase-matching is set around 240 nm. As explained above, the fiber output lies in vacuum, allowing propagation of the waveforms without significant temporal stretching induced by dispersion until reaching the argon target. In order to suppress the long and intense NIR wavelengths a silicon (Si) wafer is placed in the beam path at Brewster's angle for 800 nm ($\sim$74 degrees). As the Si wafer suppresses the NIR radiation more strongly than it does the shorter wavelengths, it acts as a spectral filter, while reducing the overall intensity. The RDW is nearly isolated and the UV waveform can be measured with reduced intensity. The resulting field of the filtered light, which is the NPS current signal corrected by the gating function is shown in Fig. 6.1 a). The corresponding spectrum, derived via Fourier transformation, is plotted together with the spectral phase in Fig. 6.1 b). Below, in Fig. 6.1 c) the spectrum is transferred to be wavelength-dependent.

This measurement shows that the RDW field and residual soliton is a few-cycle laser pulse with a spectrum reaching from 0.25 PHz to about 2.0 PHz, extending the bandwidth of NPS far beyond its earlier application regimes in the VIS-IR. The wavelength-dependent NPS spectrum allows direct comparison with one independently measured with an amplitude-calibrated spectrometer. The match at the peak of the RDW around 235 nm is excellent, while it has to be noted that the soliton tail (the wavelengths longer than $\sim$ 350 nm) could not be fully suppressed with one Si wafer. Moreover, these resulting spectral components in the higher

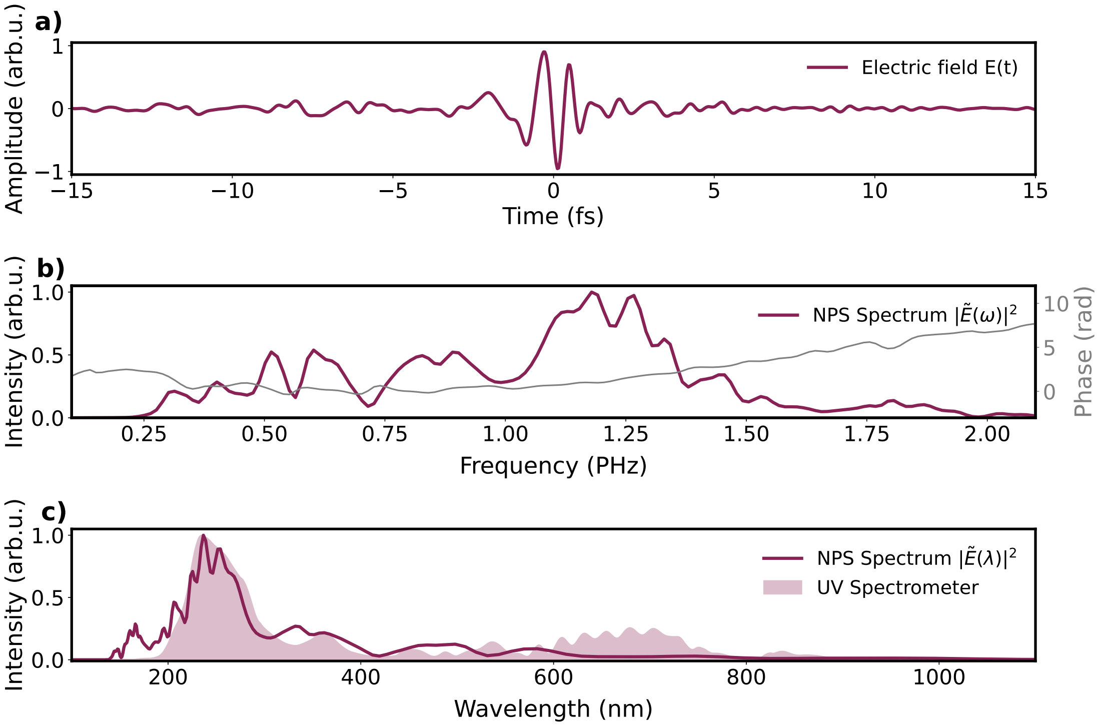

Figure 6.1: Field Sampling of a nearly isolated RDW by spectral filtering using a reflection of a Si wafer in Brewster angle suppressing the strong NIR radiation. In a) the electric field is plotted, and b) shows the Fourier transformed spectrum of the field in a), together with the spectral phase in grey. This spectrum has been transformed via Eq. 2.12 to depend on wavelength, rather than frequency, which is shown in c) for comparison with the spectrum measured with a spectrometer.

wavelengths exhibit a larger amplitude in the spectrometer, which can be explained due to spatial separation of the spectral components at the focal spot. That the wavelengths shorter than 180 nm are not seen by the spectrometer might come from the absorption in air. Later measurements with a nitrogen-flush exhibit a small peak at 170 nm.

In order to check the stability, the pulse has been measured in a smaller time delay window three times consecutively. The averaged electric field and standard deviation (std) are shown in Fig 6.2 a). Moreover, the intensity is plotted in b): on the one hand, the squared of the electric field from a) in purple, and on the other hand, the fields intensity envelope as black dashed line.

The electric field of a RDW in the DUV and some residual radiation in the VIS-NIR could have been reproducibly measured via NPS. From the intensity envelope a FWHM pulse duration of 1.2 fs can be derived, which is the shortest DUV pulse

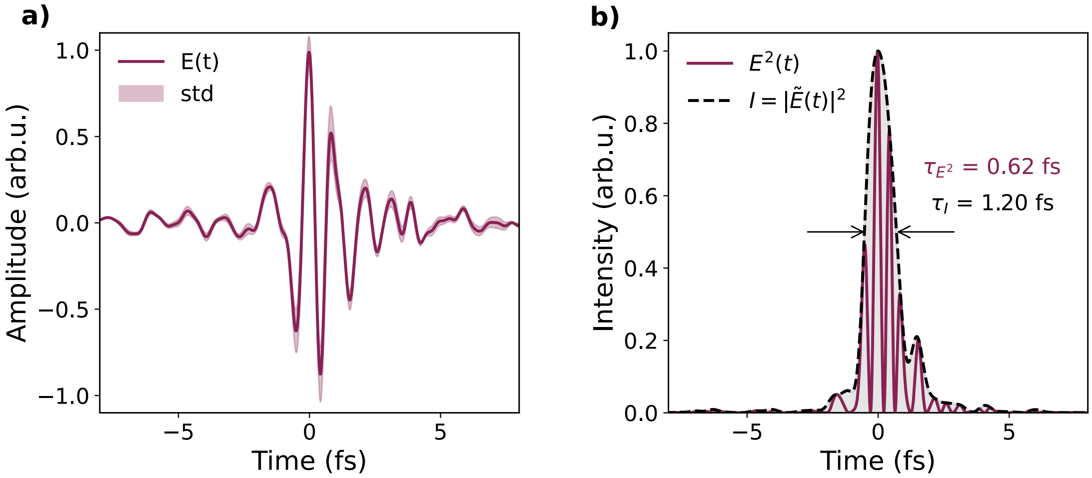

Figure 6.2: Average and standard deviation (std) of three nearly identical waveforms, comprising RDW emission spectrally filtered from the soliton by reflecting from a Si wafer in a) and the corresponding intensity distribution in b). The real electric field squared has a FWHM pulse duration of 0.62 fs, while the FWHM intensity envelope is 1.2 fs.

ever measured in a field-resolved manner. To summarize, in this work, the spectral bandwidth of the NPS technique has been extended up to 2 PHz, enabling the measurement of shorter wavelengths (down to 150 nm), and thus, shorter pulses. For the first time, a RDW can be studied with field-resolution by providing a field-sampling setup that covers this ultraviolet spectral range, measuring a squared electric field as short as 616 as. With only two half-cycles at FWHM, the generation and characterization of single-cycle pulses, having a central wavelength around 300 nm, is accomplished.

In order to extend the bandwidth of NPS towards the DUV, two requirements were needed. First, the gate pulse needs to be chosen such that the gating function can resolve the short wavelengths. Therefore, especially the laser intensity and pulse length have to be tuned to result in high-order multi-photon ionization only at one oscillation peak. Multiple ionization events would lead to less resolution, as explained in the methods (see e.g. Fig. 3.5). Moreover, the central wavelength is important, because the longer the wavelength, the broader is the pulse peak width and hence, the longer is the injection duration.

Secondly, the other requirement for DUV-NPS is regarding the medium and its properties. In a gas, a sufficiently large ionization energy should exist, similarly a wide bandgap for solids. Here, NPS is performed in argon, a noble gas with an ionization energy of 15.76 eV, which corresponds to 78.67 nm. With an NIR injection pulse with central wavelength around 700 nm (1.77 eV), injection could occur due to 9-photon ionization, an extremely nonlinear process, leading to a distinct gating function. In addition, it is important how the energy of the excited carriers is distributed in reciprocal space, since a short injection time can only occur when the conduction charge carriers have a broadband initial spread $\Delta E$. In a free electron gas, the total energy for electrons with mass $m_e$ can be written as $E = \hbar^2 k^2/2m_e$, showing a parabolic dependence of the energy to the wave vector $k = 2\pi/\lambda$, without limitations for a larger momentum $p = \hbar k$ induced by the drive pulse.

Depending on the band structure in solids, the energy dispersion of the conduction band deviates from the parabolic behaviour of free electrons. The population timescale of excited carriers in solids depends on the joint density of states, which potentially involves many conduction and valence bands. As shown by Ossiander *et al.* [9], injecting electrons into multiple bands inhibit the acceleration of the excited charges, and thus sampling of the driving field. Typically, solids hold very complex band structures with several bands that are even overlapping at different $k$ vectors. Hence, it would be difficult to find or design a sample that has the first conduction band (CB1) so far separated from higher bands that the DUV driving field with photon energies up to 8 eV accelerate the charges only along CB1 and cannot lead to population of larger bands.

Summarizing, considering the naturally occurring complex band structure of solids, it can be assumed that the here presented extraordinary broadband nonlinear photoconductive sampling would not work in solids, but does work in gas media by generating free electrons. As it was proven above that NPS in gas has excellent temporal resolution, being able to resolve the field of light with photon energies up to $\sim$ 8 eV (2 PHz), even shorter pulses being in the attosecond range should be measurable. This endeavour is covered in the following section.

## 6.2 Field-Resolved Self-Compressed Solitons: Attosecond Transients

In the measurements presented in this section, the Si wafer which suppresses the IR radiation as done in the previous section is removed. According to the theory, the resonant dispersive wave is emitted by a self-compressed soliton. By sending the full field exiting the HCF to the NPS gas sample, guided only with Al-MgF$_2$ mirrors, the self-compressed soliton should be measured together with its RDW by the above presented NPS. In this configuration, the intensity of this beam is not reduced and significantly higher than in the section before, where it was reflected from a Si wafer.

The drift current induced by this extremely broad DUV-NIR drive field is measured with NPS in the focus. In Fig. 6.3 the therefrom derived electric field is presented in a) and b), for drive CEPs 0 and $\pi/2$, respectively. With optimized settings and a CEP of zero, an attosecond light transient can be generated, proving the occurence of soliton self-compression. When changing the CEP drastically (b), the field changes more than just by a change of absolute phase, indicating that not only the CEP but also other perturbations influence the waveform when deviating from the optimal CEP settings.

The changes are even more visible in the intensity depiction, as shown in Fig. 6.3 c) and d). With the optimal CEP (c) an $E^2$ pulse duration of 323 as at FWHM was measured. Since this cosine pulse basically consists of a single half-cycle, the definition of an envelope ($|\tilde{E}(t)|^2$) is redundant. Nevertheless, it is shown as dashed line for comparison to the other case with different CEP (d), where the two central half-cycles rather represent a sine field with smaller peaks compared to the neighbouring cycles. Moreover, the two half-cycles next to the central cycle seem to be enhanced. Therefore, the $E^2$ FWHM pulse duration is much longer than in c), while the envelope duration is still comparable.

In the spectrum (e), derived via Fourier transformation of the field a), we can see that the soliton radiation in the VIS-NIR regime measured with NPS clearly matches the spectrometer-measured spectrum (dashed). On the contrary, the RDW at shorter wavelengths could not be measured with NPS, which we account to the high intensity of the soliton, leading to perturbations on the high-energetic DUV photons. In f) a spectrogram of the field in b) is shown to visualize the clear separation of the soliton and the measurable part of the RDW. When changing the CEP, the spectrum of a RDW and self-compressed soliton should not change drastically. Nevertheless, we see a stronger dip in the central frequencies for the non-optimized case. This behaviour indicates a worse NPS response for non-optimal CEPs.

From these measurements we conclude that the self-compressed soliton can be studied in this configuration, while the studies with focus on the DUV RDW has to be performed with lower intensities, separated from the strong soliton NIR peak around 950 nm, as in the section before. Moreover, to summarize, it is shown that the argon-based NPS allows sampling of a self-compressed soliton and RDW emission with sub-fs pulse duration. The measurements prove the importance of the CEP tunability as the generation of an attosecond field transient can not be investigated and optimized by only measuring the envelope. By optimizing the CEP we can tune the input pulse and measure the resulting electric field coming out of the HCF, optimizing the self-compressed soliton and receive the shortest possible waveforms.

In the following, soliton dynamics are presented that were studied with this arrangement. First, the results are compared with numerical simulations, presenting the evolution of a self-compressed soliton along the hollow-core fiber. Afterwards, the dependence of the outcoming field on the entrance gas pressure is shown, confirming the theoretical characteristics of solitons as described in section 2.2.3.

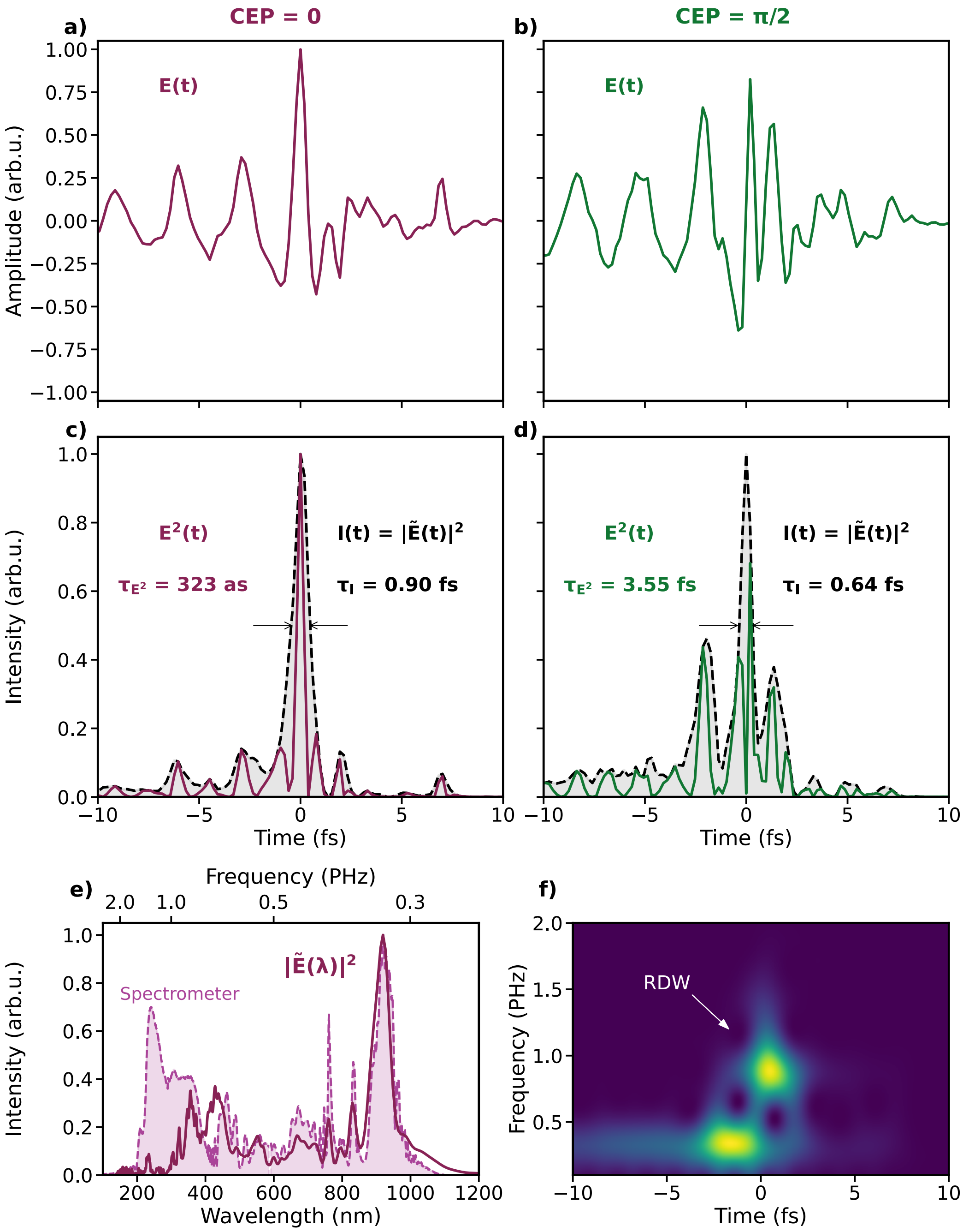

Figure 6.3: NPS of self-compressed soliton for two cases: optimized CEP in the three left panels vs. not optimized in the right panels. In a) and b) the electric field is derived from the NPS current signal with two different drive CEP, but theoretically identical injection. When optimizing the system (a), an attosecond light transient can be generated. In c) and d), the fields of a) and b) are shown in intensity representation, respectively. In the optimized case (c) an sub-cycle transient of $\sim 320\,\text{as}$ was generated, showing the importance of CEP tunability. In e) and f) the spectrum and spectrogram of the fields are presented.

## 6.3 Exploring Soliton Behaviour

### Insights from Simulations

Thanks to the numerical simulations by Francesco Tani, the measurements performed during this PhD can be compared with theory. The basic concept of soliton formation, explained in section 2.2.3, in a gas-filled HCF is visualized in Fig. 6.4 a). When the input field propagates through the fiber with 10 bar He at the entrance and vacuum at the exit, it evolves over the fiber length (from back to front).

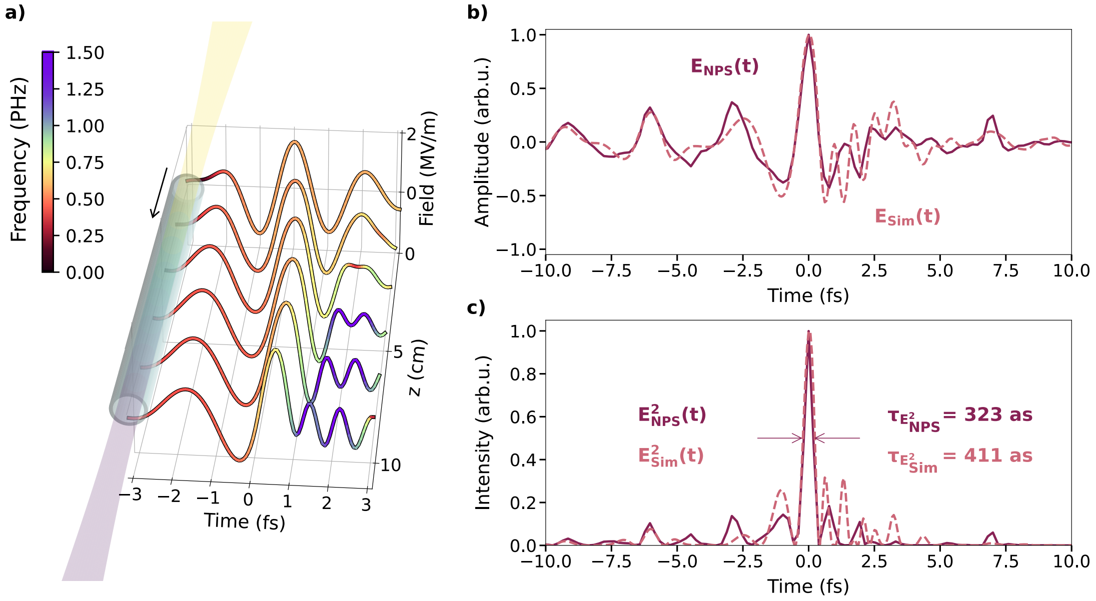

Figure 6.4: The evolution of the electric field while propagating through the HCF is simulated. In a) six electric fields with coinciding CEP are plotted as they evolve along the fiber (from back to front). The shortening of the primary half-cycle by soliton self-compression and the emergence of a DUV resonant dispersive wave is visible especially via the color-scale, indicating the instantaneous frequency of the field (DUV = purple). The image is reprinted from [108]. In b) the measured electric field after the fiber (solid line) is compared with the simulated field at the fiber exit (dashed line). These fields are shown in intensity depiction in c), being compared in pulse duration ($E^2$ FWHM).

With these pressure settings, the group velocity dispersion $\beta_2$ is negative and the soliton order N becomes greater than 1 (Eq. 2.31), allowing for soliton fission. First, SPM takes place, broadening the spectrum and changing the instantaneous frequency of the electric field, resulting in a redshifted rising edge and a blueshifted trailing edge, which is clearly visible in the left panel. The negative dispersion of the waveguide mode compensates this newly induced positive chirp and steepens the trailing edge of the field, which again leads to further SPM. Due to perturbations, this circle continues and leads to extreme pulse compression, resulting in a self-compressed soliton, which eventually breaks up and emits a resonant dispersive wave, after roughly 8 cm in this setup. Here, the self-steepening of the carrier wave (so-called carrier shock) is less pronounced than in the mid-IR range [109,110]. However, this effect is essential for achieving pulse durations of a few hundred attoseconds and for enhancing the conversion efficiency of the RDW.

In Fig. 6.4 b), the measured electric field exiting the fiber after 12 cm (solid line) is compared with the simulated field (dashed line) for the same parameters. The simulations are performed with the code described in [107] and use a measured field, acquired via NPS without fiber, as input. Consequently, the measured and simulated electric fields match excellent for the central half cycle and also agree quite well with the rising edge of the field. The high frequencies on the trailing edge were difficult to resolve experimentally and would need isolated studies as mentioned above, while the measured low frequencies agree with simulations. The intensity distribution of the two cases, shown in Fig. 6.4 c) compares the $E^2$ pulse duration of the two cases, varying by less than 100 as. As presented before, experimentally we achieve a pulse duration as short as 323 attoseconds at FWHM. In the simulations, the duration of the squared field is 411 as. The differences can be accounted to the low resolution of high frequencies in this intense soliton configuration. All in all, the measured electric field matches well with the soliton simulations at the fiber exit, meaning that the generation of a self-compressed soliton is proven.

## Pressure Scan

By changing the input pressure of the HCF, and measure the electric field with NPS, we can show the RDW behaviour in a field-resolved manner, enabling studies of the evolution of solitons. In Fig. 6.5, the electric field a) and the corresponding spectra b), derived via complex Fourier transformation, are presented for the input pressures between 1 bar and 10 bar helium. At low pressures, only minor effects occur, showing increasing spectral broadening towards the ultraviolet with increasing input pressures. The higher the pressure, the higher the soliton order becomes. At 6 bar and 7 bar, the soliton order according to Eq. 2.31, is $\mathrm{N} \sim 1.38$ and $\mathrm{N} \sim 1.52$, respectively. Hence, the requirements for the emergence of soliton self-compression and resonant dispersive wave emission is fulfilled from these pressures onwards.

In the beginning, the RDW is emitted at wavelengths around 200 nm. Then, the higher the pressure, the longer the wavelength at which the RDW phase-matches with the soliton. At 10 bar, the soliton order reaches $\mathrm{N} \sim 1.95$, leading to higher conversion efficiencies of the energy transfer from the soliton to the RDW, resulting

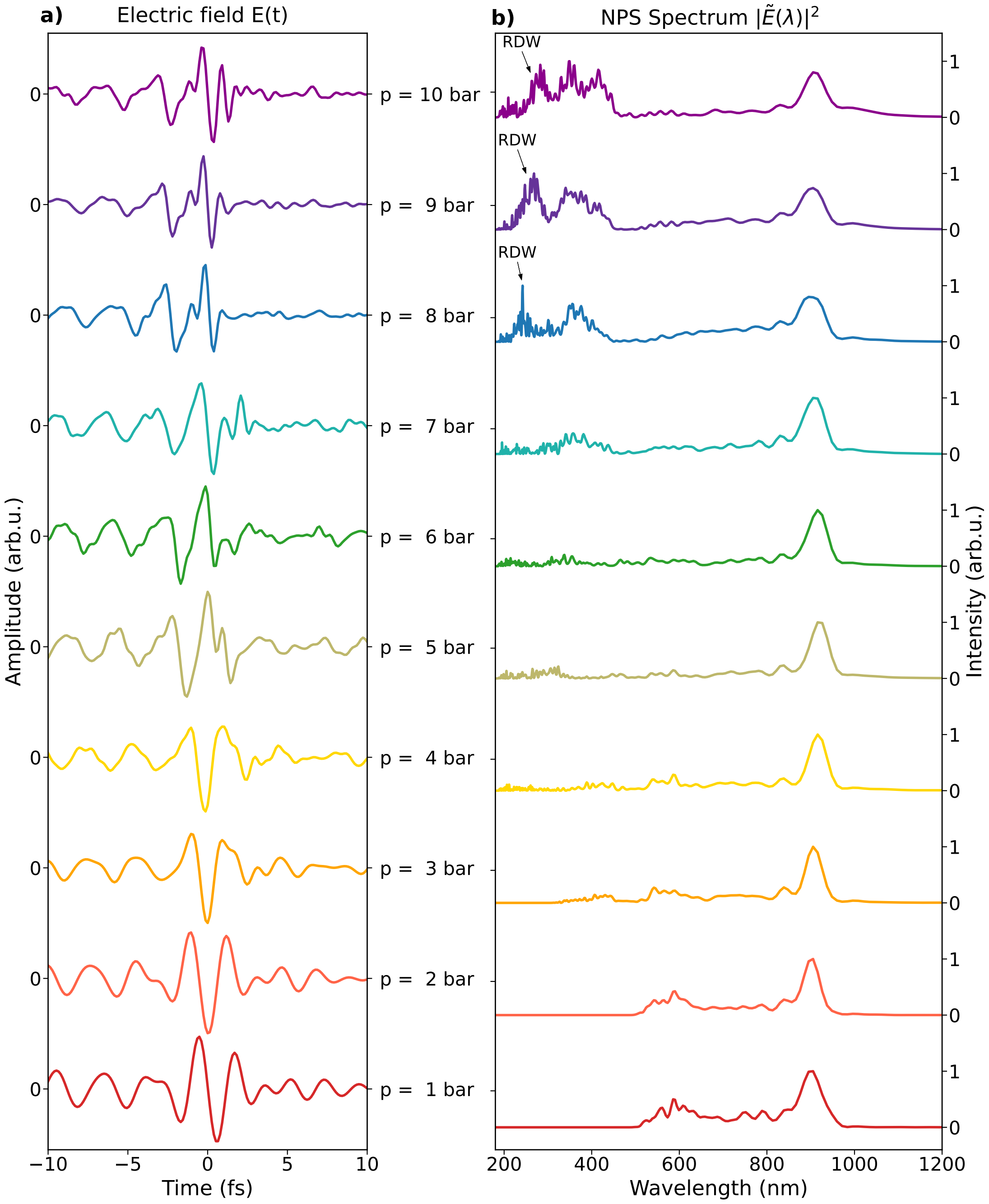

Figure 6.5: HCF input pressure tuning from 1 to 10 bar helium at constant input laser intensity. The soliton order N increases with higher pressures, and exceeds 1.5 at 7 bar, starting to enable soliton-self-compression and RDW emission. With increasing pressures, the RDW phase-matching wavelength shifts to higher wavelengths and the increasing soliton order displays a raising efficiency of energy transfer towards the phase-matched DUV RDW.

in a more intense DUV peak and reduced NIR radiation. In addition to the results in section 5, where the pressure scan was recorded with a spectrometer and compared with simulations, now the field-resolved signal allows for optimizing the RDW in its entirety, including the phase.

## 6.4 Nonlinear Processes Induced by Attosecond DUV-NIR Pulse

The intense attosecond deep-ultraviolet (DUV) pulse enables nonlinear optical effects, paving the way for novel approaches in attosecond-pump, attosecond-probe spectroscopy (APAS). Here, it is demonstrated that the attosecond DUV-NIR pulse can serve as an ultrashort gate, directing ultrafast dynamics and facilitating future APAS setups. In this experiment, the configuration depicted in Fig. 5.1 is modified to utilize the pulses for reversed purposes. By adjusting the pulse intensities such that the DUV beam becomes much stronger than the NIR beam, and rotating the electrodes by 90 degrees, the roles of the two pulses are interchanged. As shown in Fig. 6.6 a) the electrodes are typically left and right of the gas jet, aligned to the p-polarization of the previous drive field. Now, in the rotated configuration shown in b), the electrodes are above and below the gas jet, aligned with the s-polarization of the NIR beam, serving now as a drive field. The DUV-NIR self-compressed soliton and RDW emission serves as an ultrashort injection, providing the gate for field sampling.

In order to determine if the reversed configuration measurement of the NIR field yields reasonable results, it is compared with the initial configuration, which measures a similar NIR field. Therefore, the fiber in the initial drive arm was removed, and the NIR pulse that typically serves as fiber input was measured. The electric field of the drive pulse in the initial configuration is shown in c), while the field measured in the rotated configuration, with ultrabroadband injection, is presented in d). Moreover, in both cases, the intensity envelope is shown, yielding pulse lengths of 2.44 fs and 2.14 fs, respectively. Since the new configuration (b) uses a different injection pulse, the NPS signal has to be corrected by another response function. As the two arms are separated with a perforated mirror, one arm consists of the central part and the other of the surrounding part (doughnut shape). Here, the two configurations measure each one of the arms, exhibiting different strengths of certain spectral components, which can be seen in the spectra in e) and f). However, each NPS spectrum is compared with spectrometer acquisitions, showing a reasonable match. It can be concluded that the small differences in the two configurations are due to the different properties of the central vs. the outer beam. The different frequency proportions, the different beam shape, especially

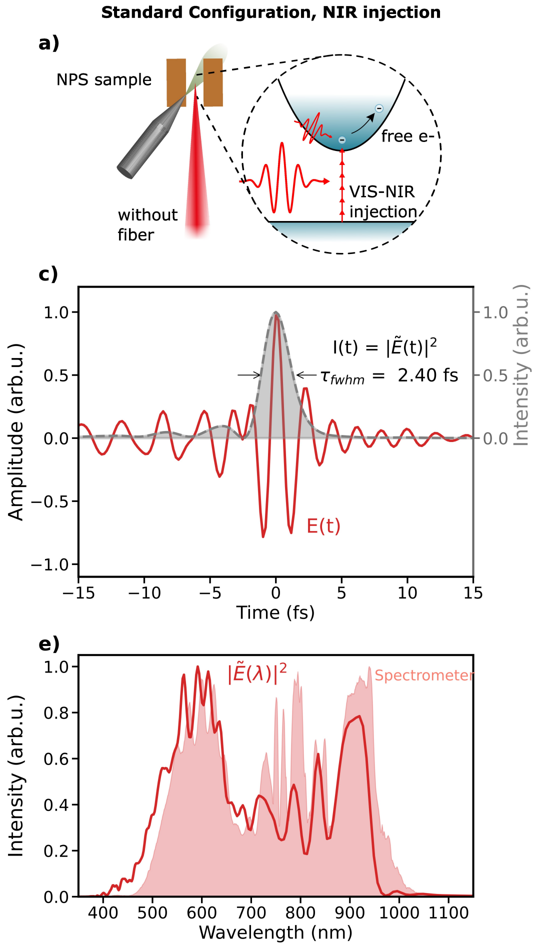

Figure 6.6: The standard NPS setup with two electrodes besides the argon jet and the working principle is shown in a). For comparison, i.e. to measure the fiber input NIR field, the fiber is here removed and UV is not generated. In b) the reversed setup with rotated NPS sample is presented. Here, the attosecond DUV-NIR beam serves as the injection pulse and the NIR beam as the drive. c) and d) show the measured NIR electric fields for the different configurations, exhibiting a FWHM pulse duration of 2.44 fs and 2.14 fs, respectively. The corresponding spectra, the Fourier transformed NPS fields, are shown in e) for the standard configuration and f) for the reversed configuration, each together with the spectrum measured with a spectrometer.

influencing the focus, and the different response functions are sources of deviations between the two measurements. Hence, it can be concluded that the reversed setup shows appropriate results, indicating that NPS is demonstrated with DUV injection. As single-photon ionization in argon occurs at 78.67 nm, the photoionization by the RDW is at least a two-photon or three-photon process. In summary, it has been shown that the self-compressed soliton and RDW emission can trigger nonlinear effects, enabling future APAS experiments.

In conclusion, in this chapter it has been shown that soliton self-compression and resonant dispersive wave emission in hollow-core fibers is a valuable phenomenon being extremely useful for conducting field-resolved application experiments with intense attosecond pulses. By carefully selecting parameters such as fiber diameter, length, and gas composition, it becomes possible to achieve direct emission of single-cycle transients spanning the NIR to DUV regions without the need for post-compression, resulting in a compact and reproducible attosecond light source. In combination with the field-sampling technique NPS, responding not only in the UV-IR, but now proven to be applicable also to DUV fields up to 8 eV, the investigation of ultrafast light-matter interactions in a new energy regime (between 4 and 8 eV) is enabled. The extension of the NPS bandwidth allows for field-resolved measurements of DUV laser pulses that were interacting with wide-bandgap solids being important for optoelectronics, or molecules, e.g. with biological meaning, such as aromatic amino acids, naturally occurring in human blood plasma.

# Chapter 7

# Summary and Discussion

Resolving the dynamics of matter in time allows understanding of the underlying processes, mechanisms and possible methods of control. For instance, in medicine, various studies of diseases have been performed over long time scales, in order to track the typical development of health conditions. Likewise, in emergencies it is crucial to monitor the vital values of patients and their symptoms over time, in order to perform the correct diagnostic analysis and help accordingly. Now, what about the processes that are so fast that humans cannot see them and electronic devices cannot detect them? As our world consists of matter, being composed of electrons, protons and neutrons in different configurations, and movements of electrons typically happen on an ultrafast time scale, the question is how these dynamics can be observed and understood to form and improve our daily lives.

The ultrafast timescale of electron dynamics lies in the range of attoseconds ($10^{-18}$ s). Advancements in attosecond physics provided measurement schemes and tools to study these ultrafast dynamics through ultrashort light pulses with specific wavelengths. Since electrons are part of all common materials (solids, liquids as well as gases), the energy range on which they can interact is tremendous. Fortunately, the electromagnetic spectrum covers an extremely broad range of photon energies, allowing researchers to investigate and steer all kinds of interactions. In attosecond metrology, the electronic behaviour is driven on its natural timescale and with the desired energy through the electric field of ultrashort pulses. Extensive research of and with these metrology techniques resulted in great revelations, such as the ultrafast switching of dielectrics with PHz frequencies via light-matter interaction, a few hundred thousand times faster than current electronics.

However, many types of electron dynamics are still uncovered, especially in wide-bandgap solids and molecules with energy transitions in the ultraviolet range. Existing metrology techniques have been proven to operate in the near-UV to mid-IR, and with extreme UV radiation, but the spectral range in between, the deep-UV (DUV) and vacuum-UV (VUV) (see Appendix A.1), could not be investigated yet.

One reason for this is the challenging generation of DUV pulses on the few- and subfemtosecond (attosecond) timescale. Another reason is the undiscovered mirror technology and material research in this regime, such that the metrology techniques could not be further extended. A complete field characterization technique in the DUV-VUV wavelength range has to date been missing.

This dissertation introduces the generation of deep-UV pulses with unrivaled temporal compression in this spectral regime, as well as the extension of the photoconductive sampling technique enabling the detection of this radiation in all its properties. Three metrology techniques are presented, their limits are tested and experiments have been performed to extend their bandwidth. Then, different DUV generation mechanisms have been investigated. All results have been performed with a phase-stable visible to near-IR laser source with a central wavelength around 750 nm and pulse durations of ∼3 fs.

The first used measurement technique, known as attosecond streaking uses large-scale infrastructure and requires expensive optics and devices. Moreover, long integration times are needed for sufficient signal. As a consequence, attosecond metrology developed into a new direction, providing more compact and flexible solutions for pulse characterization. In this work, photoconductive sampling is introduced as an alternative to attosecond streaking. Linear photoconductive sampling (LPS) has been found to require different photon energies and injection intensities as attosecond streaking, mostly steering the lower energetic electrons as they have higher intensities (compare Chapter 4.1). This finding experimentally proves the theoretical prediction and enables the determination of the limitations of this technique more precisely, as discussed below.

Spectral filtering as typically performed in attosecond streaking is disadvantageous for LPS, since it reduces the intensity of the lower energetic photons drastically. As this spectral filtering acts also as a temporal filter, the absence leads to longer XUV pulses, a high harmonic pulse train. This work points out that an LPS setup using high harmonics as injection pulse is not suitable for sampling ultraviolet radiation (as presented in Chapter 4.2). It was concluded that the pulse duration of the XUV pulse without spectral filtering is too long to act as an ultrashort gate and resolve ultraviolet radiation. For future LPS measurements, a different XUV generation mechanism would be needed, delivering shorter XUV pulses.

In this work, the third measurement technique, nonlinear photoconductive sampling (NPS), was used instead for further advancements, as it was proven to operate already up to 1.1 PHz in previous works [10], resolving the mid-IR, visible and even the near and mid-UV regime. However, the spectral region with wavelengths between 275 nm and the XUV, remained inaccessible to field sampling techniques. Here, the development of a suitable NPS setup, using a gas sample and two electrodes to detect UV radiation in a vacuum chamber is presented (in Chapter 5.1).

Hence, for the first time, a solution is found to fill the DUV gap of field sampling techniques.

The generation of ultrashort DUV pulses was first performed via spectral broadening in a gas-filled hollow-core fiber (HCF). Using the short input pulses of the VIS-NIR laser setup and its high intensities, self-phase modulation (SPM) led to spectral extension down to 170 nm, detected with an UV spectrometer. Introducing this setup into the developed NPS setup, showed the field-resolved measurements of UV for the first time in this work (in Chapter 5.2). However, due to the nature of SPM, the fiber output pulse was positively chirped, resulting in pulse durations >7 fs as detected by NPS. Unfortunately, these pulses cannot be compressed with the current chirped mirror technology, as suitable coating materials are not available, according to collaborations with optics designers. Thus, it was concluded that using a different generation mechanism that directly emits an ultrashort pulse is the only solution at the current state of the art.

As a consequence, another DUV generation technique was introduced, resulting intrinsically in an ultrashort pulse, such that post-compression is not necessary. The recent advances in soliton dynamics were applied to the existing laser system and could be adapted in order to arise soliton self-compression, allowing for the emission of a resonant dispersive wave in the DUV. Using the few-cycle, broadband VIS-NIR input pulse and developing a suitable HCF setup (Chapter 5.3) led to an even shorter output pulse, with record-breaking pulse durations in this spectral regime. Single-cycle DUV pulses with intensity envelope durations as short as 1.2 fs were reported, resolved in a field-resolved manner, including the phase information (Chapter 6.1).

Additionally, the self-compressed soliton in the VIS-NIR region was successfully resolved with this NPS setup, presenting a field-resolved measurement of this phenomenon in HCF for the very first time. The measured fields could be tuned with dispersion and CEP optimization to result in attosecond sub-cycle light transients with $E^2$ pulse durations around 320 as (Chapter 6.2). Through comparisons with simulations and a pressure scan, the soliton dynamics in the HCF were discovered (Chapter 6.3). Moreover, the intense attoseconds transients were used as nonlinear injection pulse, enabling measurements of an VIS-NIR pulse and thus proving the applicability of these pulses for studies of nonlinear optics (Chapter 6.4).

In summary, this dissertation worked out a suitable DUV generation technique delivering ultraviolet pulses shorter than 1.3 fs: resonant dispersive wave emission via soliton self-compression. The complete setup is a compact and reproducible attosecond light source with comparably high pulse energies. In comparison with lightwave synthesizers, an improved stability is expected, since the generation is taking place in a single beam path. In addition, a field metrology technique was presented operating up to 2 PHz, frequencies in the VUV, a previously undiscovered sampling regime. The results presented here provide a unique and user friendly solution to investigate a new class of attosecond experiments, in the energy range between 4 eV and 8 eV. This range is suitable e.g. for large-band gap semiconductors for opto-electronical devices, but also a wide range of molecules.

Further advancements can be made on the setup to optimize it for better signal to noise ratio, finely resolving the DUV while the strong NIR peak is present. Moreover, the differential pumping unit of the fiber setup should be improved, e.g. with a second stage, as the extreme pressure gradient from 10 bar to vacuum leads to a tremendous gas load for the turbo pump, running it close to the limit. Further investigations can be made with different NPS samples, different gases or specially designed materials, as well as with different types of electrodes and advanced electrical engineering for noise reduction and signal enhancement. In addition, the UV separation should be optimized by replacing the Si wafer by different optics, testing e.g. dichroic wedged beam separators used in [51] for high harmonic DUV pulses with durations of 1.9 fs, or customized beamsplitters. Furthermore, the influence of CEP and dispersion needs further investigation, as the change of input CEP, counteracting with a wedge in the injection arm changed the field measurement more than expected.

However, the current state of the setup can readily be used for experiments, such as time-resolved spectroscopy, using pump-probe schemes to study electron dynamics. The following outlook presents new research opportunities enabled by this newly developed apparatus, a key technology for investigating light-matter interactions on the attosecond timescale in a previously inaccessible spectral range of 4 eV to 8 eV.

# Chapter 8

# Outlook

The developed setup and corresponding results presented in this dissertation pave the way for a new class of attosecond experiments: studies of light-matter interactions with unprecedented time resolution and previously inaccessible energy range. The most fundamental interaction is the charge separation in matter induced by an electric field: the polarization. Sampling the electric field $E(t)$ of an ultrashort, intense laser pulse after propagating through a medium and comparing it with a weak reference measurement can directly yield the nonlinear polarization $P_{NL}$ of the medium induced by the strong field. With the knowledge of the time-dependent electric field and nonlinear polarization, the energy transfer from the electric field to the medium can be determined as a function of time [2], allowing time-resolved studies of the charge carrier dynamics. Now, with the newly developed apparatus, the time resolution is eminently improved and the energy transfer through the single-cycle UV pulses could take place within less than 1 fs, pushing the speed of signal processing. Moreover, attosecond experiments in a new frequency range are now possible, as not only the generation of attosecond pulses in the DUV-NIR region was presented, but also a suitable metrology technique, resolving this spectral region up to 8 eV. Hence, the physical properties studied in previous experiments can now be investigated with better time resolution, capturing faster dynamics, and at different energy ranges. Fundamental examples are discussed below in detail.

Attosecond chemistry became a new established research field approximately one decade ago. XUV-pump/IR-probe experiments are the key technology to study the dynamics of molecules [32, 33], first ionizing the molecule and generating an electronic wavepacket, a coherent superposition of electronic states, and then probing the charge migration by changing the time delay between pump and probe. However, certain transitions, e.g. between highest occupied and lowest unoccupied molecular orbitals (HOMO and LUMO, respectively) can only be steered by DUV pulses with sub-fs ionization, as theoretically predicted [3]. Since these DUV pulses have not been generated and charactarized in a field-resolved manner before this work, such experiments stayed inaccessible. Now, with the DUV advancements, the RDW can be be tuned to be resonant with the transition and initiate the desired charge migration, while the extended NPS metrology technique can observe the changes in the DUV pulse. As several molecules exhibit many excited electronic states in the LUMO separated by approximately 5-8 eV from the HOMO, an excitation with a broadband DUV pulse would lead to a superposition of electronic and vibrational states. Hence, the electronic coherences and their decay can now be studied directly for the very first time, as this phenomenon cannot only be induced by the ultrashort DUV pulse, also the emitted broadband radiation can finally be detected with the extended NPS metrology setup presented in this dissertation.

Moreover, this research can be extended from fundamental chemistry to biology and medicine. Recent advancements in field-resolved infrared spectroscopy allow sampling of molecular vibrations after few-cycle IR excitation in biological systems [87]. With electro-optic sampling, the optical coherence is measured in complex molecular ensembles with broadband excitation from 5 to 12 $\mu$m, by investigating the excited molecular vibrations and corresponding decay on the typical vibrational response times and energies. With this technique, human blood plasma and its molecular composition can be studied in detail. Further research may allow an evaluation of a human's health condition, providing a person-specific fingerprint and detecting cancer in very early stages. The ultrashort DUV source and metrology technique presented here enable the extension of this measurement scheme and can hence deliver complementary information about the molecule's properties. The electronic wavepacket, impulsively excited by the single-cycle DUV pulse, will perform oscillatory charge migration within the molecule and radiates accordingly in this UV regime. Measuring the decay of this radiation with the NPS attosecond resolution provides direct information about the lifetime of the electronic coherence in the molecules, in chemical systems as mentioned before as well as in biological samples, extending the molecular fingerprint with its electronic component.

In addition, the single-cycle DUV pulses presented here can be applied to investigate electron dynamics in wide-bandgap solids. Due to the great tunability of the RDWs, the photon energy can be tuned to be resonant with the transitions between the valence and conduction bands. Hence, several materials can be investigated with such pump-probe spectroscopy. In a perfectly controlled fashion, an attosecond Bloch wavepacket can be launched by the single-cycle UV pulse, linearly exciting the solid, and subsequently steered by the ultrashort probe (drive) pulse (similar to the process in Fig. 6.6 b) but in a solid). Then, in a subsequent focus, the modified transmitted drive electric field can be measured with NPS, carrying the information about the induced polarization and corresponding details about the injected wavepacket. Previous measurements could only study 'slow' dynamics in wide-bandgap materials with nonlinear photon-absorption and longer injection pulses, and thus only after a few femtoseconds [111]. With the new DUV setup, enabling linear excitation on the attosecond timescale, the motion of the Bloch wavepacket within the first femtosecond can be studied for the first time. Moreover, electronic decoherence phenomena could be studied in these solids, e.g. via the measurement of HHG emitted from the excited sample as a function of time delay between pump and probe. An extensive amount of undiscovered, ultrafast, and fundamental electronic processes in semiconductors and dielectrics with bandgaps in the UV region can now be studied with extraordinary attosecond resolution.

In summary, the above presented outlook shows that the setup and attosecond DUV-NIR source presented in this PhD work offer a great number of new research opportunities, extending the energy range up to 8 eV and investigating time-resolved charge and energy transfer in various systems with extraordinary resolution.

# Appendix A

# Supplementary Information

## A.1 Relevant Spectral Regions of Light

Attosecond metrology uses ultrashort light pulses in various spectral regions. To provide a general overview, the most important regions of the electromagnetic spectrum are presented in Fig. A.1 in wavelength, frequency and photon energy description.

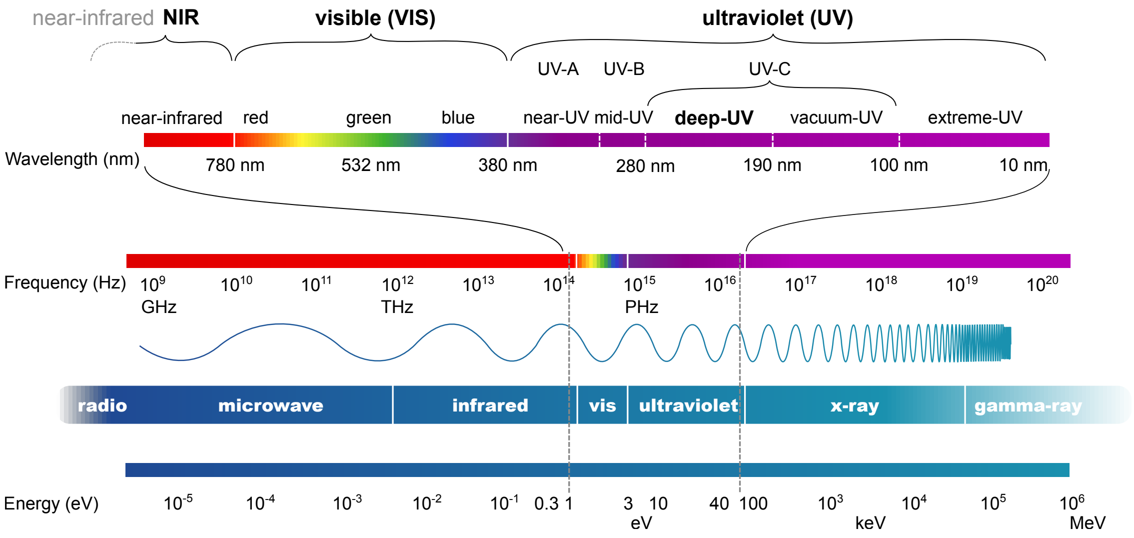

Figure A.1: Overview of the different regimes of the electromagnetic spectrum in order to emphasize the importance of the spectral regions discussed in this work. The input laser source covers the visible region and reaches into the NIR (400-1050 nm). The spectrum was extended via self-phase modulation down to 170 nm, covering also the near-UV, mid-UV and deep-UV. Via resonant dispersive wave emission, the pulse durations were reduced, and the spectrum reached similarly from NIR to DUV, down to 150 nm. Via high harmonic generation, radiation was generated in the XUV regime, up to approx. 70 eV.

The visible and ultraviolet region covers only a small fraction of the electromagnetic spectrum, but as shown above, a quite central range. In this work, the NIR to XUV wavelengths are discussed, and hence highlighted in the scheme. Field sampling techniques were previously operated with radiation in the XUV range and mid-UV to infrared. However, the electric field of ultrashort pulses could only be measured down to 275 nm and the lower wavelength region, such as the deep-UV and vacuum-UV, remained missing. In this work, the field sampling bandwidth was extended, providing an NPS measuring up to 2 PHz (8 eV / 150 nm). Thus, the complete DUV region is now covered, even reaching into the VUV.

## A.2 Photoconductive Sampling Data Processing

For the sections in chapters 4,5 and 6 that contain measurements with photoconductive sampling, it has to be noted that the measured delay-dependent signal, the electric current $I_{drive}(\tau)$, maps the vector potential of the drive pulse $A_{drive}(t)$ convolved with a gating function $G(t-\tau)$. In the frequency domain, we can write Eq.3.5, such that we can simply divide the current with the complex response function $\tilde{G}^*(\omega)$ to obtain the pure vector potential.

For nonlinear photoconductive sampling (NPS), the response function $\tilde{G}^*(\omega)$, which is the complex conjugate of $\tilde{G}(\omega) = \Re(\tilde{G}(\omega)) + i\Im(\tilde{G}(\omega))$, was theoretically derived via numerical solving the time-dependent Schrödinger equation (TDSE) with the tRecX code [112] in the single active electron approximation by Manoram Agarwal. In the typical case, in which the VIS-NIR laser pulse is used as injection, the response function has been found to be quite flat in the spectral region covered by the pulse (0.25 - 2.0 PHz), as shown in Fig. A.2.

In order to derive the electric field from the measured photocurrent, the data is processed as follows. First, the signal is multiplied with a tukey filter in the time domain. Moreover, zero-padding is implemented to smoothen the spectrum. Secondly, the signal is Fourier transformed to the frequency domain, where a super-Gaussian bandpass filter is applied. Thirdly, as explained above, the signal is corrected by the response function $\tilde{G}^*(\omega)$. In addition, the electric field is derived from the vector potential via multiplication with $i\omega$, as it is defined via $\tilde{E} = -\frac{\partial \tilde{A}}{\partial t} = i\omega \cdot \tilde{A}$. Finally, the inverse Fourier transformation is applied. In summary, the following transformation has been performed:

$$\tilde{E}(t) = \mathrm{iFFT}\left(\frac{i\omega \cdot \mathrm{FFT}(I_{drift}(t) \cdot \text{tukey-filter}) \cdot \text{sg-bandpass-filter}}{G^*(\omega)}\right) \tag{A.1}$$

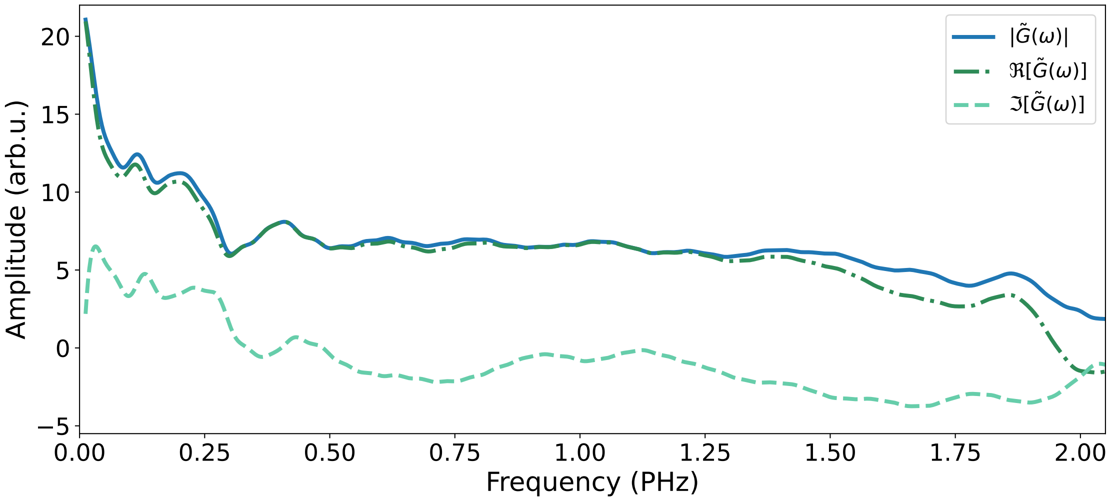

Figure A.2: NPS response function derived numerically by Manoram Agarwal for the FP3 injection pulse, by solving the TDSE with the tRecX code [112].

For linear photoconductive sampling, similar data processing has been performed, but the measured current is not corrected for the response function, as the efforts of the numerical calculation were not needed for the performed comparisons. Hence, in Chapter 4, the electric field is derived via:

$$\begin{aligned}\tilde{E}_{LPS}(t) &= \tilde{E}(t) \cdot \tilde{G}(t) \\ &= \text{iFFT}\left(i\omega \cdot \text{FFT}(I_{drift}(t) \cdot \text{tukey-filter}) \cdot \text{sg-bandpass-filter}\right)\end{aligned} \tag{A.2}$$

# Appendix B

# Data Preservation

The data and figures presented in the chapters 2 to 6 are archived on the Data Archive Server of the Laboratory for Attosecond Physics at the Max Planck Institute of Quantum Optics by Vladislav Yakovlev. Separate folders are created for the content of the different figures. The figures containing experimental data are generated from the raw data with data processing scripts. The python scripts required for the data analysis are provided together with the figures and raw data in each folder. An overview of the figures is given below.

| | |
|---|---|
| Figure 2.1 | schematic plot (.pdf), and generating script (.py) |
| Figure 2.2 | schematic plot (.pdf), and generating script (.py) |
| Figure 2.3 | schematic plot (.pdf) |
| Figure 2.4 | schematic plot (.pdf) |
| Figure 2.5 | reprinted figure (.png) from L. Rego, et al. [72] |
| Figure 2.6 | reprinted figure (.png) from F. Krausz and M. Ivanov [7] |
| Figure 3.1 | schematic plot (.pdf) |
| Figure 3.2 | schematic plot (a.pdf) and reprinted figure (b.png) from F. Krausz and M. I. Stockman [76] |
| Figure 3.3 | schematic plot (.pdf) |
| Figure 3.4 | schematic plot (.pdf) |
| Figure 3.5 | schematic plot (.pdf), and generating script (.py) |
| Figure 3.6 | schematic plot (.pdf), adapted reprint from S. Sederberg, et al. [10] |
| Figure 4.1 | schematic plot (.pdf), generating script (.py), and raw data (.npz). |
| Figure 4.2 | schematic plot (.pdf), generating script (.py), and raw data (.npz). |

| | |
|---|---|
| Figure 4.3 | schematic plot (.pdf), generating script (.py), and raw data (.npz and .txt). |
| Figure 4.4 | schematic plot (.pdf), generating script (.py), and raw data (.npz). |
| Figure 4.5 | schematic plot (.pdf), generating script (.py), and raw data (.npz and .txt). |
| Figure 4.6 | schematic plot (.pdf), generating script (.py), and raw data (.npz). |
| Figure 4.7 | schematic plot (.pdf) |
| Figure 4.8 | schematic plot (.pdf), generating script (.py), and raw data (.npz, .hdf5 and .csv). |
| Figure 4.9 | schematic plot (.pdf), generating script (.py), and raw data (.npz, .hdf5 and .csv). |
| Figure 4.10 | schematic plot (.pdf), generating script (.py), and raw data (.npz, .hdf5 and .csv). |
| Figure 4.11 | schematic plot (.pdf), generating script (.py), and raw data (.hdf5). |
| Figure 5.1 | schematic plots (.pdf) |
| Figure 5.2 | pictures (.png) |
| Figure 5.3 | schematic plot (.pdf), generating script (.py), and raw data (.npz and .csv). |
| Figure 5.4 | schematic plot (.pdf), generating script (.py), and raw data (.npz, .mat, .txt and .csv). |
| Figure 5.5 | schematic plot (.pdf), generating script (.py), and raw data (.npz, .mat, .txt and .csv). |
| Figure 5.6 | schematic plot (.pdf) |
| Figure 5.7 | pictures (.jpeg /.png) |
| Figure 5.8 | schematic plot (.pdf), generating script (.py), and raw data (.npz, .txt and .csv). |
| Figure 6.1 | schematic plot (.pdf), generating script (.py), and raw data (.npz, .mat, .csv). |
| Figure 6.2 | schematic plot (.pdf), generating script (.py), and raw data (.mat and .csv). |
| Figure 6.3 | schematic plot (.pdf), generating script (.py), and raw data (.npz, .mat, .txt and .csv). |
| Figure 6.4 | schematic plot (.pdf), generating script (.py), and raw data (.mat, .txt and .csv). |

| | |
|---|---|
| Figure 6.5 | schematic plot (.pdf), generating script (.py), and raw data (.mat and .csv). |
| Figure 6.6 | schematic plot (.pdf), generating script (.py), and raw data (.mat, .txt and .csv). |
| Figure A.1 | schematic plot (.pdf) |
| Figure A.2 | schematic plot (.pdf), generating script (.py), and raw data (.csv). |

# Appendix C

# List of Author's Publications

## Publications related to this thesis:

- **A. Heinzerling**, F. Tani, M. Agarwal, V. Yakovlev, N. Karpowicz, and F. Krausz. "Field-resolved Attosecond Solitons", submitted.
  *The author built the experimental setup, performed the measurements and processed the data. The first draft of the manuscript was prepared by the author together with N.K. and F.T.*

### Conference Contributions:

- **Amelie Heinzerling**, Johannes Schötz, Francesco Tani, Nicholas Karpowicz, and Ferenc Krausz. "Field Sampling of Ultrashort Deep-UV RDW-Emitted Pulses", ATTO IX Conference, Poster, incl. Best Student Poster Award (2023).
  Abstract: `https://www.atto9.org/abstracts_book.php`

- **Amelie Schulte**, Corinna Konrad, Matthew Weidman, Nicholas Karpowicz, Johannes Schötz, and Ferenc Krausz. "Towards Field Sampling of Ultrabroadband Continuum Radiation from deep-UV to Near-IR", ATTO VIII Conference, Highlighted Poster (2022).
  Abstract: `https://sciences.ucf.edu/physics/atto/book-of-abstracts/`

- **Amelie Schulte**, Corinna Konrad, Julia Anthea Gessner, Matthew Weidman, Vladislav Yakovlev, Johannes Schötz, and Ferenc Krausz. "Towards Field Sampling of Ultrabroadband Continuum Radiation from deep-UV to NIR", Optica High-brightness Sources and Light-driven Interactions Congress 2022, Technical Digest Series, Optica Publishing Group, Conference Paper HW3B.3, Talk (2022).
  Abstract: `https://doi.org/10.1364/HILAS.2022.HW3B.3`

# Other publications:

- Jan Mathijssen, Zeudi Mazzotta, **Amelie M. Heinzerling**, Kjeld S. E. Eikema, and Stefan Witte. "Material-specific high-order harmonic generation in laser-produced plasmas for varying plasma dynamics", Applied Physics B **129**, 91 (2023).
  https://doi.org/10.1007/s00340-023-08034-7
- S. Dziarzhytski, M. Biednov, B. Dicke, A. Wang, P. S. Miedema, R. Y. Engel, J. O. Schunck, H. Redlin, H. Weigelt, F. Siewert, C. Behrens, M. Sinha, **A. Schulte**, B. Grimm-Lebsanft, S. G. Chiuzbăian, W. Wurth, M. Beye, M. Rübhausen, and G. Brenner. "The TRIXS end-station for femtosecond time-resolved resonant inelastic x-ray scattering experiments at the soft x-ray free-electron laser FLASH ", Structural Dynamics **7**, 054301 (2020).
  https://doi.org/10.1063/4.0000029

### Other Conference Contributions:

- **Amelie Schulte**, Jan Mathijssen, Kjeld Eikema, and Stefan Witte. "Towards High Harmonic Generation in Laser-Produced Plasma", OSA High-brightness Sources and Light-driven Interactions Congress 2020, OSA Technical Digest, Optica Publishing Group, Conference Paper ETh3A.4, Talk (2020).
  Abstract: https://doi.org/10.1364/EUVXRAY.2020.ETh3A.4

# Bibliography

[1] Martin Schultze, Elisabeth M Bothschafter, Annkatrin Sommer, Simon Holzner, Wolfgang Schweinberger, Markus Fiess, Michael Hofstetter, Reinhard Kienberger, Vadym Apalkov, Vladislav S Yakovlev, Mark I Stockman, and Ferenc Krausz. Controlling dielectrics with the electric field of light. *Nature*, 493(7430):75–78, 2013.

[2] A. Sommer, E. M. Bothschafter, S. A. Sato, C. Jakubeit, T. Latka, O. Razskazovskaya, H. Fattahi, M. Jobst, W. Schweinberger, V. Shirvanyan, V. S. Yakovlev, R. Kienberger, K. Yabana, N. Karpowicz, M. Schultze, and F. Krausz. Attosecond nonlinear polarization and light-matter energy transfer in solids. *Nature*, 534(7605):86–90, 5 2016.

[3] F Remacle and R D Levine. An electronic time scale in chemistry. *Proceedings of the National Academy of Sciences*, 103(18):6793–6798, 5 2006.

[4] Francesca Calegari and Fernando Martin. Open questions in attochemistry. *Communications Chemistry*, 6(1):184, 2023.

[5] John C. Travers, Teodora F. Grigorova, Christian Brahms, and Federico Belli. High-energy pulse self-compression and ultraviolet generation through soliton dynamics in hollow capillary fibres. *Nature Photonics*, 13(8):547–554, 8 2019.

[6] Christian Brahms and John C Travers. HISOL: High-energy soliton dynamics enable ultrafast far-ultraviolet laser sources. *APL Photonics*, 9(5):050901, 5 2024.

[7] Ferenc Krausz and Misha Ivanov. Attosecond physics. *Reviews of Modern Physics*, 81(1):163–234, 1 2009.

[8] E Goulielmakis, M Schultze, M Hofstetter, V S Yakovlev, J Gagnon, M Uiberacker, A L Aquila, E M Gullikson, D T Attwood, R Kienberger, F Krausz, and U Kleineberg. Single-Cycle Nonlinear Optics. *Science*, 320(5883):1614–1617, 6 2008.

[9] M Ossiander, K Golyari, K Scharl, L Lehnert, F Siegrist, J P Bürger, D Zimin, J A Gessner, M Weidman, I Floss, V Smejkal, S Donsa, C Lemell, F Libisch, N Karpowicz, J Burgdörfer, F Krausz, and M Schultze. The speed limit of optoelectronics. *Nature Communications*, 13(1):1620, 2022.

[10] Shawn Sederberg, Dmitry Zimin, Sabine Keiber, Florian Siegrist, Michael S Wismer, Vladislav S Yakovlev, Isabella Floss, Christoph Lemell, Joachim Burgdörfer, Martin Schultze, Ferenc Krausz, and Nicholas Karpowicz. Attosecond optoelectronic field measurement in solids. *Nature Communications*, 11(1):430, 2020.

[11] Dmitry Zimin, Matthew Weidman, Johannes Schötz, Matthias F. Kling, Vladislav S. Yakovlev, Ferenc Krausz, and Nicholas Karpowicz. Petahertz-scale nonlinear photoconductive sampling in air. *Optica*, 8(5):586, 5 2021.

[12] A L'Huillier, K J Schafer, and K C Kulander. Theoretical aspects of intense field harmonic generation. *Journal of Physics B: Atomic, Molecular and Optical Physics*, 24(15):3315, 1991.

[13] M Lewenstein, Ph. Balcou, M Yu. Ivanov, Anne L'Huillier, and P B Corkum. Theory of high-harmonic generation by low-frequency laser fields. *Physical Review A*, 49(3):2117–2132, 3 1994.

[14] M Ferray, A L'Huillier, X F Li, L A Lompre, G Mainfray, and C Manus. Multiple-harmonic conversion of 1064 nm radiation in rare gases. *Journal of Physics B: Atomic, Molecular and Optical Physics*, 21(3):L31, 1988.

[15] Demetris G Lappas and Anne L'Huillier. Generation of attosecond xuv pulses in strong laser-atom interactions. *Physical Review A*, 58(5):4140–4146, 11 1998.

[16] P M Paul, E S Toma, P Breger, G Mullot, F Augé, Ph. Balcou, H G Muller, and P Agostini. Observation of a Train of Attosecond Pulses from High Harmonic Generation. *Science*, 292(5522):1689–1692, 6 2001.

[17] M Hentschel, R Kienberger, Ch. Spielmann, G A Reider, N Milosevic, T Brabec, P Corkum, U Heinzmann, M Drescher, and F Krausz. Attosecond metrology. *Nature*, 414(6863):509–513, 2001.

[18] J Itatani, F Quéré, G L Yudin, M Yu. Ivanov, F Krausz, and P B Corkum. Attosecond Streak Camera. *Physical Review Letters*, 88(17):173903, 4 2002.

[19] R Kienberger, E Goulielmakis, M Uiberacker, A Baltuska, V Yakovlev, F Bammer, A Scrinzi, Th. Westerwalbesloh, U Kleineberg, U Heinzmann,

M Drescher, and F Krausz. Atomic transient recorder. *Nature*, 427(6977):817–821, 2004.

[20] E Goulielmakis, M Uiberacker, R Kienberger, A Baltuska, V Yakovlev, A Scrinzi, Th. Westerwalbesloh, U Kleineberg, U Heinzmann, M Drescher, and F Krausz. Direct Measurement of Light Waves. *Science*, 305(5688):1267–1269, 8 2004.

[21] G. Sansone, E. Benedetti, F. Calegari, C. Vozzi, L. Avaldi, R. Flammini, L. Poletto, P. Villoresi, C. Altucci, R. Velotta, S. Stagira, S. De Silvestri, and M. Nisoli. Isolated single-cycle attosecond pulses. *Science*, 314(5798):443–446, 10 2006.

[22] Eleftherios Goulielmakis, Zhi Heng Loh, Adrian Wirth, Robin Santra, Nina Rohringer, Vladislav S. Yakovlev, Sergey Zherebtsov, Thomas Pfeifer, Abdallah M. Azzeer, Matthias F. Kling, Stephen R. Leone, and Ferenc Krausz. Real-time observation of valence electron motion. *Nature*, 466(7307):739–743, 8 2010.

[23] M Schultze, M Fieß, N Karpowicz, J Gagnon, M Korbman, M Hofstetter, S Neppl, A L Cavalieri, Y Komninos, Th. Mercouris, C A Nicolaides, R Pazourek, S Nagele, J Feist, J Burgdörfer, A M Azzeer, R Ernstorfer, R Kienberger, U Kleineberg, E Goulielmakis, F Krausz, and V S Yakovlev. Delay in Photoemission. *Science*, 328(5986):1658–1662, 2010.

[24] Florian Siegrist, Julia A. Gessner, Marcus Ossiander, Christian Denker, Yi Ping Chang, Malte C. Schröder, Alexander Guggenmos, Yang Cui, Jakob Walowski, Ulrike Martens, J. K. Dewhurst, Ulf Kleineberg, Markus Münzenberg, Sangeeta Sharma, and Martin Schultze. Light-wave dynamic control of magnetism. *Nature*, 571(7764):240–244, 7 2019.

[25] Martin Schultze, Krupa Ramasesha, C D Pemmaraju, S A Sato, D Whitmore, A Gandman, James S Prell, L J Borja, D Prendergast, K Yabana, Daniel M Neumark, and Stephen R Leone. Attosecond band-gap dynamics in silicon. *Science*, 346(6215):1348–1352, 2014.

[26] Matteo Lucchini, Shunsuke A Sato, Giacinto D Lucarelli, Bruno Moio, Giacomo Inzani, Rocío Borrego-Varillas, Fabio Frassetto, Luca Poletto, Hannes Hübener, Umberto De Giovannini, Angel Rubio, and Mauro Nisoli. Unravelling the intertwined atomic and bulk nature of localised excitons by attosecond spectroscopy. *Nature Communications*, 12(1):1021–1027, 2021.

[27] F Schlaepfer, M Lucchini, S A Sato, M Volkov, L Kasmi, N Hartmann, A Rubio, L Gallmann, and U Keller. Attosecond optical-field-enhanced carrier injection into the GaAs conduction band. *Nature Physics*, 14(6):560–564, 2018.

[28] M. Volkov, S. A. Sato, F. Schlaepfer, L. Kasmi, N. Hartmann, M. Lucchini, L. Gallmann, A. Rubio, and U. Keller. Attosecond screening dynamics mediated by electron localization in transition metals. *Nature Physics*, 15(11):1145–1149, 11 2019.

[29] Romain Géneaux, Christopher J. Kaplan, Lun Yue, Andrew D. Ross, Jens E. Bækhøj, Peter M. Kraus, Hung Tzu Chang, Alexander Guggenmos, Mi Ying Huang, Michael Zürch, Kenneth J. Schafer, Daniel M. Neumark, Mette B. Gaarde, and Stephen R. Leone. Attosecond Time-Domain Measurement of Core-Level-Exciton Decay in Magnesium Oxide. *Physical Review Letters*, 124(20):207401(1)–(6), 5 2020.

[30] Mauro Nisoli, Piero Decleva, Francesca Calegari, Alicia Palacios, and Fernando Martín. Attosecond Electron Dynamics in Molecules. *Chemical Reviews*, 117(16):10760–10825, 8 2017.

[31] Peng Peng, Claude Marceau, and David M Villeneuve. Attosecond imaging of molecules using high harmonic spectroscopy. *Nature Reviews Physics*, 1(2):144–155, 2019.

[32] F Calegari, D Ayuso, A Trabattoni, L Belshaw, S De Camillis, S Anumula, F Frassetto, L Poletto, A Palacios, P Decleva, J B Greenwood, F Martín, and M Nisoli. Ultrafast electron dynamics in phenylalanine initiated by attosecond pulses. *Science*, 346(6207):336–339, 10 2014.

[33] G Sansone, F Kelkensberg, J F Pérez-Torres, F Morales, M F Kling, W Siu, O Ghafur, P Johnsson, M Swoboda, E Benedetti, F Ferrari, F Lépine, J L Sanz-Vicario, S Zherebtsov, I Znakovskaya, A L'Huillier, M Yu. Ivanov, M Nisoli, F Martín, and M J J Vrakking. Electron localization following attosecond molecular photoionization. *Nature*, 465(7299):763–766, 2010.

[34] Manuel Lara-Astiaso, Mara Galli, Andrea Trabattoni, Alicia Palacios, David Ayuso, Fabio Frassetto, Luca Poletto, Simone De Camillis, Jason Greenwood, Piero Decleva, Ivano Tavernelli, Francesca Calegari, Mauro Nisoli, and Fernando Martín. Attosecond Pump–Probe Spectroscopy of Charge Dynamics in Tryptophan. *The Journal of Physical Chemistry Letters*, 9(16):4570–4577, 8 2018.

[35] E Goulielmakis, V S Yakovlev, A L Cavalieri, M Uiberacker, V Pervak, A Apolonski, R Kienberger, U Kleineberg, and F Krausz. Attosecond Control and Measurement: Lightwave Electronics. *Science*, 317(5839):769–775, 8 2007.

[36] O Schubert, M Hohenleutner, F Langer, B Urbanek, C Lange, U Huttner, D Golde, T Meier, M Kira, S W Koch, and R Huber. Sub-cycle control of terahertz high-harmonic generation by dynamical Bloch oscillations. *Nature Photonics*, 8(2):119–123, 2014.

[37] Markus Borsch, Manuel Meierhofer, Rupert Huber, and Mackillo Kira. Lightwave electronics in condensed matter. *Nature Reviews Materials*, 8(10):668–687, 2023.

[38] A L Cavalieri, N Müller, Th. Uphues, V S Yakovlev, A Baltuška, B Horvath, B Schmidt, L Blümel, R Holzwarth, S Hendel, M Drescher, U Kleineberg, P M Echenique, R Kienberger, F Krausz, and U Heinzmann. Attosecond spectroscopy in condensed matter. *Nature*, 449(7165):1029–1032, 2007.

[39] A Wirth, M Th. Hassan, I Grguraš, J Gagnon, A Moulet, T T Luu, S Pabst, R Santra, Z A Alahmed, A M Azzeer, V S Yakovlev, V Pervak, F Krausz, and E Goulielmakis. Synthesized Light Transients. *Science*, 334(6053):195–200, 2011.

[40] Enrico Ridente, Mikhail Mamaikin, Najd Altwaijry, Dmitry Zimin, Matthias F Kling, Vladimir Pervak, Matthew Weidman, Ferenc Krausz, and Nicholas Karpowicz. Electro-optic characterization of synthesized infrared-visible light fields. *Nature Communications*, 13(1):1111, 2022.

[41] Husain Alqattan, Dandan Hui, Vladimir Pervak, and Mohammed Th. Hassan. Attosecond light field synthesis. *APL Photonics*, 7(4):041301, 4 2022.

[42] D. H. Auston. Picosecond optoelectronic switching and gating in silicon. *Applied Physics Letters*, 26(3):101–103, 1975.

[43] Seung Beom Park, Kyungseung Kim, Wosik Cho, Sung In Hwang, Igor Ivanov, Chang Hee Nam, and Kyung Taec Kim. Direct sampling of a light wave in air. *Optica*, 5(4):402, 4 2018.

[44] Agustin Schiffrin, Tim Paasch-Colberg, Nicholas Karpowicz, Vadym Apalkov, Daniel Gerster, Sascha Mühlbrandt, Michael Korbman, Joachim Reichert, Martin Schultze, Simon Holzner, Johannes V. Barth, Reinhard Kienberger, Ralph Ernstorfer, Vladislav S. Yakovlev, Mark I. Stockman, and Ferenc

Krausz. Optical-field-induced current in dielectrics. *Nature*, 493(7430):70–74, 1 2013.

[45] Kyung Taec Kim, Chunmei Zhang, Andrew D. Shiner, Bruno E. Schmidt, François Légaré, D. M. Villeneuve, and P. B. Corkum. Petahertz optical oscilloscope. *Nature Photonics*, 7(12):958–962, 12 2013.

[46] Yangyang Liu, John E Beetar, Jonathan Nesper, Shima Gholam-Mirzaei, and Michael Chini. Single-shot measurement of few-cycle optical waveforms on a chip. *Nature Photonics*, 16(2):109–112, 2022.

[47] Mina R. Bionta, Felix Ritzkowsky, Marco Turchetti, Yujia Yang, Dario Cattozzo Mor, William P. Putnam, Franz X. Kärtner, Karl K. Berggren, and Phillip D. Keathley. On-chip sampling of optical fields with attosecond resolution. *Nature Photonics*, 15(6):456–460, 6 2021.

[48] Michael Krüger, Markus Schenk, and Peter Hommelhoff. Attosecond control of electrons emitted from a nanoscale metal tip. *Nature*, 475(7354):78–81, 2011.

[49] Johannes Schötz, Lennart Seiffert, Ancyline Maliakkal, Johannes Blöchl, Dmitry Zimin, Philipp Rosenberger, Boris Bergues, Peter Hommelhoff, Ferenc Krausz, Thomas Fennel, and Matthias F. Kling. Onset of charge interaction in strong-field photoemission from nanometric needle tips. *Nanophotonics*, 10(14):3769–3775, 10 2021.

[50] Johannes Schötz, Ancyline Maliakkal, Johannes Blöchl, Dmitry Zimin, Zilong Wang, Philipp Rosenberger, Meshaal Alharbi, Abdallah M Azzeer, Matthew Weidman, Vladislav S Yakovlev, Boris Bergues, and Matthias F Kling. The emergence of macroscopic currents in photoconductive sampling of optical fields. *Nature Communications*, 13(1):962, 2022.

[51] Mara Galli, Vincent Wanie, Diogo Pereira Lopes, Erik P. Månsson, Andrea Trabattoni, Lorenzo Colaizzi, Krishna Saraswathula, Andrea Cartella, Fabio Frassetto, Luca Poletto, François Légaré, Salvatore Stagira, Mauro Nisoli, Rebeca Martínez Vázquez, Roberto Osellame, and Francesca Calegari. Generation of deep ultraviolet sub-2-fs pulses. *Optics Letters*, 44(6):1308, 3 2019.

[52] Florentin Reiter, Ulrich Graf, Martin Schultze, Wolfgang Schweinberger, Hartmut Schröder, Nicholas Karpowicz, Abdallah Mohammed Azzeer, Reinhard Kienberger, Ferenc Krausz, and Eleftherios Goulielmakis. Generation of sub-3 fs pulses in the deep ultraviolet. *Optics Letters*, 35(13):2248–2250, 2010.

[53] M. Reduzzi, M. Pini, L. Mai, F. Cappenberg, L. Colaizzi, F. Vismarra, A. Crego, M. Lucchini, C. Brahms, J. C. Travers, R. Borrego-Varillas, and M. Nisoli. Direct temporal characterization of sub-3-fs deep UV pulses generated by resonant dispersive wave emission. *Optics Express*, 31(16):26854, 7 2023.

[54] Felix Köttig, Francesco Tani, Christian Martens Biersach, John C. Travers, and Philip St.J. Russell. Generation of microjoule pulses in the deep ultraviolet at megahertz repetition rates. *Optica*, 4(10):1272, 10 2017.

[55] John C Travers. Optical solitons in hollow-core fibres. *Optics Communications*, 555:130191, 3 2024.

[56] Christian Brahms, Teodora Grigorova, Federico Belli, and John C. Travers. High-energy ultraviolet dispersive-wave emission in compact hollow capillary systems. *Optics Letters*, 44(12):2990, 6 2019.

[57] Christian Brahms, Dane R. Austin, Francesco Tani, Allan S. Johnson, Douglas Garratt, John C. Travers, John W. G. Tisch, Philip St.J. Russell, and Jon P. Marangos. Direct characterization of tuneable few-femtosecond dispersive-wave pulses in the deep UV. *Optics Letters*, 44(4):731, 2 2019.

[58] David J Griffiths. *Introduction to Electrodynamics.* Cambridge University Press, Cambridge, 4th edition, 2017.

[59] Jean-Claude Diels. *Ultrashort laser pulse phenomena : fundamentals, techniques, and applications on a femtosecond time scale.* Optics and photonics. Academic Press, Burlington, MA, 2nd edition, 2006.

[60] Zenghu Chang. *Fundamentals of attosecond optics.* CRC Press, Boca Raton, Fla., 2011.

[61] Rick Trebino and Erik Zeek. Ultrashort Laser Pulses. In *Frequency-Resolved Optical Gating: The Measurement of Ultrashort Laser Pulses*, pages 11–35. Springer US, Boston, MA, 2000.

[62] Robert W Boyd. *Nonlinear optics.* Academic Press, Burlington, MA, 3rd edition, 2008.

[63] Govind P. Agrawal. *Nonlinear Fiber Optics*, volume 5th Edition of *Optics and Photonics.* Academic Press, Elsevier Inc., 2013.

[64] Ka Fai Mak, John C. Travers, Philipp Hölzer, Nicolas Y. Joly, and Philip St. J. Russell. Tunable vacuum-UV to visible ultrafast pulse source based on gas-filled Kagome-PCF. *Optics Express*, 21(9):10942, 5 2013.

[65] Christian Brahms, Federico Belli, and John C Travers. Resonant dispersive wave emission in hollow capillary fibers filled with pressure gradients. *Opt. Lett.*, 45(16):4456–4459, 8 2020.

[66] Units The NIST Reference on Constants, Uncertainty, National Institute of Standards, and US Department of Commerce Technology. Fundamental Physical Constants.

[67] L V Keldysh. Ionization in the Field of a Strong Electromagnetic Wave. Technical Report 5, P.N. Lebedev Physics Institute, Moscow, 5 1965.

[68] J H Eberly and J Javanainen. Above-threshold ionisation. *European Journal of Physics*, 9(4):265, 1988.

[69] Maxim V Ammosov, Nikolai B Delone, and Vladimir P Krainov. Tunnel Ionization Of Complex Atoms And Atomic Ions In Electromagnetic Field. In *Proc.SPIE*, volume 0664, pages 138–141, 10 1986.

[70] P B Corkum. Plasma perspective on strong field multiphoton ionization. *Physical Review Letters*, 71(13):1994–1997, 9 1993.

[71] Tenio Popmintchev, Ming-Chang Chen, Alon Bahabad, Michael Gerrity, Pavel Sidorenko, Oren Cohen, Ivan P Christov, Margaret M Murnane, and Henry C Kapteyn. Phase matching of high harmonic generation in the soft and hard X-ray regions of the spectrum. *Proceedings of the National Academy of Sciences (PNAS)*, 106(26):10516–10521, 6 2009.

[72] Laura Rego, Julio San Román, Luis Plaja, Antonio Picón, and Carlos Hernández-García. Ultrashort Extreme Ultraviolet Vortices. In *Vortex Dynamics and Optical Vortices*, chapter 9. IntechOpen, 2017.

[73] Julia Anthea Gessner. *Strong-Field Driven Charge and Spin Dynamics in Solids.* PhD thesis, Ludwig-Maximilians-Universität München, München, 2021.

[74] Takao Fuji, Jens Rauschenberger, Alexander Apolonski, Vladislav S Yakovlev, Gabriel Tempea, Thomas Udem, Christoph Gohle, Theodor W Hänsch, Walter Lehnert, Michael Scherer, and Ferenc Krausz. Monolithic carrier-envelope phase-stabilization scheme. *Optics Letters*, 30(3), 2005.

[75] Donna Strickland and Gerard Mourou. Compression of amplified chirped optical pulses. *Optics Communications*, 55(6):447–449, 10 1985.

[76] Ferenc Krausz and Mark I. Stockman. Attosecond metrology: from electron capture to future signal processing. *Nature Photonics*, 8(3):205–213, 3 2014.

[77] M. Lucchini, M.H. Brügmann, A. Ludwig, L. Gallmann, U. Keller, and T. Feurer. Ptychographic reconstruction of attosecond pulses. *Optics Express*, 23(23):29502, 11 2015.

[78] Y. Mairesse and F. Quéré. Frequency-resolved optical gating for complete reconstruction of attosecond bursts. *Physical Review A - Atomic, Molecular, and Optical Physics*, 71(1), 1 2005.

[79] J. Gagnon, E. Goulielmakis, and V. S. Yakovlev. The accurate FROG characterization of attosecond pulses from streaking measurements. *Applied Physics B: Lasers and Optics*, 92(1):25–32, 7 2008.

[80] Najd Altwaijry, Muhammad Qasim, Dmitry Zimin, Nicholas Karpowicz, and Matthias F. Kling. Sensitivity Enhancement in Photoconductive Light Field Sampling. *Advanced Optical Materials*, 2024.

[81] Johannes Schötz, Ancyline Maliakkal, Johannes Blöchl, Dmitry Zimin, Zilong Wang, Philipp Rosenberger, Meshaal Alharbi, Abdallah M. Azzeer, Matthew Weidman, Vladislav S. Yakovlev, Boris Bergues, and Matthias F. Kling. The emergence of macroscopic currents in photoconductive sampling of optical fields. *Nature Communications*, 13(1), 12 2022.

[82] Manoram Agarwal, Armin Scrinzi, Ferenc Krausz, and Vladislav S Yakovlev. Theory of Nonlinear Photoconductive Sampling in Atomic Gases. *Annalen der Physik*, 535(12):2300322, 12 2023.

[83] Najd Abdulaziz Suliman Altwaijry. *Pushing the boundaries of photoconductive sampling in solids.* PhD thesis, Ludwig-Maximilians-Universität München, München, 2023.

[84] C E Shannon. Communication in the Presence of Noise. *Proceedings of the IRE*, 37(1):10–21, 1949.

[85] Zurich Instruments. Principles of lock-in detection and the state of the art, 2016.

[86] Keyhan Golyari. *Linear-Petahertz-PhotoConductive Switching.* PhD thesis, Ludwig-Maximilians-Universität München, München, 2022.

[87] Ioachim Pupeza, Marinus Huber, Michael Trubetskov, Wolfgang Schweinberger, Syed A Hussain, Christina Hofer, Kilian Fritsch, Markus Poetzlberger, Lenard Vamos, Ernst Fill, Tatiana Amotchkina, Kosmas V Kepesidis, Alexander Apolonski, Nicholas Karpowicz, Vladimir Pervak, Oleg Pronin, Frank

Fleischmann, Abdallah Azzeer, Mihaela Žigman, and Ferenc Krausz. Field-resolved infrared spectroscopy of biological systems. *Nature*, 577(7788):52–59, 2020.

[88] Marinus Huber, Kosmas V Kepesidis, Liudmila Voronina, Frank Fleischmann, Ernst Fill, Jacqueline Hermann, Ina Koch, Katrin Milger-Kneidinger, Thomas Kolben, Gerald B Schulz, Friedrich Jokisch, Jürgen Behr, Nadia Harbeck, Maximilian Reiser, Christian Stief, Ferenc Krausz, and Mihaela Zigman. Infrared molecular fingerprinting of blood-based liquid biopsies for the detection of cancer. *eLife*, 10:e68758, 2021.

[89] Liudmila Voronina, Frank Fleischmann, Jelena Šimunović, Christina Ludwig, Mislav Novokmet, and Mihaela Žigman. Probing Blood Plasma Protein Glycosylation with Infrared Spectroscopy. *Analytical Chemistry*, 96(7):2830–2839, 2 2024.

[90] Kosmas V. Kepesidis, Masa Bozic-Iven, Marinus Huber, Nashwa Abdel-Aziz, Sharif Kullab, Ahmed Abdelwarith, Abdulrahman Al Diab, Mohammed Al Ghamdi, Muath Abu Hilal, Mohun R.K. Bahadoor, Abhishake Sharma, Farida Dabouz, Maria Arafah, Abdallah M. Azzeer, Ferenc Krausz, Khalid Alsaleh, Mihaela Zigman, and Jean Marc Nabholtz. Breast-cancer detection using blood-based infrared molecular fingerprints. *BMC Cancer*, 21(1), 12 2021.

[91] Tarek Eissa, Kosmas V. Kepesidis, Mihaela Zigman, and Marinus Huber. Limits and Prospects of Molecular Fingerprinting for Phenotyping Biological Systems Revealed through In Silico Modeling. *Analytical Chemistry*, 95(16):6523–6532, 4 2023.

[92] Maria Paraskevaidi, Baker J Matthew, Butler J Holly, Byrne J Hugh, Chakkumpulakkal P V Thulya, Christie Loren, Crean StJohn, Gardner Peter, Gassner Callum, Kazarian G Sergei, Kochan Kamila, Kyrgiou Maria, Lima M G Kássio, Martin-Hirsch L Pierre, Paraskevaidis Evangelos, Pebotuwa Savithri, Adegoke A John, Sala Alexandra, Santos Marfran, Sulé-Suso Josep, Tyagi Gunjan, Walsh Michael, and Wood Bayden. Clinical applications of infrared and Raman spectroscopy in the fields of cancer and infectious diseases. *Applied Spectroscopy Reviews*, 56(8-10):804–868, 11 2021.

[93] Zhou Wang, Hyunwook Park, Yu Hang Lai, Junliang Xu, Cosmin I Blaga, Fengyuan Yang, Pierre Agostini, and Louis F DiMauro. The roles of photo-carrier doping and driving wavelength in high harmonic generation from a semiconductor. *Nature Communications*, 8(1):1686, 2017.

[94] Giacomo Inzani, Lyudmyla Adamska, Amir Eskandari-asl, Nicola Di Palo, Gian Luca Dolso, Bruno Moio, Luciano Jacopo D'Onofrio, Alessio Lamperti, Alessandro Molle, Rocío Borrego-Varillas, Mauro Nisoli, Stefano Pittalis, Carlo Andrea Rozzi, Adolfo Avella, and Matteo Lucchini. Field-driven attosecond charge dynamics in germanium. *Nature Photonics*, 17(12):1059–1065, 12 2023.

[95] M Lewenstein, N Baldelli, U Bhattacharya, J Biegert, M F Ciappina, T Grass, P T Grochowski, A S Johnson, Th. Lamprou, A S Maxwell, A Ordóñez, E Pisanty, J Rivera-Dean, P Stammer, and P Tzallas. Attosecond Physics and Quantum Information Science. In Luca Argenti, Michael Chini, and Li Fang, editors, *Proceedings of the 8th International Conference on Attosecond Science and Technology*, pages 27–44, Cham, 2024. Springer International Publishing.

[96] Á Jiménez-Galán, R E F Silva, O Smirnova, and M Ivanov. Lightwave control of topological properties in 2D materials for sub-cycle and non-resonant valley manipulation. *Nature Photonics*, 14(12):728–732, 2020.

[97] Sambit Mitra, Álvaro Jiménez-Galán, Mario Aulich, Marcel Neuhaus, Rui E F Silva, Volodymyr Pervak, Matthias F Kling, and Shubhadeep Biswas. Lightwave-controlled Haldane model in monolayer hexagonal boron nitride. *Nature*, 628(8009):752–757, 2024.

[98] Philipp Stammer, Javier Rivera-Dean, Theocharis Lamprou, Emilio Pisanty, Marcelo F Ciappina, Paraskevas Tzallas, and Maciej Lewenstein. High Photon Number Entangled States and Coherent State Superposition from the Extreme Ultraviolet to the Far Infrared. *Physical Review Letters*, 128(12):123603, 3 2022.

[99] J Reimann, S Schlauderer, C P Schmid, F Langer, S Baierl, K A Kokh, O E Tereshchenko, A Kimura, C Lange, J Güdde, U Höfer, and R Huber. Subcycle observation of lightwave-driven Dirac currents in a topological surface band. *Nature*, 562(7727):396–400, 2018.

[100] Y C Shen, P C Upadhya, H E Beere, E H Linfield, A G Davies, I S Gregory, C Baker, W R Tribe, and M J Evans. Generation and detection of ultra-broadband terahertz radiation using photoconductive emitters and receivers. *Applied Physics Letters*, 85(2):164–166, 7 2004.

[101] Najd Altwaijry, Muhammad Qasim, Mikhail Mamaikin, Johannes Schötz, Keyhan Golyari, Michael Heynck, Enrico Ridente, Vladislav S Yakovlev, Nicholas Karpowicz, and Matthias F Kling. Broadband Photoconductive Sampling in Gallium Phosphide. *Advanced Optical Materials*, 11(9):2202994, 5 2023.

[102] M. Högner, V. Tosa, and I. Pupeza. Generation of isolated attosecond pulses with enhancement cavities —a theoretical study. *New Journal of Physics*, 19(3), 3 2017.

[103] Johannes Schötz. *Field-resolved studies of ultrafast light-matter interaction.* PhD thesis, Ludwig-Maximilians-Universität München, München, 2021.

[104] G. Doumy, J. Wheeler, C. Roedig, R. Chirla, P. Agostini, and L. F. Dimauro. Attosecond synchronization of high-order harmonics from midinfrared drivers. *Physical Review Letters*, 102(9), 3 2009.

[105] The Center for X-Ray Optics, B.L. Henke, E.M. Gullikson, and J.C. Davis. X-Ray Reflectivity Mirror Data Base, 7 1993.

[106] Clemens Tobias Friedrich Jakubeit. *High Harmonic Generation using a 2 $\mu m$ OPCPA*. PhD thesis, Ludwig-Maximilians-Universität München, Munich, 4 2019.

[107] Francesco Tani, John C. Travers, and Philip St.J. Russell. Multimode ultrafast nonlinear optics in optical waveguides: numerical modeling and experiments in kagomé photonic-crystal fiber. *Journal of the Optical Society of America B*, 31(2):311, 2 2014.

[108] Amelie M. Heinzerling, Francesco Tani, Manoram Agarwal, Vladislav S. Yakovlev, Ferenc Krausz, and Nicholas Karpowicz. Field-resolved attosecond solitons. Submitted manuscript in review, 2024.

[109] Paris Panagiotopoulos, Patrick Whalen, Miroslav Kolesik, and Jerome V. Moloney. Super high power mid-infrared femtosecond light bullet. *Nature Photonics*, 9(8):543–548, 7 2015.

[110] Patrick Whalen, Paris Panagiotopoulos, Miroslav Kolesik, and Jerome V. Moloney. Extreme carrier shocking of intense long-wavelength pulses. *Physical Review A - Atomic, Molecular, and Optical Physics*, 89(2), 2 2014.

[111] Dmitry A Zimin, Nicholas Karpowicz, Muhammad Qasim, Matthew Weidman, Ferenc Krausz, and Vladislav S Yakovlev. Dynamic optical response of solids following 1-fs-scale photoinjection. *Nature*, 618(7964):276–280, 2023.

[112] Armin Scrinzi. tRecX — An environment for solving time-dependent Schrödinger-like problems. *Computer Physics Communications*, 270:108146, 2022.

# Acknowledgements

I am incredibly grateful to everyone who contributed to this work and made my PhD time an incredible experience. First and foremost, I would like to express my deepest gratitude to my "Doktorvater" Ferenc Krausz for being an extraordinary advisor who seems to be overflowing with energy, knowledge and confidence in reaching his goals. I am extremely grateful for the opportunity to be a member of this amazing research group and to work in this advanced MPQ laboratory (mostly as a scientist, sometimes also as plumber, engineer, mechanic, cleaner, repairman, tour guide, TV actor,..). Special thanks for accepting my wish to keep working with FP3 till the end!

Moreover, I would like to extend my deepest appreciation to the direct supervisors I had over the time. First of all, I am extremely grateful to Matthew Weidman for welcoming and introducing me to the LAP world in the very beginning. Furthermore, this endeavour would not have been possible without Johannes Schötz, who took over my supervision without any concern and taught me the fundamentals and details of field sampling. I am incredibly grateful for his tremendous support in the lab, as well as with the simulations and feedback for Chapter 4. Last but not least, words cannot express my gratitude to Nick Karpowicz, who basically inherited the supervision of me in the middle of my "the laser is broken"-crisis. I am very grateful for the guidance and support to get the system running again, reach my goals and achieve this work. Moreover, many thanks for proof-reading of all these pages in such a short time!

In addition, I would like to extend my sincere thanks to Francesco Tani and his broad knowledge about solitons and dispersive waves, paving the way for my greatest measurements and comparing them with simulations. Special thanks for his input and support for the paper. Moreover, I would like to thank Vlad Yakovlev to always have an open door and being incredibly helpful, not only as theorist, but also with IMPRS-APS or atto-interna questions. I am also grateful to Agustin Schiffrin for being my secondary advisor in my thesis advisory committee, helping to guide me through this journey.

I would like to thank the attosecond metrology / spectrocopy 2.0 team for the continuous support during the last years! I am extremely grateful for the help in the lab, discussions, and all the fun in the breaks and at parties. Many thanks to Najd Altwaijry and Mikhail Mamaikin, for all the chats, fun, advice, trips, parties, and special thanks for your precious feedback on this thesis! I am very grateful to Julia Gessner who taught me how to use and take care of FP3 and AS2 and joined me on a great trip to Budapest. Special thanks to Najd and Julia for the women-power, being severely missed after their graduations. Moreover, I would like to thank Keyhan Golyari for being a great group dad, always taking care of everyone (or that everyone has enough meat). Special thanks to Manoram Agarwal for being a great office mate and doing simulations for me! Additionally, I would like to thank Marco Dassie for being so patient with me and being very fair with the laser sharing (aka thanks for always giving me beamtime when I need it). I am still impressed that he is always fine or 'ok', no matter what happens. Thanks to Dmitrii Kormin for all the support in the lab and outside, especially for pushing to find a reasonable work-life-balance. Special thanks to Misha, Tanya, Marco and Mano for the great trip to South Korea.

I am also thankful to my other former colleagues. Firstly, thanks to Michael Heynck, who started simultaneously with me as a Masters student, for learning together, and making the topic of RDWs more present. Secondly, thanks to Corinna Konrad for being a great Master student that I could teach the system and share endless hours working together at AS4. Thirdly, thanks to Eva Bayer for staying in touch and becoming a great friend. Finally, also many thanks to Muhammad Qasim, Simon Reiger, Enrico Ridente, Clemens Jakubeit and all others I might have missed.

Additionally, I am very grateful for the support from other teams. I would like to acknowledge Vladimir Pervak and Daniel Hahner for providing me with home-coated optics. Moreover, I had the pleasure of working with our technical team: Andreas Küchler, Harald Haas and Tobias Kleinhenz, and Michael Rogg and his team in the workshop. I would also like to acknowledge the electrical engineers Hojjat Heydarian and Behnam Jahedi. Furthermore, I would like to recognize the administrative team: Thanks for the great efforts Nicole Buchwiser and Ruth Göttler!

Many thanks to my friends for listening to my laser stories, trying to understand what I am doing (like questions about the difference between a pulse and an impulse), your encouragement and helping me to find a good work-life-balance. I am also grateful to my Volleyball team for creating a pleasant and fun atmosphere during practice and games. It always helped me immensely to free my mind and just have fun!

Finally, my deepest gratitude goes to my family. I am extremely thankful for your unconditional support and understanding for long working hours and that I could not always attend every get-together. Special thanks to my parents for always encouraging and supporting me in every possible way. I wouldn't have accomplished this work without your guidance and love throughout my whole life, helping me to become the person I am today. Further special thanks go to Jan: I could not have undertaken this journey without you. Thank you for always having my back! I cannot thank you enough for always believing in me and encouraging me, for celebrating every tiny achievement or good news with me, or hugging me while I cry in frustrating moments. Thank you for always cheering me up and making me smile. You definitely deserve to be "Herr Doktor".